

Fall 2014

Dynamics of Energy Carriers in Solids During Interaction with Ultrafast Laser Pulses

Liang Guo
Purdue University

Follow this and additional works at: https://docs.lib.purdue.edu/open_access_dissertations

Recommended Citation

Guo, Liang, "Dynamics of Energy Carriers in Solids During Interaction with Ultrafast Laser Pulses" (2014). *Open Access Dissertations*. 276.
https://docs.lib.purdue.edu/open_access_dissertations/276

This document has been made available through Purdue e-Pubs, a service of the Purdue University Libraries. Please contact epubs@purdue.edu for additional information.

PURDUE UNIVERSITY
GRADUATE SCHOOL
Thesis/Dissertation Acceptance

This is to certify that the thesis/dissertation prepared

By Liang Guo

Entitled
Dynamics of Energy Carriers in Solids During Interaction with Ultrafast Laser Pulses

For the degree of Doctor of Philosophy



Is approved by the final examining committee:

Xianfan Xu (Chair)

Timothy S. Fisher

Xiulin Ruan

Ali Shakouri

To the best of my knowledge and as understood by the student in the Thesis/Dissertation Agreement, Publication Delay, and Certification/Disclaimer (Graduate School Form 32), this thesis/dissertation adheres to the provisions of Purdue University's "Policy on Integrity in Research" and the use of copyrighted material.

Xianfan Xu (Chair)

Approved by Major Professor(s): _____

Approved by: Ganesh Subbarayan

09/16/2014

Head of the Department Graduate Program

Date

DYNAMICS OF ENERGY CARRIERS IN SOLIDS DURING INTERACTION WITH
ULTRAFAST LASER PULSES

A Dissertation

Submitted to the Faculty

of

Purdue University

by

Liang Guo

In Partial Fulfillment of the

Requirements for the Degree

of

Doctor of Philosophy

December, 2014

Purdue University

West Lafayette, Indiana

ACKNOWLEDGEMENTS

I have been so fortunate to receive so much help from the kind people around me during my graduate study and here I would like to express my sincere gratitude to all of them.

My first appreciation is for my advisor, Prof. Xianfan Xu. His rich experience, insightful suggestions, and patient guidance always drove me to overcome bottlenecks and move forward throughout my research work. He also provided a nice atmosphere with talented peers, state-of-the-art facilities, and illuminating discussions. The experience of working with him will benefit my professional development in the future. I would also like to thank Prof. Timothy S. Fisher, Prof. Xiulin Ruan, and Prof. Ali Shakouri for being my advisory committee members. Besides, I appreciate James Salvador from General Motor and Prof. Jihui Yang from University of Washington for providing and characterizing skutterudite samples and helpful discussions. I also want to say thanks to all of my lab mates, especially to Carl M. Liebig, Yaguo Wang, Wenzhi Wu, Bryan T. Spann and Yan Li, who helped me a lot in both research and daily life. It is my pleasure to have been working with these smart and nice friends. Finally, I am grateful to my girlfriend and families, whom I owe too much. It is the concern and the support from my parents and the other relatives that make me work and live happily.

TABLE OF CONTENTS

	Page
LIST OF TABLES	vi
LIST OF FIGURES	vii
ABSTRACT	xiii
CHAPTER 1. INTRODUCTION	1
1.1 Classification of Solids by Band Structures	2
1.2 Interaction of Ultrafast Laser and Metals	8
1.3 Interaction of Ultrafast Laser and Semiconductors	11
1.4 Objectives and Organizations of This Thesis	13
CHAPTER 2. EXPERIMENTAL SETUP FOR DETECTION AND CHARACTERIZATION	15
2.1 Ultrafast Time-Resolved Spectroscopy	15
2.2 Transient Reflectance and Dynamics of Energy Carriers	18
2.3 Characterization of Ultrafast Laser Pulses	20
2.4 Summary	26
CHAPTER 3. ELECTRON-PHONON COUPLING ACROSS METAL- DIELECTRIC INTERFACE	27
3.1 Transient reflectance Measurement on Gold Films Using 400 nm Pump and 800 nm Probe	28
3.2 Calculation of the Energy-Carrier Temperatures Using the TTM	31
3.3 Energy Coupling Strength Across Metal-Dielectric Interface	36
3.4 Summary	38
CHAPTER 4. TRANSIENT DYNAMICS OF CARRIERS DETECTED BY ULTRAFAST SPECTROSCOPY WITH TUNABLE LASER WAVELENGTH	40

	Page
4.1 Dynamics of Photoexcited Carriers in Gold	40
4.1.1 Band Structure of Gold and Experimental Configuration.....	41
4.1.2 Transient Reflectance Measurement on Gold Films Using 800 nm Pump with Varying Probe Wavelength	42
4.1.3 Influence of Nonthermalized Electrons.....	46
4.1.4 Analysis of the Carrier-Phonon Coupling Rate.....	49
4.2 Dynamics of Photoexcited Carriers in GaAs	54
4.2.1 Transient Reflectance Measurement on GaAs with Excitation Across the Band Gap	55
4.2.2 Transient Reflectance Measurement on GaAs with Free Carrier Excitation	60
4.3 Summary	65
CHAPTER 5. DYNAMICS OF ENERGY CARRIERS IN SKUTTERUDITES DETECTED BY ULTRAFAST SPECTROSCOPY	66
5.1 Interaction Between Guest Atoms and the Host Lattice in Filled Skutterudites	66
5.1.1 Background	66
5.1.2 Transient Reflectance Measurement on Filled Skutterudites Using 400 nm Pump and 800 nm Probe	68
5.1.3 Identification of the Oscillation Modes.....	71
5.1.4 Effect of the Resonant Interaction on Lattice Thermal Conductivity	74
5.2 Dynamics of Photoexcited Carriers in Skutterudites	77
5.2.1 Band Structure of Skutterudites	77
5.2.2 Transient Reflectance Measurement on Filled Skutterudites Using 800 nm Pump and Probe with Varying Wavelength.....	79
5.3 Summary	86
CHAPTER 6. CONCLUSIONS AND FUTURE WORK.....	87
6.1 Summary and Conclusions.....	87

	Page
6.2 Future Work	88
LIST OF REFERENCES	90
VITA	98

LIST OF TABLES

Table	Page
Table 3.1. Properties and parameters used in the simulation by the TTM.	34
Table 5.1. Fitting parameters for k_L (ω_o and τ_o are experimentally determined values)... ..	75
Table 5.2. Fitting parameters for the transient reflectance signals of skutterudites.	83

LIST OF FIGURES

Figure	Page
Figure 1.1. Distributions of the probability density for finding an electron at position x .	3
Figure 1.2. Square-well periodic potential used in the Kronig-Penney model (a specifies the width of the well and b specifies the width of the high-level potential)....	5
Figure 1.3. The left hand side of (1.13) as a function of Ka .	6
Figure 1.4. Electron occupancy in energy bands of different types of solids: insulator, metal, metal, semimetal, intrinsic semiconductor, and extrinsic semiconductor (from left to right), with white part indicating empty bands and gray part indicating filled bands.	8
Figure 1.5. Three steps of heating of metals by ultrafast laser: (a) nonequilibrium among electrons; (b) nonequilibrium between electrons and phonons; (c) equilibrium between electrons and phonons.	9
Figure 1.6. Photoexcitation and relaxation of energy carriers in semiconductors: (a) photoexcitation of electrons and holes; (b) momentum randomization among electrons and holes; (c) thermalization of electrons and holes; (d) carrier-phonon scattering.	11
Figure 2.1. Optical setup for transient reflectance measurement.	16
Figure 2.2. Signal processing for transient reflectance measurement.	18

Figure	Page
Figure 2.3. Noncollinear scheme for correlation measurement using SHG.	
Note: there will be both SHG and residual fundamental beams in the side arms after the BBO crystal.	22
Figure 2.4. Autocorrelation trace of ultrafast laser pulses (Qiu, <i>et al.</i> , 1994).	23
Figure 2.5. Illustration of single-shot autocorrelation.	24
Figure 2.6. Cross-correlation trace of ultrafast laser pulses.	26
Figure 3.1. Transient reflectance signals for the 77 nm-thick gold film with different pump fluencies: (a) before stretching the pump pulse; (b) after stretching the pump pulse.	29
Figure 3.2. Transient reflectance measurement results for gold films of varying thicknesses on silicon.	30
Figure 3.3. Simulation results with varying R_{es} for the sample with a 39 nm-thick gold film: (a) $R_{ps}=1\times 10^{-10}$ m ² K/W; (b) $R_{ps}=1\times 10^{-7}$ m ² K/W.	36
Figure 3.4. Comparison between the measurement and the simulation results for samples of varying gold thicknesses. The open circle represents the measured data and the solid line represents the simulation results. (a) 39 nm fitted by $R_{es}=5\times 10^{-10}$ m ² K/W; (b) 46 nm fitted by $R_{es}=6\times 10^{-10}$ m ² K/W; (c) 60 nm fitted by $R_{es}=1.2\times 10^{-9}$ m ² K/W; (d) 77 nm fitted by $R_{es}=1.8\times 10^{-9}$ m ² K/W.	37
Figure 4.1. Qualitative illustration of the DOS of gold: the light and the dark blue regions indicate the <i>s/p</i> and the <i>d</i> bands, respectively, which overlap partially in energy; the red and the yellow arrows indicate transition from the <i>d</i> band to states below and above E_F	42

Figure	Page
Figure 4.2. (a) Transient reflectance signals of gold by 800 nm pump and varying probe wavelength; (b) Dependence of the amplitude of the transient reflectance signal on the probe photon energy (The horizontal dashed line marks $\Delta R/R = 0$ and the vertical dashed line marks the energy equal to the ITT).	44
Figure 4.3. Calculated probe photon energy dependence of $\Delta R/R$ and $\Delta T/T$ for a 20 nm-thick gold film for the initial nonthermalized electron distribution (dashed lines) and the thermalized electron distribution (solid lines) from the work by Sun, <i>et al.</i> (1994).....	44
Figure 4.4. (a) The Fermi-Dirac distribution at varying temperature; (b) Difference in the Fermi-Dirac distribution between $T_e = E_F/50k_B$ and $T_e = E_F/20k_B$	45
Figure 4.5. (a) Dependence of max ΔT_e on the pump fluence probed by 490 nm; (b) Dependence of amplitude of the transient reflectance signal on max ΔT_e probed by 490 nm with linear fitting indicated by the black line.	46
Figure 4.6. Comparison between the change of the electron distribution due to nonthermalized electrons based on (4.1) and due to thermalized electrons (The vertical dashed line indicates the states probed by 800 nm).	47
Figure 4.7. Transient reflectance signals of gold films of varying thickness excited by 1300 nm and probed by 800 nm.	49
Figure 4.8. Dependence of the electron relaxation time on the probe wavelength: (a) probe photon energy below ITT; (b) probe photon energy above ITT.	51

Figure	Page
Figure 4.9. Comparison between the transient reflectance signals of bulk gold with the ΔT_e calculated by the TTM for pump fluence (a) 1.76 mJ/cm ² ; (b) 3.52 mJ/cm ² ; (c) 5.28 mJ/cm ² ; (d) 7.04 mJ/cm ²	53
Figure 4.10. (a) Illustration of photoexcitation across the band gap; (b) Illustration of cooling of photoexcited carriers with the solid areas denoting the carrier distribution. The purple and the blue arrows indicate photon energies at which bandfilling occurs.....	56
Figure 4.11. Evolution of $\varepsilon = \varepsilon_1 + i\varepsilon_2$ after photoexcitation.....	57
Figure 4.12. Transient reflectance measurement results on GaAs by (a) 610 nm pump and 800 nm probe and (b) 800 nm pump and 610 nm probe.....	59
Figure 4.13. Calculated $\Delta R/R$ versus the carrier temperature T for 307.5 nm pump and 615 nm probe. The volumetric densities of photoexcited electrons and holes are both 10 ¹⁹ cm ⁻³ . The sum of the mean electron energy $\langle E_e \rangle$ and the mean hole energy $\langle E_h \rangle$ is also plotted versus T . The black dot-dash line shows the classical value of $\langle E_e \rangle + \langle E_h \rangle$, $3k_B T$. T_i indicates the carrier temperature immediately after the excitation and the red dashed lines mark the values of T and $\langle E_e \rangle + \langle E_h \rangle$, at which $\Delta R = 0$. The plot is from the work by Shank, <i>et al.</i> (1978).....	60
Figure 4.14. Band structure of GaAs (http://www.ioffe.ru/SVA/NSM/Semicond/GaAs/bandstr.html). The red and the orange arrows indicate transitions by optical excitation.....	62
Figure 4.15. Transient reflectance signals of <i>n</i> -type GaAs by 1400 nm pump with fluence 4.48 mJ/cm ² and varying probe wavelength.	63

Figure	Page
Figure 4.16. Transition analysis for GaAs: (a) energy states probed by varying probe wavelength (The blue area indicates the cold electron distribution while the red area indicates the hot electron distribution; The thick arrow indicates the excitation by the pump while the thin arrows indicate transitions by the probe.); (b) effect of two possible transitions for one probe wavelength (The thin arrows indicate transitions by the probe.).....	64
Figure 5.1. Unit cell of the binary skutterudite crystal structure (Morelli, <i>et al.</i> , 1995). The gray circle represents the pnictide atom and the black circle represents the transition metal atom.....	67
Figure 5.2. Transient reflectance signals of the filled skutterudites: (a) Ba-filled; (b) Yb-filled; (c) La-filled; (d) triple-filled (magnified in the insets).....	70
Figure 5.3. Transient reflectance signals of the filled skutterudites: (a) $\text{Mm}_{0.82}\text{Fe}_4\text{Sb}_{11.96}$; (b) $\text{Mm}_{0.72}\text{Fe}_{3.43}\text{Co}_{0.57}\text{Sb}_{11.97}$; (c) $\text{Mm}_{0.65}\text{Fe}_{2.92}\text{Co}_{1.08}\text{Sb}_{11.98}$; (d) $\text{Mm}_{0.55}\text{Fe}_{2.44}\text{Co}_{1.56}\text{Sb}_{11.96}$ (Mm represents misch-metal atoms).....	71
Figure 5.4. Normalized spectrums of the transient reflectance signals of the filled skutterudites.	72
Figure 5.5. Raman spectrums of the filled skutterudites.	73
Figure 5.6. Comparison between the measured and the fitted k_L	75
Figure 5.7. Comparison of each scattering term at the resonance frequency and 300 K in (5.2).	76
Figure 5.8. Band structure and DOS of $\text{BaFe}_4\text{Sb}_{12}$ (Takegahara, <i>et al.</i> , 2008).	78

Figure	Page
Figure 5.9. Transient reflectance signals of $\text{Mm}_{0.65}\text{Fe}_{2.92}\text{Co}_{1.08}\text{Sb}_{11.98}$ with pump wavelength 800 nm, probe wavelength: (a) 1500 nm, 1300 nm, and 1200 nm; (b) 1000 nm, 950 nm, and 900 nm; (c) 722 nm, 650 nm, 610 nm, and 580 nm.	79
Figure 5.10. Change of the dielectric constant due to the pseudogap shrinkage induced by lattice heating.	81
Figure 5.11. Transient reflectance signal of $\text{Mm}_{0.65}\text{Fe}_{2.92}\text{Co}_{1.08}\text{Sb}_{11.98}$ with pump wavelength 800 nm, probe wavelength 1500 nm (a) by fluence 0.42 mJ/cm^2 together with the fitting result by the model described in (5.3); (b) at varying pump fluence after normalization.	83
Figure 5.12. Transient reflectance signals of $\text{Mm}_{0.65}\text{Fe}_{2.92}\text{Co}_{1.08}\text{Sb}_{11.98}$ with probe wavelength 1300 nm, 1200 nm, 1000 nm and 900 nm shown in a long-time scale (The first oscillation peak is marked by the dashed line).	85

ABSTRACT

Guo, Liang. Ph.D., Purdue University, December, 2014. Dynamics of Energy Carriers in Solids During Interaction with Ultrafast Laser Pulses. Major Professor: Dr. Xianfan Xu, School of Mechanical Engineering.

The dynamics of energy carriers, including mainly electrons, holes, and phonons, determine important physical properties of solids such as thermal conductivity and electrical conductivity, which affect the design and the performance of solid-state devices. Solids can be classified as metal, semimetal, semiconductor, and insulator according to the band structure. Different kinds of solids have some common features but are generally distinct in terms of the energy-carrier dynamics.

Ultrafast spectroscopy is a powerful tool to examine the dynamics of energy carriers, which excites a transient response of the material by a short laser pulse and detects the response by optical observables such as reflectance and transmittance. This technique allows observation of the optical response, which is closely related to the dynamics of energy carriers, in the time domain with a high temporal resolution on the order of 10 fs. In this thesis, ultrafast spectroscopy is used to investigate the behavior of electrons, holes, and phonons in metals and semiconductors.

For metals, the dynamics of energy carriers is relatively well understood. Our work focuses on energy transport in gold as demonstration. By measuring the transient reflectance of gold films and analyzing the measured signals with the two-temperature model (TTM), it is found that during the transient heating process, when electrons and phonons are in thermal nonequilibrium state, electrons in metal thin films can directly transfer energy to phonons in dielectric substrates. In addition, the effect of the probe wavelength on the transient reflectance signal of gold is analyzed, which provides comprehensive information about the carrier dynamics and helps to optimize the experimental configuration for facilitating the analysis. For semiconductors, there is much less detailed work on the energy-carrier dynamics due to the typically complicated and diverse band structures. In our work, the carrier dynamics of gallium arsenide (GaAs) is investigated using ultrafast spectroscopy due to its well-known band structure, which serves as a reference for materials with more complex band structures. Based on the information obtained from the analysis of GaAs, we explore the carrier dynamics of filled-skutterudites, which is an important thermoelectric material. It is found that the transient reflectance signals of skutterudites are mainly attributed to bandfilling and lattice heating, which can reflect the relaxation of photoexcited carriers.

In addition to the dynamics of electrons and holes, lattice vibration can also be manifested in the time domain by ultrafast spectroscopy. Our study shows that the guest atoms added to the voids in the lattice structure of skutterudites can interact with the host lattice and form lattice vibration modes by resonant interaction and different species of guest atoms lead to such vibration modes with different frequencies, which can scatter phonons in a broad spectral span. Therefore, filling skutterudites with multiple species of

atoms can reduce the lattice contribution to the thermal conductivity more effectively and improve the thermoelectric performance.

For future work, the acquired information from the studied materials can be applied to investigate materials with potential and important application such as black phosphorene and molybdenum disulfide (MoS_2). Ultrafast spectroscopy can be carried out by different pump and probe wavelengths at varying temperatures and fluences to provide comprehensive information about the properties of energy carriers. The ultimate goal is to fully understand the energy-carrier dynamics in solid materials and to guide the design of solid-state devices.

CHAPTER 1. INTRODUCTION

Study of properties of solids is an important branch of physics since solids constitute most of the appliances used in daily life and industry. An essential consideration in the design and utilization of solid-state devices involves the thermal transport properties of solids, which are determined by the dynamics of energy carriers from a microscopic viewpoint. Ultrafast spectroscopy based on ultrafast laser has been widely used for the study of the dynamics of energy carriers in solids including mainly electrons, holes, and phonons. On one hand, the properties of energy carriers, such as relaxation time and phonon frequencies, can be extracted by this technique. On the other hand, the interaction of energy carriers among themselves and with photons during the laser heating can be investigated. Such studies can also provide guidance for the choice of parameters in laser processing, which is widely used in industry due to its advantages such as high instantaneous power, high precision, and small heat-affected zone.

In this chapter, the classification of crystals according to the features of the band structures and the electron occupancy is introduced, which is the basis for studying solid-laser interaction. Then the general physical processes during the interaction of ultrafast laser with metals and semiconductors are discussed. The last section describes the objectives and the organization of this thesis.

1.1 Classification of Solids by Band Structures

The introduction in this section is based on the two books by Kittel (2005) and Ashcroft (1976).

The free electron model allows the electron energy to range from zero to infinity, which works well for predicting properties related to the kinetic properties of electrons in the conduction band such as thermal conductivity of metals but ignores the electron-lattice interaction. When the effect on electrons of the periodic potential of the lattice is considered, Bragg reflection causes the formation of a band gap, referring to the energy region where no wavelike electron orbitals exist.

The free electron wavefunction has the form of a running wave:

$$\psi_{\mathbf{k}}(\mathbf{r}) = \exp(i\mathbf{k} \cdot \mathbf{r}), \quad (1.1)$$

where \mathbf{k} represents the wavevector and \mathbf{r} represents the spatial coordinate. During the propagation of such a wave in the lattice, Bragg reflection occurs when

$$(\mathbf{k} + \mathbf{G})^2 = k^2 \quad (1.2)$$

is satisfied where \mathbf{G} represents a reciprocal lattice vector. In one dimension, for simplicity, with the lattice constant equal to a , the condition is satisfied when $k = n\pi/a$, where n is an integer. At these values of k , the traveling wave is Bragg-reflected into the inverse direction, so the wavefunction consists of wave components traveling in opposite directions, resulting in two standing waves:

$$\psi(+) = \exp(i\pi x/a) + \exp(-i\pi x/a) = 2\cos(\pi x/a), \quad (1.3a)$$

$$\psi(-) = \exp(i\pi x/a) - \exp(-i\pi x/a) = 2i\sin(\pi x/a). \quad (1.3b)$$

Therefore, the probability density of finding an electron at position x is determined by

$$\rho(+) = |\psi(+)|^2 \propto \cos(\pi x/a), \quad (1.4a)$$

$$\rho(-) = |\psi(-)|^2 \propto \sin(\pi x/a). \quad (1.4b)$$

The two different distributions of the probability density pile up electrons in different regions in the crystal as plotted in Fig. 1.1, in which normalization over unit length is taken to compare the magnitudes. For a traveling wave with a wavefunction in the form of (1.1), the probability density is constant and also plotted in Fig. 1.1 with normalization considered. It is seen that $\rho(+)$ concentrates electrons at $x = 0, \pm a, \pm 2a, \dots$ on the positive ions while $\rho(-)$ concentrates electrons at $x = 0, \pm a/2, \pm 3a/2, \dots$ off the positive ions. Since the force between the positive ions and the negative electrons is attractive, $\rho(+)$ renders a lower average potential than the traveling wave does while $\rho(-)$ renders a higher average potential. This difference creates a band gap.

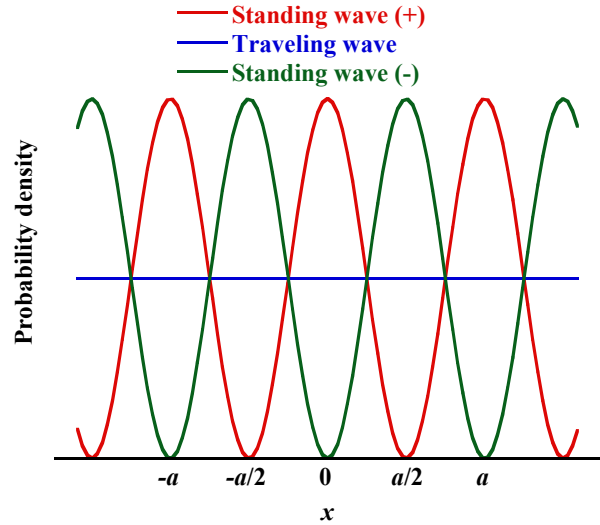


Figure 1.1. Distributions of the probability density for finding an electron at position x .

A more quantitative analysis is given by the Kronig-Penney model, which assumes the lattice introduces a square-well periodic potential, as shown in Fig. 1.2. The time-independent Schrödinger equation for the electron wavefunction is

$$-\frac{\hbar^2}{2m} \frac{d^2\psi}{dx^2} + U(x)\psi = \varepsilon\psi \quad (1.5)$$

where $U(x)$ is the potential function and ε is the energy eigenvalue. In the region $0 < x < a$, the eigenfunction has the form

$$\psi = A \exp(iKx) + B \exp(-iKx) \quad (1.6)$$

with the energy eigenvalue

$$\varepsilon = \frac{\hbar^2 K^2}{2m}. \quad (1.7)$$

In the region $-b < x < 0$, the eigenfunction has the form

$$\psi = C \exp(Qx) + D \exp(-Qx) \quad (1.8)$$

with the energy eigenvalue

$$\varepsilon = U_0 - \frac{\hbar^2 Q^2}{2m}. \quad (1.9)$$

According to the Bloch theorem, which specifies the features of the wavefunction in a periodic potential, the solution in the region $a < x < a+b$ should be related to that in the region $-b < x < 0$ by

$$\psi(a < x < a + b) = \psi(-b < x < 0) \exp[ik(a + b)]. \quad (1.10)$$

The solution should be continuous and have continuous first derivative at $x = 0$ and $x = a$, which require that

$$A + B = C + D, \quad (1.11a)$$

$$iK(A - B) = Q(C - D), \quad (1.11b)$$

$$A \exp(iKa) + B \exp(-iKa) = [C \exp(-Qb) + D \exp(Qb)] \exp[ik(a + b)], \quad (1.11c)$$

$$\begin{aligned} iK[A \exp(iKa) - B \exp(-iKa)] = \\ Q[C \exp(-Qb) - D \exp(Qb)] \exp[ik(a + b)]. \end{aligned} \quad (1.11d)$$

These four equations are solvable only if the determinant of the coefficients of A , B , C , and D vanishes, which requires that

$$[(Q^2 - K^2)/2QK] \sinh(Qb) \sin(Ka) + \cosh(Qb) \cos(Ka) = \cos[k(a + b)]. \quad (1.12)$$

For simplicity, the case is considered in which the potential becomes a periodic delta function in such a way that $Q^2 ba/2 = P$, a finite quantity. In this case, (1.12) becomes

$$(P/Ka) \sin(Ka) + \cos(Ka) = \cos(ka). \quad (1.13)$$

The left hand side of (1.13) is plotted in Fig. 1.3 for $P = 1.5\pi$. It is seen that solutions of k exist only for certain values of K that make the left hand side of (1.13) lie between -1 and +1 since the right hand side is a cosine function. From (1.7), this predicts the existence of a band gap, in which no solutions of k exist. This gap is raised when $\cos(ka) = \pm 1$ or when $k = n\pi/a$, consistent with the analysis by Bragg reflection.

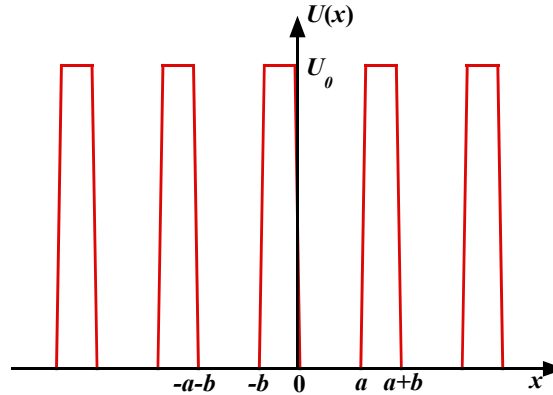


Figure 1.2. Square-well periodic potential used in the Kronig-Penney model (a specifies the width of the well and b specifies the width of the high-level potential).

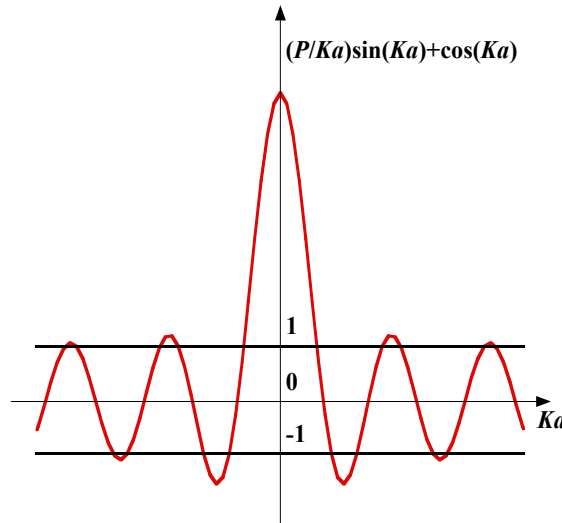


Figure 1.3. The left hand side of (1.13) as a function of Ka .

In a crystal, each primitive cell contributes one independent value of k to each energy band. A crystal containing N primitive cells has $2N$ independent orbitals in each energy bands considering the spin orientation. Depending on the number of atoms in each primitive cell, the number of valence electrons donated by each atom, and the overlapping of bands in energy, the occupation of energy bands varies with crystal species. If valence electrons completely fill some bands, leaving the other bands empty and the highest filled band is separated from the lowest empty band by a considerable energy gap, electrons cannot move even when an external electric field is applied provided it is not too strong and such a solid is an insulator. If valence electrons completely filled some bands and partially filled some other bands, then the electrons in the partially-filled bands can move under an external electric field and such a solid is a metal. If valence electrons can completely fill some bands but the highest filled band overlaps with the lowest empty band in energy, then both the bands will be partially filled,

which also results in a metal. If such an overlap is small, the solid is also called a semimetal. At 0 K, perfect crystals are classified unambiguously as metals or insulators depending on whether there are any partially-filled energy bands. The conduction band, which is usually the partially filled band, is the range of electron energy sufficient to free an electron from binding with its atom and allow it to move freely within the lattice. The valence band, which is usually the completely filled band, is the range of electron energy in which electrons are bound to individual atoms. The band gap is the difference in energy between the lowest point of the conduction band (the conduction band edge) and the highest point of the valence band (the valence band edge). If the minimum of the conduction band and the maximum of the valence band have the same wave vector, such a band gap is called a direct band gap. It is called an indirect band gap otherwise and transition across an indirect band gap usually requires phonon absorption or emission.

At elevated temperature, however, some solids which are insulators at zero temperature and have small band gap can have partially-filled energy bands due to thermal excitation of electrons. Such solids are called intrinsic semiconductors. Impurities can contribute electrons which are easily thermoexcited into otherwise empty bands and make insulators become semiconductors. Such doped solids are called extrinsic semiconductors. Fig. 1.4 shows the qualitative band structures and the electron occupancy of the types of solids discussed above.

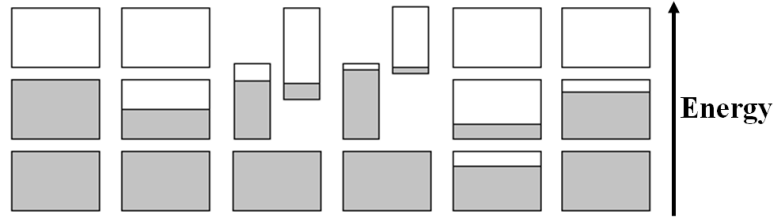


Figure 1.4. Electron occupancy in energy bands of different types of solids: insulator, metal, metal, semimetal, intrinsic semiconductor, and extrinsic semiconductor (from left to right), with white part indicating empty bands and gray part indicating filled bands.

1.2 Interaction of Ultrafast Laser and Metals

In metals, the electrons in the conduction band, which are almost free to move, usually play a more important role in the interaction with laser than the bound electrons in the valence band. Generally, heating of metals by ultrafast laser can be described as three steps (Hohlfeld, *et al.*, 2000), illustrated in Fig. 1.5. The heating energy is first absorbed by some electrons near the Fermi energy E_F , which are excited to higher energy levels. This leaves the electrons in a nonequilibrium state characterizing the first step (Fig. 1.5(a)). Two competing processes dominate this step. One is the ballistic motion of the excited electrons into the deeper part of the material roughly at the Fermi velocity. The other is the development of a temperature of the free electrons. The excited electrons and mainly the electrons near E_F exchange energy by collisions and finally electrons reach equilibrium, characterized by the Fermi-Dirac distribution with a defined temperature (T_e). Then the second step begins, in which electrons have a much higher temperature than phonons (T_p) (Fig. 1.5(b)). The hot electrons initially close to the sample surface diffuse into the deeper part of the material driven by the temperature gradient. Meanwhile, the hot electrons are cooled down by the cold lattice through electron-phonon scattering.

At the end of the second step, electrons and phonons reach equilibrium at a common temperature (Fig. 1.5(c)). Phonons generally have a much larger heat capacity than electrons and therefore the equilibrium temperature is much lower than the maximum of T_e . In the third step, heat transport is driven by the remaining smaller temperature gradient and progresses slowly.

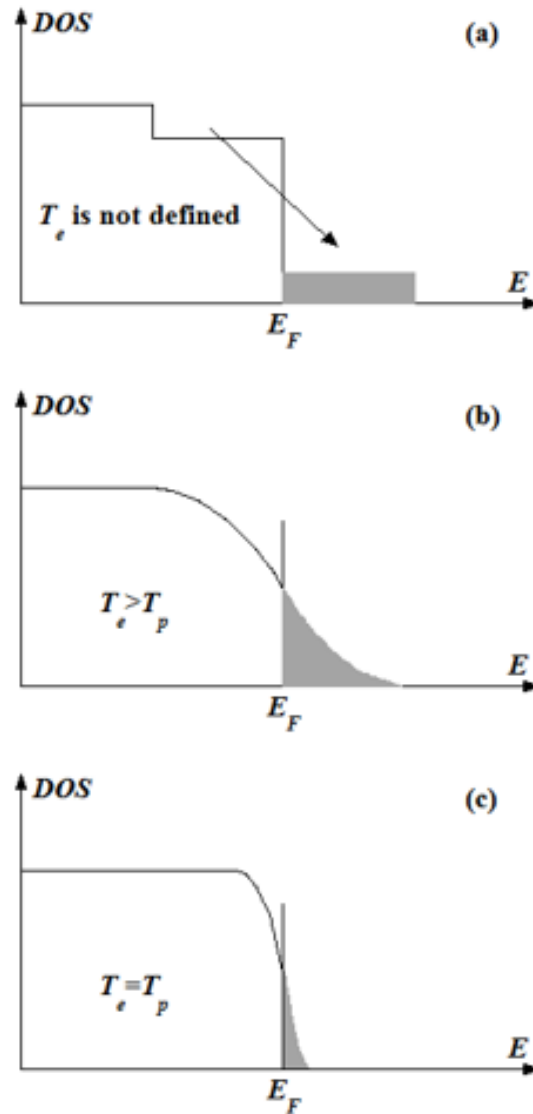


Figure 1.5. Three steps of heating of metals by ultrafast laser: (a) nonequilibrium among electrons; (b) nonequilibrium between electrons and phonons; (c) equilibrium between electrons and phonons.

Kaganov, *et al.* (1957) first theoretically investigated the energy exchange between electrons and phonons and Anisimov, *et al.* (1974) developed a two-temperature model (TTM) to quantify electron-phonon coupling during the heating process of metals by ultrafast laser:

$$C_e \frac{\partial T_e}{\partial t} = \frac{\partial}{\partial x} \left(k_e \frac{\partial T_e}{\partial x} \right) - G(T_e - T_p) + S, \quad (1.14a)$$

$$C_p \frac{\partial T_p}{\partial t} = G(T_e - T_p). \quad (1.14b)$$

Here T denotes the temperature, C represents the heat capacity, k denotes the thermal conductivity, t is the time and x is the spatial coordinate. Subscripts e and p indicate “electron” and “phonon” respectively. G is the electron-phonon coupling factor, characterizing the rate of energy coupling between electrons and phonons. S represents the laser heating source. Physically, when the heating is fast or the pulse duration is much shorter than the characteristic time for electrons and phonons to reach equilibrium, which is determined by C_e and G , electrons and phonons will have different temperatures immediately after the heating pulse.

If the pulse duration is much longer than the electron-phonon coupling time, electrons and phonons have a common temperature and the TTM turns into the one-temperature model:

$$C \frac{\partial T}{\partial t} = \frac{\partial}{\partial x} \left(k \frac{\partial T}{\partial x} \right) + S, \quad (1.15)$$

which can be derived from Fourier’s law.

1.3 Interaction of Ultrafast Laser and Semiconductors

The wide use of semiconductor devices excites the interest in investigating the dynamics of energy carriers in semiconductors. Ultrafast laser serves as a powerful tool to excite semiconductors into a nonequilibrium state and probe the relaxation process of energy carriers. Typical relaxation processes were reviewed by Othonos (1998) and are illustrated here in Fig. 1.6.

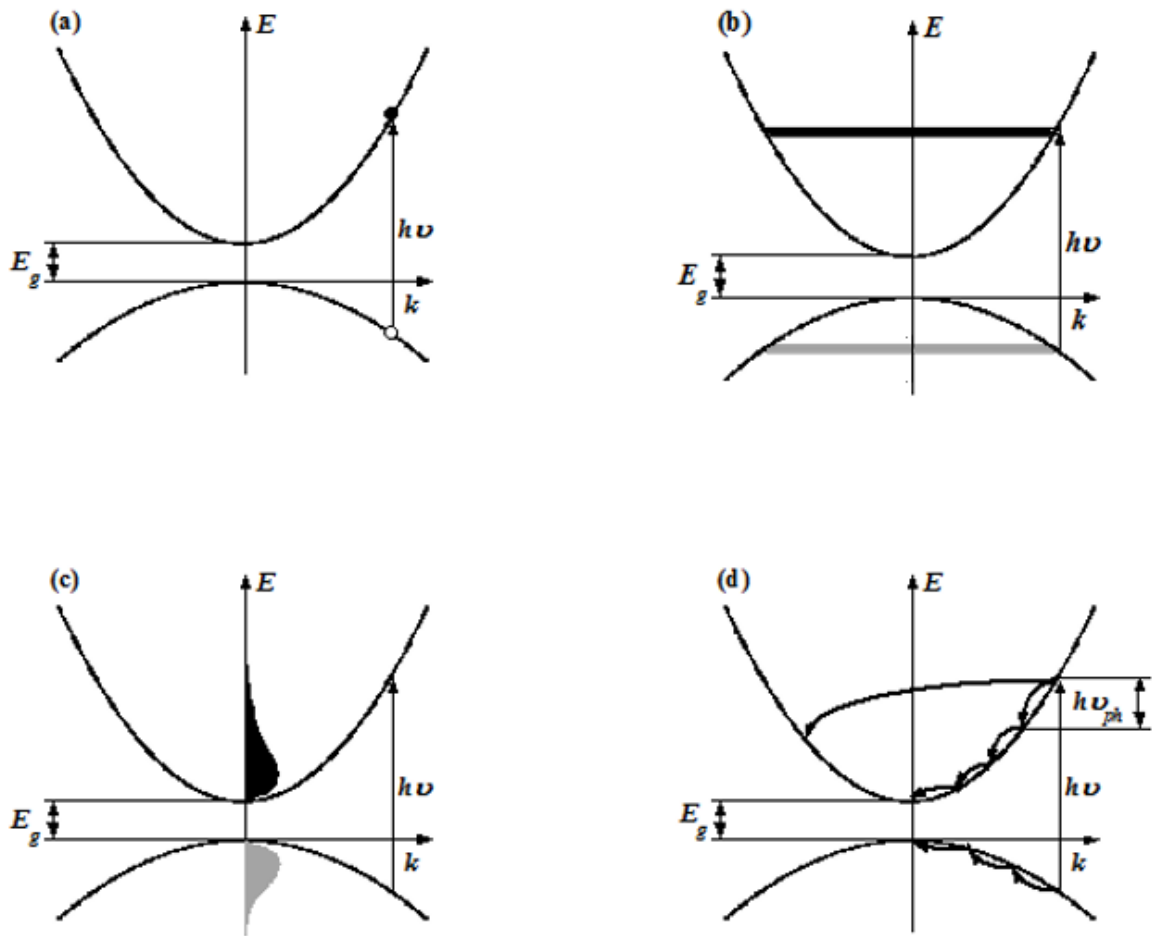


Figure 1.6. Photoexcitation and relaxation of energy carriers in semiconductors: (a) photoexcitation of electrons and holes; (b) momentum randomization among electrons and holes; (c) thermalization of electrons and holes; (d) carrier-phonon scattering.

If the incident photon energy $h\nu$ (h is the Planck constant and ν the frequency) is greater than the band gap E_g , electrons in the valence band will absorb photons and be excited into the conduction band, leaving holes in the valence band (Fig. 1.6(a)). The excitation energy is initially stored in electrons and holes, exciting them into nonequilibrium states. Momentum randomization among the carriers by scattering can be finished within tens of femtoseconds (Fig. 1.6(b)). Carrier-carrier collisions generally take less than 1 ps to thermalize electrons and holes into equilibrium states. After the thermalization, electrons and holes can be described by the Fermi-Dirac distribution with individual temperatures T_e and T_h (Fig. 1.6(c)). The subsequent relaxation of carriers is mainly through scattering among carriers and phonons (Fig. 1.6(d)). Intervalley scattering of carriers is associated with emission of long wave-vector phonons while intravalley scattering of carriers is realized by emission of short wave-vector phonons. Carriers are cooled down and phonons are heated until they reach equilibrium. The interaction between carriers and phonons typically lasts more than 1 ps. Electron-hole recombination, which brings the excited electrons back to the valence band and fills the holes, can happen either radiatively or nonradiatively (en.wikipedia.org). In the radiative way, an electron-hole pair recombines and releases its energy by emitting a photon. Since the photon has zero momentum, this kind of recombination must occur as a direct transition and thus is important only in materials with direct band gap. The Auger recombination is nonradiative, in which the released energy from an electron-hole pair is transferred to a third carrier and excites it to a higher energy level. The Auger recombination is only significant in nonequilibrium states with high carrier density. Impurities can create energy states within the band gap, called localized states. Interactions with localized

states contribute to the elimination of the momentum difference between carriers and the energy is released in the form of a phonon. Such a recombination is called the Shockley-Read-Hall (SRH) process, which is the dominant recombination mechanism in materials with indirect band gap and is also important in materials with direct band gap when the carrier density is low. The recombination process typically lasts more than 100 ps.

The interaction of solids with ultrafast laser is often more complex than those basic processes described in this section and Section 1.2. For example, if the photon energy used for excitation is large enough, interband transitions can also occur in metals with part of the bound electrons excited and if the photon energy is smaller than the band gap, excitation can only happen within the conduction band for *n*-type semiconductors or the valence band for *p*-type semiconductors. These may complicate the physical analysis (Hopkins, *et al.*, 2008) and may also help to isolate the dynamics of specified energy carriers (Ye, *et al.*, 1999 and 2000). Some special physical processes occurring for certain materials will be introduced later.

1.4 Objectives and Organizations of This Thesis

In this thesis, dynamics of energy carriers, including electrons, holes, and phonons, in metals and semiconductors is inspected in the time domain by ultrafast spectroscopy. Chapter 2 introduces the ultrafast spectroscopy experiment system for transient reflectance measurement and the related techniques for characterizing the ultrafast laser pulse. Chapter 3 presents the study of energy coupling across metal-dielectric interfaces, from which it is found that electrons in the metal layer can transfer energy directly to phonons in the dielectric layer. Chapter 4 demonstrates detection of the

carrier dynamics by transient reflectance measurement. Excitation and relaxation of carriers are analyzed through the Kramers-Kronig relations for metals and semiconductors. Gold and gallium arsenide are selected for demonstration of the analysis. By an optical parametric amplifier (OPA), probe with tunable wavelengths is produced and used to sense different electronic energy levels, which provides more physical information compared with single-wavelength detection. Chapter 5 illustrates detection of energy-carrier dynamics for skutterudites, a thermoelectric material with complicated band structure, by ultrafast spectroscopy. The resonant interaction mode of the guest atoms and the host lattice in filled skutterudites is detected and its effect on the lattice thermal conductivity is discussed. Carrier dynamics in skutterudites is explored by probing with multiple wavelengths and it is found that the transient reflectance signals are mainly attributed to bandfilling and lattice heating. Chapter 6 summarizes the conclusions and recommends some future work.

CHAPTER 2. EXPERIMENTAL SETUP FOR DETECTION AND CHARACTERIZATION

This chapter introduces the experimental techniques used in this work including theories and optical arrangements. Section 2.1 describes the optical configuration and the signal processing for ultrafast spectroscopy. Section 2.2 analyzes the relation between the dynamics of energy carriers and the signal detected by ultrafast spectroscopy. Section 2.3 discusses the methods for characterizing short pulses.

2.1 Ultrafast Time-Resolved Spectroscopy

Spectroscopy based on ultrafast laser has been widely used for time-resolved study of transient dynamic processes in all kinds of materials. On one hand, ultrafast laser with pulse width shorter than the relaxation time of energy carriers can excite the material into nonequilibrium state. On the other hand, ultrafast laser pulses can be used as a flashing camera to record the transient excitation and the relaxation process, with temporal resolution comparable to the pulse width, which is not easily achieved by common electronics. Many ultrafast spectroscopy schemes have been invented to monitor different kinds of transient chemical or physical processes.

The ultrafast spectroscopy schemes used in this thesis includes a typical design for transient reflectance measurements as shown in Fig. 2.1. The femtosecond laser beam from a Ti:Sapphire system is centered at 800 nm with pulse width of about 70 fs

and repetition rate of 5 kHz. The beam is divided into two arms by a beam splitter. The more intense arm is used to excite materials, which is usually called the “pump” while the much weaker arm is used to detect the pump-induced reflectance change of the sample surface, which is usually called the “probe”. The probe is usually made weak to avoid strong excitation by itself. One of the two arms (here the probe) has tunable optical path length by a retroreflector mounted on a computer-controlled delay stage. The other arm (here the pump) has a fixed optical path designed to make sure that the two arms can have equal optical path lengths within the scanning range of the delay stage. Usually the pump and the probe are made optically distinguishable by either polarization or wavelength. Here the original 800 nm pump is converted into a 400 nm beam by a piece of barium borate (BBO) crystal while the probe is kept at 800 nm. A dichroic mirror which reflects the pump and passes the probe combines the two beams into a collinear scheme. A lens focuses the collinear beams onto the sample.

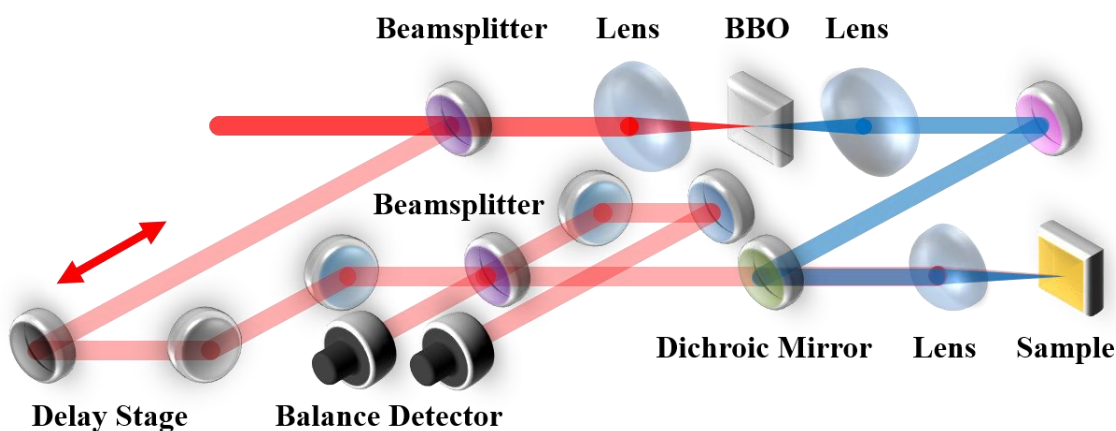


Figure 2.1. Optical setup for transient reflectance measurement.

The signal processing is shown in Fig. 2.2. The pump is modulated by a mechanical chopper with a certain frequency, inducing periodic change of the reflectance of the sample surface with period corresponding to the chopping frequency. If the delay stage introduces an optical path difference and thus a temporal delay Δt between the pump and the probe, the probe will see a reflectance equal to $R_0 + \Delta R(\Delta t)$ during the open window of the chopper and R_0 during the shut window, where R_0 denotes the reflectance without excitation and ΔR denotes the reflectance change. In order to increase the signal-to-noise ratio, a beam splitter is used to divide the probe into two arms as shown in Fig. 2.1. One of the arms is directed to the sample whose reflection is collected by a balance detector to make subtraction with the other arm without reflection, the “reference”. The intensities of the reflected probe and the reference are usually made roughly equal in the unperturbed state without the pump shot. Therefore, the balance detector generates photocurrent only during the open window of the chopper, when the intensity of the reflected probe differs from the unperturbed value. The output signal from the detector, which is also periodic with the chopping frequency, is filtered and amplified by a preamplifier and further filtered by a lock-in amplifier with the lock-in frequency set equal to the chopping frequency. The ideal signal cleaned by the lock-in amplifier should be a sinusoidal wave with the chopping frequency and amplitude proportional to $\Delta R(\Delta t)$. By translating the delay stage with fine enough steps, the transient dynamic process induced by the pump can be recorded in terms of $\Delta R(\Delta t)$. The setup introduced above is the basic scheme and some parameters such as laser wavelength can be tuned by additional devices to satisfy experimental requirements.

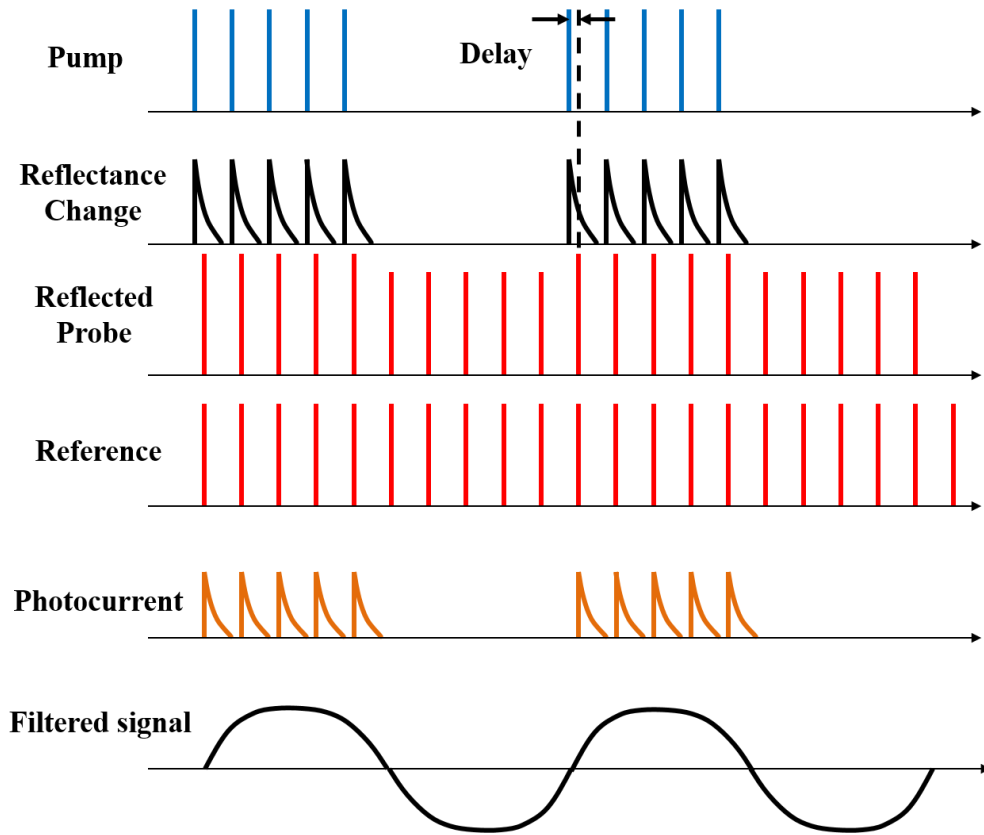


Figure 2.2. Signal processing for transient reflectance measurement.

2.2 Transient Reflectance and Dynamics of Energy Carriers

In order to obtain the information about the transport properties of energy carriers from transient reflectance measurement, the relation between transient reflectance and dynamics of energy carriers should be clarified. Generally, the optical properties of the excited sample undergo a transient change due to perturbation to the band structure and the electron occupancy.

The band structure or equivalently, the electron wavefunction, is determined by the potential function $U(x)$ in the Schrödinger equation (1.5). When the volumetric density of free carriers increases significantly due to excitation of bound electrons, the wavefunctions of individual carriers may overlap, resulting in a gas of interacting

particles. The Coulomb forces among electrons and holes will be enhanced and the Pauli exclusion principle prevents any pair of electrons or holes to occupy the same quantum state. The enhanced interaction among carriers induces a change of $U(x)$ and the band structure. The enhanced interaction among free electrons tends to reduce the energy of the conduction band edge while the enhanced interaction among holes tends to raise the energy of the valence band. The net results is a shrinkage of the band gap for semiconductors. In addition, when the lattice is heated by the hot carriers, the lattice constant increases for most materials, which tends to decrease $U(x)$ and also results in a shrinkage of the band gap. The perturbation to the electron occupancy is straightforward since more carriers occupy high energy states due to the excitation. For metal, the effect is the same for the shift of band energy except that the metal has no band gap.

The direct result of the perturbation to the band structure and the electron occupancy is modification of the imaginary part of the dielectric constant $\varepsilon(\omega) = \varepsilon_1(\omega) + i\varepsilon_2(\omega)$, since the absorption of light at certain wavelength can be either stronger or weaker. For example, if some states become more occupied, absorption due to transition to these states becomes weaker and the corresponding $\varepsilon_2(\omega)$ decreases. $\varepsilon_1(\omega)$ and $\varepsilon_2(\omega)$ are related by the Kramers-Kronig dispersion relations (Wooten, 1972):

$$\varepsilon_1(\omega_0) - 1 = \frac{2}{\pi} P \int_0^\infty \frac{\omega \varepsilon_2(\omega) d\omega}{(\omega^2 - \omega_0^2)}, \quad (2.1a)$$

$$\varepsilon_2(\omega_0) = -\frac{2\omega_0}{\pi} P \int_0^\infty \frac{[\varepsilon_1(\omega) - 1] d\omega}{(\omega^2 - \omega_0^2)}. \quad (2.1b)$$

Here P stands for principal value and ω_0 is a specific frequency at which $\varepsilon_1(\omega)$ and $\varepsilon_2(\omega)$ are evaluated. The differential form of either (2.1a) or (2.1b) renders the relation between the change of $\varepsilon_1(\omega)$ and $\varepsilon_2(\omega)$:

$$\Delta\varepsilon_1(\omega_0) = \frac{2}{\pi} P \int_0^\infty \frac{\omega \Delta\varepsilon_2(\omega)}{(\omega^2 - \omega_0^2) d\omega}. \quad (2.2)$$

$\Delta\varepsilon_2(\omega)$ can be calculated or estimated based on the band structure and the wavelength of the excitation light and the $\Delta\varepsilon_1(\omega)$ can be evaluated by (2.2).

The refractive index $n + ik$ is related to $\varepsilon = \varepsilon_1 + i\varepsilon_2$ by

$$n = \left[\frac{1}{2} (|\varepsilon| + \varepsilon_1) \right]^{\frac{1}{2}}, \quad (2.3a)$$

$$k = \left[\frac{1}{2} (|\varepsilon| - \varepsilon_1) \right]^{\frac{1}{2}}, \quad (2.3b)$$

where $|\varepsilon|$ means the magnitude of ε . The reflectance R can be calculated from n and k by

$$R = [(n - 1)^2 + k^2] / [(n + 1)^2 + k^2]. \quad (2.4)$$

From (2.3a), (2.3b) and (2.4), the relative change of R can be related to the change of ε through

$$\Delta R/R = (\Delta\varepsilon_1 \partial R / \partial \varepsilon_1 + \Delta\varepsilon_2 \partial R / \partial \varepsilon_2) / R, \quad (2.5)$$

$$(\partial R / \partial \varepsilon_1) / R = (2\varepsilon_1 - |\varepsilon| - 1) \sqrt{2(\varepsilon_1 + |\varepsilon|)} / |\varepsilon| / [(\varepsilon_1 - 1)^2 + \varepsilon_2^2], \quad (2.6a)$$

$$(\partial R / \partial \varepsilon_2) / R = \sqrt{2}\varepsilon_2 (2\varepsilon_1 + |\varepsilon| - 1) / |\varepsilon| / \sqrt{|\varepsilon| + \varepsilon_1} / [(\varepsilon_1 - 1)^2 + \varepsilon_2^2]. \quad (2.6b)$$

In transient reflectance measurement, $\Delta R(\Delta t)/R$ is measured versus the delay between the pump and the probe, Δt , and (2.2) to (2.6) are generally used for analyzing the variation of the band structure and the electron occupancy. Such analysis can provide information such as the relaxation of hot carriers, the heating of the lattice and the recombination of electrons and holes, which are directly related to the transport properties of energy carriers.

2.3 Characterization of Ultrafast Laser Pulses

Ultrafast laser usually has pulses with temporal width on the order of 1ps or shorter. Electronic devices generally do not respond fast enough to do accurate

measurement in this range. A common idea of characterizing ultrafast laser pulses is to use the short pulse itself as a fast camera, similar to ultrafast spectroscopy introduced in Section 2.1. Such methods include auto- or cross-correlation measurement, frequency-resolved optical gating (FROG), spectral phase interferometry for direct electric field reconstruction (SPIDER), spectrally and temporally resolved upconversion technique (STRUT) and so on. Each method may have several realization schemes. A detailed description of these methods can be found in the book by Weiner (2009). Several schemes of correlation measurement used in this thesis are introduced in this section based on this book.

One scheme of correlation measurement utilizing second harmonic generation (SHG) to record the correlation function is shown in Fig. 2.3. Two beams of the same wavelength are noncollinearly focused into a nonlinear crystal such as BBO and the power of the SHG generated by sum of the two arms is recorded as a function of the temporal delay τ between the two beams. The SHG beams and the residual fundamental beams from the individual arms are blocked by the iris and the residual fundamental beams are further cleared by the filter passing the wavelength of the SHG. The field incident on the crystal is the sum of the two input fields:

$$e(t) = \text{Re}[a_1(t)e^{j\omega t} + a_2(t - \tau)e^{j\omega(t-\tau)}], \quad (2.7)$$

where ω is the frequency and a is the amplitude. The second harmonic field is proportional to the square of the fundamental field and therefore the time-averaged power of the SHG follows the expression:

$$\langle P_{SHG}(t) \rangle \propto \langle |a_1(t)|^2 |a_2(t - \tau)|^2 \rangle \propto \int I_1(t) I_2(t - \tau) dt, \quad (2.8)$$

where I indicates intensity and “ $\langle \rangle$ ” means time-averaged quantity. From (2.7) to (2.8), the fast-oscillating terms and the constant background terms are dropped since they are suppressed in the noncollinear scheme. If the two input pulses are assumed to be Gaussian-like with $a_1(t) = \exp(-t^2/t_1^2)$ and $a_2(t) = \exp(-t^2/t_2^2)$, then the full widths at half maximum (FWHM) are $(2\ln 2)^{1/2}t_1$ and $(2\ln 2)^{1/2}t_2$, respectively. By (2.8),

$$\langle P_{SHG}(t) \rangle \propto \exp\left(-\frac{2\tau^2}{t_1^2 + t_2^2}\right), \quad (2.9)$$

which shows that the detected correlation trace has a FWHM equal to $[2\ln 2(t_1^2 + t_2^2)]^{1/2}$. When the two input pulses are the same, this scheme is called autocorrelation and the pulse width is given by dividing the correlation trace width by 1.414. When the two pulses are different, this scheme is called cross-correlation. If one pulse is much shorter than the other, the correlation trace width is close to the width of the longer pulse. Figure 2.4 presents an example of autocorrelation measurement. The autocorrelation trace is fitted by the Gaussian function, giving a FWHM of 140 fs and a pulse width (t_p) of 100 fs.

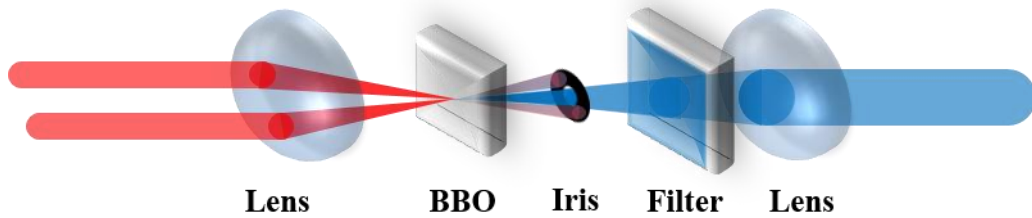


Figure 2.3. Noncollinear scheme for correlation measurement using SHG. Note: there will be both SHG and residual fundamental beams in the side arms after the BBO crystal.

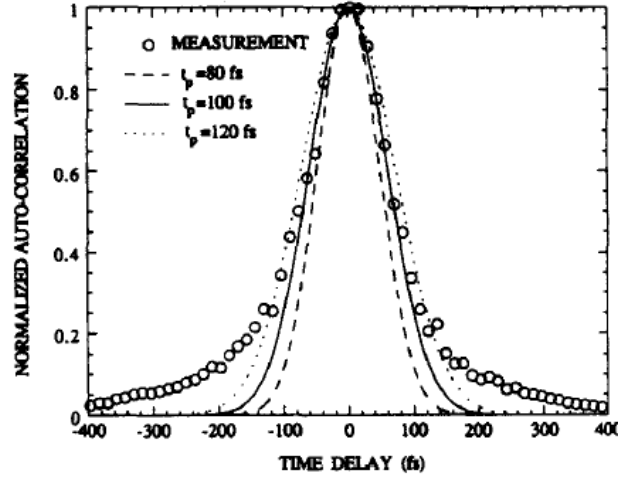


Figure 2.4. Autocorrelation trace of ultrafast laser pulses (Qiu, *et al.*, 1994).

Another scheme of autocorrelation works mainly for ultrafast laser with high pulse energy and large spot size, called single-shot autocorrelation (SSA). In this scheme, one beam is split into two arms, which cross in a nonlinear crystal at a certain angle after going through equal paths as shown in Fig. 2.5. At the center of the crossing area ($x = 0$), the temporal delay between the two arms is zero and the SHG is maximized. Away from the center, the delay varies as

$$\tau = 2x \sin(\theta/2)/c, \quad (2.10)$$

where x and θ are indicated in Fig. 2.5 and c is the speed of light. As the delay magnitude increases, the SHG becomes weaker. Therefore, the auto-correlation trace can be mapped into a spatial distribution of the SHG, which can be detected by cameras. A typical single-shot autocorrelation trace is similar to that shown in Fig. 2.4 except that the horizontal scale is the spatial coordinate. The spatial width is related to the pulse width by a certain factor that can be easily calibrated by an oscilloscope.

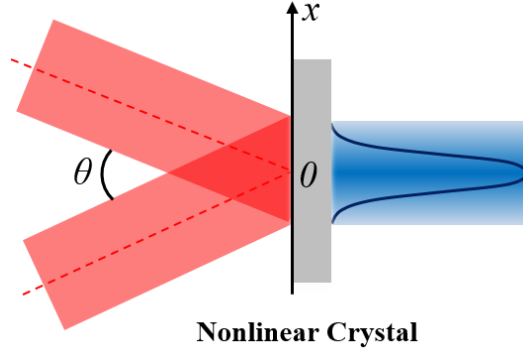


Figure 2.5. Illustration of single-shot autocorrelation.

Cross-correlation between two beams of different wavelengths is also used in this thesis, which is realized by sum frequency generation (SFG). Let ω_1 and ω_2 denote the frequencies of the two input waves, one of which needs characterizing, and ω_3 denotes the sum frequency. $v_{g,i}$ denotes the group velocity of the wave i in the nonlinear crystal, with $i = 1, 2$ or 3 . n_i denotes the refractive index of wave i . The ω_3 wave is assumed to be much weaker than the two input waves and perfect phase matching is assumed. The field is written as

$$E_i(z, t) = \text{Re}[a_i(z, t)e^{j(\omega_i t - k_i z)}], \quad (2.11)$$

where z and t are the spatial coordinate and the time, k is the wave vector, ω is the frequency and a is the amplitude. Then the propagation equation for the ω_3 wave inside the crystal is

$$\frac{\partial a_3(z, t_3')}{\partial z} = -j\kappa_3 a_1(t_3' - \eta_{13}z) a_2(t_3' - \eta_{23}z), \quad (2.12)$$

where

$$t_3' = t - z/v_{g,3}, \quad (2.13)$$

$$\eta_{ij} = 1/v_{g,i} - 1/v_{g,j}, \quad (2.14)$$

$$\kappa_i = \frac{\omega_i d_{eff}}{2n_i c}, \quad (2.15)$$

with d_{eff} be the effective nonlinear coefficient as introduced by Weiner (2009). (2.12) can be solved to yield

$$a_3(L, t_3') = -j\kappa_3 \int_0^L a_1(t_3' - \eta_{13}z) a_2(t_3' - \eta_{23}z) dz, \quad (2.16)$$

with L being the thickness of the crystal. If the ω_l wave has a short pulse width, approximated by a delta function

$$a_1(0, t) \propto \delta(t - \tau), \quad (2.17)$$

where τ is the delay between the two input beams, then by (2.16)

$$a_3(L, t_3') \propto sq\left(\frac{t_3' - \tau}{\eta_{13}L} - \frac{1}{2}\right) a_2\left(\frac{\eta_{12}(t_3' - \tau)}{\eta_{13}} + \tau\right), \quad (2.18)$$

where $sq(t) = 1$ when $|t| < 1/2$ and 0 otherwise. From (2.18), the average power of the SFG depends on the part of $a_2(t)$ from τ to $\tau + \eta_{12}L$. If the average power is recorded versus the delay, then the shape of $a_2(t)$ can be deduced with resolution equal to $|\eta_{12}L|$.

Figure 2.8 shows an example of cross-correlation trace by SFG. One input beam is centered at 800 nm with a pulse width of 69 fs. The other input beam is centered at 400 nm with unknown pulse width. Numerical calculation is performed following (2.16) by varying the assumed pulse width of the 400 nm beam. The result indicates that the 400 nm beam has a pulse width of 140 fs. In practice, one of the input beams is usually known, for example by auto-correlation, and the pulse width of the other beam is measured by cross-correlation.

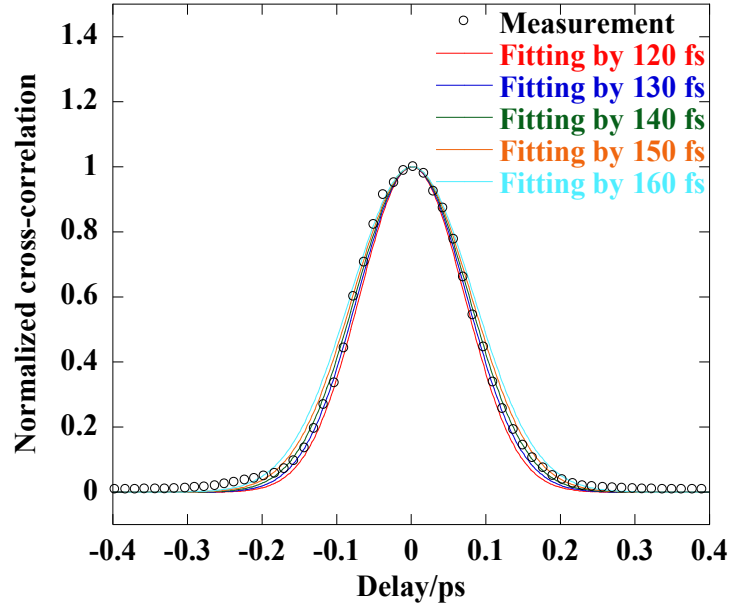


Figure 2.6. Cross-correlation trace of ultrafast laser pulses.

2.4 Summary

In this chapter, the experimental techniques used in this thesis are discussed including theories and optical arrangements. Ultrafast spectroscopy will be used to excite and detect the transient response of materials, which reflects the dynamics of energy carriers. By using a commercial optical parametric amplifier (OPA), the wavelength of the laser can be tuned to excite or detect the transient response of different energy levels. Autocorrelation and cross-correlation are used for measuring the pulse width. The scheme of ultrafast spectroscopy introduced in Section 2.1 is the basic configuration while the OPA or other devices can be included for specific design of experiments.

CHAPTER 3. ELECTRON-PHONON COUPLING ACROSS METAL-DIELECTRIC INTERFACE

Interface heat transfer is one of the major concerns in the design of micro- and nano-scale devices. For metal-dielectric composite structures, heat can cross the interface by interaction between phonons in the metal and the dielectric or by coupling between electrons in the metal and phonons in the dielectric. Phonon-phonon coupling has been simulated mainly by the acoustic mismatch model (AMM) and the diffuse mismatch model (DMM) as reviewed by Cahill, *et al.* (2003). As for electron-phonon coupling, there are different viewpoints. A study by Majumdar, *et al.* (2004) has assumed that electron-phonon coupling across a metal-dielectric interface is negligible. On the other hand, Bosco, *et al.* (2003) observed the dependence of the electron cooling rate on the substrate. Hopkins, *et al.* (2007 and 2009) revealed that energy could be transferred to the substrate by electron-interface scattering during ultrafast-laser heating.

In this chapter, we investigate heat transfer across metal-dielectric interface during and after heating by ultrafast laser. Interface resistances are defined for quantifying the strength of energy coupling across interface. By comparison between the simulation results based on the two-temperature model (TTM) and transient reflectance signals for gold films on silicon substrates, we find strong direct coupling between electrons in the metal film and phonons in the dielectric substrate during ultrafast-laser heating.

3.1 Transient reflectance Measurement on Gold Films Using 400 nm Pump and 800 nm Probe

Gold is chosen as the metal layer since gold has been extensively studied and its physical properties are well-known (Qiu, *et al.*, 1993, Wellershoff, *et al.*, 1999 and Chowdhury, *et al.*, 2003). Gold films of varying thicknesses on silicon are prepared by thermal evaporation. The thicknesses of the gold films are 39, 46, 60, 77 and 250 nm, measured by an atomic force microscope (AFM). The optical setup described in Section 2.1 is used for measuring the transient reflectance. The pump beam has a central wavelength of 400 nm and a full width at half maximum (FWHM) of 390 fs measured by cross-correlation and is focused onto the sample with a spot radius of 20.3 μm . The probe beam has a central wavelength of 800 nm and a FWHM of 205 fs measured by single-shot autocorrelation (SSA) and is focused with a spot radius of 16.9 μm . This pump pulse width is intentionally stretched from the original value of 140 fs to 390 fs for minimizing the influence from nonthermalized electrons. The thermalization time of electrons generally varies with the pump fluence and the pump wavelength (Fann, *et al.*, 1992) and can be on the order of 100 fs for gold (Sun, *et al.*, 1993). Therefore, if the pump laser has a duration comparable to or shorter than the thermalization time of electrons, the nonthermalized electron distribution can contribute to the transient reflectance signal, which will complicate the data explanation. Nonthermalized electrons in thermal transport have not been thoroughly studied, including the references cited above. The effect of nonthermalized electrons will be discussed in details in Chapter 4.

Figure 3.1 shows the transient reflectance signals for the sample of thickness 77 nm with different pump fluences before and after stretching the pump pulse. The plots

show the normalized relative reflectance change ($-\Delta R/R$) versus the delay time between the pump and the probe to highlight the contrast in cooling rates, indicating a decrease of reflectance for the 800 nm probe. As will be discussed thoroughly in Chapter 4, the interband transition threshold (ITT) for gold is 2.47 eV, which is the energy difference from the top of the d band to the Fermi energy E_F . As the electrons are heated, the smearing of the Fermi-Dirac distribution leads to increased electron occupancy above E_F and decreased electron occupancy below E_F , which reduces reflectance for photon energy smaller than the ITT. The probe photon energy used in this work is 1.55 eV, below the ITT, so the reflectance decreases at elevated electron temperature, T_e . As electrons are cooled down, the electron occupancy and the reflectance recovers to the initial value. Therefore, the transient reflectance signal can be related to the change of T_e .

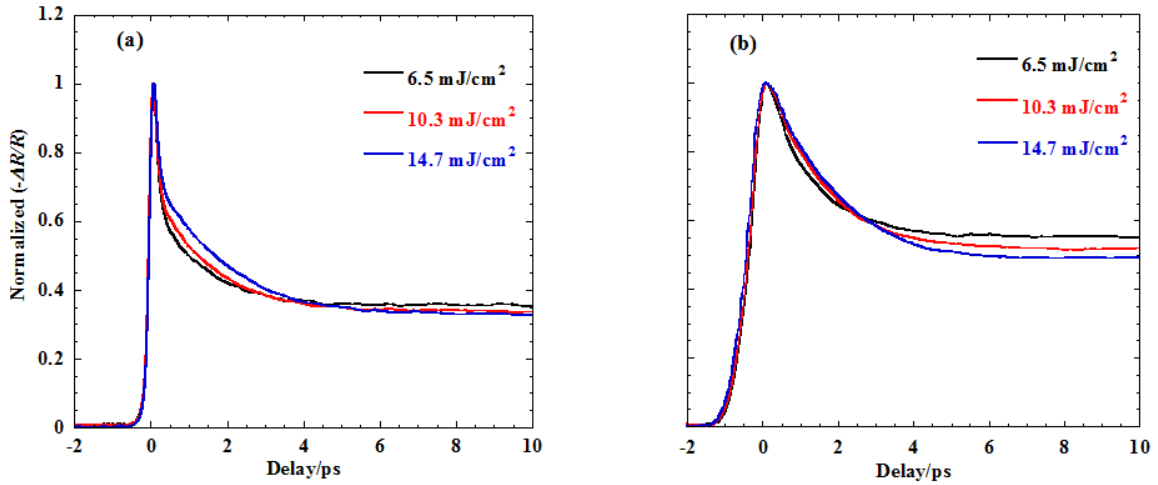


Figure 3.1. Transient reflectance signals for the 77 nm-thick gold film with different pump fluencies: (a) before stretching the pump pulse; (b) after stretching the pump pulse.

With a shorter pulse (Fig. 3.1(a)), a steep initial drop is seen in the signals, attributed to the contribution from nonthermalized electrons. Since the TTM to be used for simulation assumes a well-defined temperature for electrons or electrons have reached

thermal equilibrium, the model cannot predict the fast initial drop in the signals. As will be shown in Section 3.3, the signals obtained by stretched pulses, which suppress the contribution from nonthermalized electrons by slower heating, can be predicted better by the TTM.

Transient reflectance signals by stretched pump pulses with a fluence of 14.7 mJ/cm^2 are plotted in Fig. 3.2. The fast decay of the reflectance indicates energy transport from hot electrons to cold phonons, followed by a relatively slow decay after several ps, which indicates electrons and phonons have reached thermal equilibrium. The initial cooling rates are smaller for the samples with gold film thicknesses smaller than the electron ballistic length (about 100 nm for gold) since T_e is almost uniform across the thin films, and coupling with phonons within the gold film and the substrate are the cooling mechanisms. For the sample with 250 nm-thick gold layer, the initial decay is much faster partially due to thermal diffusion caused by a gradient of T_e in the gold film and partially due to the contribution from nonthermalized electrons as illustrated in Chapter 4.

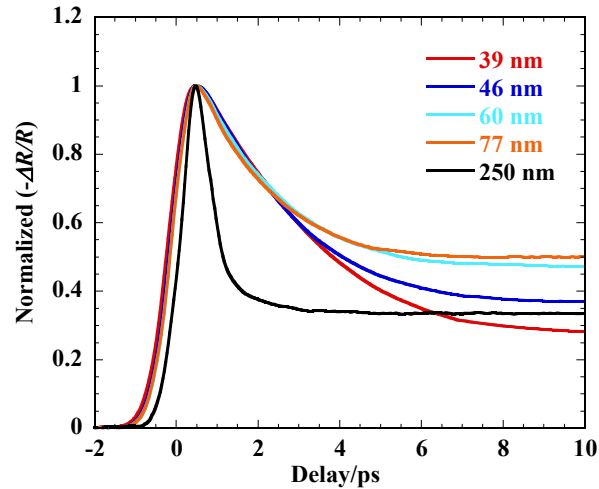


Figure 3.2. Transient reflectance measurement results for gold films of varying thicknesses on silicon.

3.2 Calculation of the Energy-Carrier Temperatures Using the TTM

Since both electrons and phonons are energy-carriers in metal while phonons are the main energy-carriers in dielectric, the heterogeneous interface between the gold film and the silicon substrate involves three temperature variables (two in the gold film and one in the substrate). The TTM introduced in Section 1.2 is applied to the metal while the one-temperature model is applied to the substrate. For investigating electron-phonon and phonon-phonon coupling across the interface, two interface thermal resistances are defined: R_{es} indicates the coupling strength between electrons in the gold film and phonons in the substrate, while R_{ps} indicates the coupling strength between phonons in the gold film and phonons in the substrate. Large resistance corresponds to weak coupling. The governing equations, the initial and the interface conditions are:

$$C_e \frac{\partial T_e}{\partial t} = k_e \frac{\partial^2 T_e}{\partial x^2} - G(T_e - T_p) + S, \quad (3.1a)$$

$$C_p \frac{\partial T_p}{\partial t} = k_p \frac{\partial^2 T_p}{\partial x^2} + G(T_e - T_p), \quad (3.1b)$$

$$C_s \frac{\partial T_s}{\partial t} = k_s \frac{\partial^2 T_s}{\partial x^2}; \quad (3.1c)$$

$$T_e(t=0) = T_p(t=0) = T_s(t=0) = 300 \text{ K}; \quad (3.2)$$

$$-k_e \frac{\partial T_e}{\partial x}(x=L) = \frac{T_e - T_s}{R_{es}}(x=L), \quad (3.3a)$$

$$-k_p \frac{\partial T_p}{\partial x}(x=L) = \frac{T_p - T_s}{R_{ps}}(x=L), \quad (3.3b)$$

$$-k_s \frac{\partial T_s}{\partial x}(x=L) = \frac{T_e - T_s}{R_{es}}(x=L) + \frac{T_p - T_s}{R_{ps}}(x=L). \quad (3.3c)$$

The subscripts e , p and s denote electrons in the gold film, phonons in the gold film, and phonons in the substrate, respectively. T represents the temperature, C the volumetric heat capacity, k the thermal conductivity, G the electron-phonon coupling factor governing the rate of energy transfer from electrons to phonons within the gold film, and L the thickness of the gold film. x and t are the spatial coordinate and the time respectively. At the front surface of the gold film, insulation boundary condition is used due to the much larger heat flux caused by laser heating relative to the heat loss to air. At the rear surface of the substrate, since the thickness of the substrate is thicker than 1 μm , there is no temperature rise within the time domain of consideration and thus insulation boundary condition is also applied.

Thermal properties of phonons in both gold and silicon are taken as temperature-independent due to the very weak temperature dependence. The thermal conductivity of phonons in metal is much smaller than that of electrons and is taken as 0.001 times the bulk thermal conductivity of gold. The volumetric heat capacity of phonons is taken as that of the bulk gold. C_e is taken as proportional to T_e (Kittel, 2005) with a proportion coefficient B_e :

$$C_e = B_e T_e. \quad (3.4)$$

k_e is calculated by the model proposed by Anisimov, *et al.* (1997):

$$k_e = \chi \frac{(\vartheta_e^2 + 0.16)^{1.25} (\vartheta_e^2 + 0.44) \vartheta_e}{(\vartheta_e^2 + \eta \vartheta_p) \sqrt{\vartheta_e^2 + 0.092}}, \quad (3.5)$$

which is valid for a wide range of T_e up to the Fermi temperature. In (3.5), $\vartheta_e = k_B T_e / E_F$ and $\vartheta_p = k_B T_p / E_F$, with k_B and E_F being the Boltzmann constant and the Fermi energy,

respectively. χ and η are constants. G is obtained with the model derived by Chen, *et al.* (2005):

$$G = G_{RT} \left[\frac{A_{ee}}{B_{ep}} (T_e + T_p) + 1 \right]. \quad (3.6)$$

Here G_{RT} is the value of G at the room temperature. A_{ee} and B_{ep} are constants derived from experimental data, as will be discussed later for evaluation of the electron collisional frequency. The laser heating source term S is calculated by

$$S = \frac{0.94(1 - R)J}{t_p(\delta + \delta_b)[1 - \exp(-\frac{L}{\delta + \delta_b})]} \exp\left[-\frac{x}{\delta + \delta_b} - 2.77\left(\frac{t}{t_p}\right)^2\right], \quad (3.7)$$

which assumes that the pump pulse has a Gaussian shape with a FWHM of t_p and that all the absorbed laser energy is deposited in the metal layer. J is the fluence of the pump pulse, R the surface reflectance for the pump, δ the optical penetration depth, and δ_b the electron ballistic length. x and t denote the spatial and the temporal coordinates, respectively. The properties and the parameters used in the simulation are listed in Table 3.1. R is calculated by the method of transfer matrix (Pedrotti, *et al.*, 2007) which considers the influence of multiple reflections at the interface. R_{es} and R_{ps} are varied during the simulation to study the effect of energy coupling across the interface. The governing equations (3.1a)-(3.1c) are solved to yield the evolution of the energy-carrier temperatures, T_e and T_p in the gold film and T_s in the silicon substrate.

Table 3.1. Properties and parameters used in the simulation by the TTM.

B_e	70 J/(m ³ K ²) (Chowdhury, <i>et al.</i> , 2003)	G_{RT}	4.6×10 ¹⁶ W/(m ³ K) (Hostetler, <i>et al.</i> , 1999)
C_p	2.49×10 ⁶ J/(m ³ K)	A_{ee}	1.2×10 ⁷ s ⁻¹ K ⁻² (Hopkins, 2010)
C_s	1.66×10 ⁶ J/(m ³ K)	B_{ep}	3.6×10 ¹¹ s ⁻¹ K ⁻¹ (discussed later)
χ	353.0 W/(mK) (Anisimov, <i>et al.</i> , 1997)	J	147 J/m ²
η	0.16 (Anisimov, <i>et al.</i> , 1997)	t_p	390 fs but with a modification due to the electron thermalization time (Hopkins, <i>et al.</i> , 2011)
E_F	5.53 eV (Chowdhury, <i>et al.</i> , 2003)	δ	16.28 nm
k_p	0.311 W/(mK)	δ_b	100 nm (Hohlfeld, <i>et al.</i> , 2000)
k_s	148 W/(mK)	L	39, 46, 60, 77 nm

The Drude model is used to relate T_e and T_p to the dielectric function and then the index of refraction, formulated as (Maier, 2007)

$$\varepsilon = \varepsilon_\infty - \frac{\omega_p^2}{\omega(\omega + i\omega_\tau)}, \quad (3.8)$$

where ω is the frequency of the probe laser and ω_p is the plasma frequency, 1.37×10¹⁶ rad/s for gold evaluated by the data in the book by Kittel (2005). ω_τ is the electron collisional frequency, the inverse of the electron relaxation time, which includes contribution from both T_e and T_p . The temperature dependence of electrical resistivity indicates that ω_τ is approximately proportional to T_p at high temperature (Kittel, 2005)

and from the Fermi liquid theory, its variation with T_e is quadratic (Ashcroft, *et al.*, 1976). Therefore, ω_τ is related to T_e and T_p approximately as

$$\omega_\tau = A_{ee}T_e^2 + B_{ep}T_p. \quad (3.9)$$

A_{ee} is taken as the literature value $1.2 \times 10^7 \text{ s}^{-1}\text{K}^{-2}$ (Hopkins, 2010) while ε_∞ and B_{ep} are evaluated to be 9.7 and $3.6 \times 10^{11} \text{ s}^{-1}\text{K}^{-1}$ by fitting the room-temperature value of the complex dielectric constant at 800 nm (Johnson, *et al.*, 1972). The complex index of refraction $n' + in''$ is the square root of the dielectric constant. Considering the gradient of the index of refraction caused by temperature gradient and the substrate effect, the reflectance for the probe is then calculated from n' and n'' by the method of transfer matrix.

We investigated the effect of R_{es} and R_{ps} on the transient reflectance signal by simulation. Two values of R_{ps} , $1 \times 10^{-10} \text{ m}^2\text{K/W}$ and $1 \times 10^{-7} \text{ m}^2\text{K/W}$, are used, each with a parameterized range of values for R_{es} . Figure 3.3 shows the calculated results for the sample with a 39 nm-thick gold film. Little difference can be seen between Fig. 3.3 (a) and (b) while different cooling rates are obtained with varying R_{es} in either plot, indicating that the cooling rate is not sensitive to the coupling strength between phonons in the gold film and the substrate. Note that an interface resistance of $1 \times 10^{-10} \text{ m}^2\text{K/W}$ is lower than any reported value, indicating a very high coupling strength. Conversely, the results vary significantly with the coupling strength between electrons in the gold film and phonons in the substrate. This is first because in the gold film the change of T_p is much smaller than the change of T_e so that the interface coupling between phonons in the gold film and the substrate does not influence the surface temperature, which mainly determines the measured reflectance. Also, the thermal conductivity of phonons in gold is

very small, making the surface isolated from the interface. However, the rise of T_e is much higher, and consequently, the cooling rate is sensitive to R_{es} . The relatively high sensitivity of the transient reflectance signal to R_{es} than to R_{ps} demonstrates that the former can be isolated for the study of the coupling between electrons in the gold film and phonons in the substrate. In the next section, this sensitivity difference is utilized to investigate the electron-phonon energy coupling across the interface.

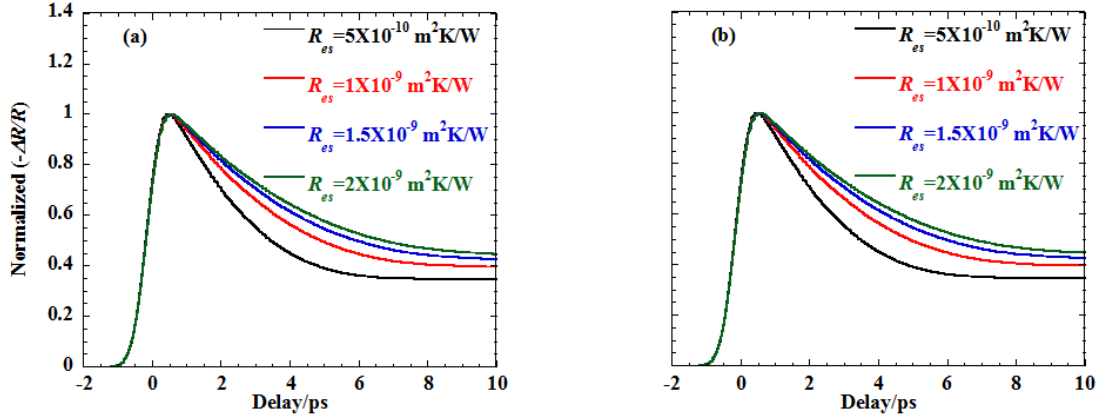


Figure 3.3. Simulation results with varying R_{es} for the sample with a 39 nm-thick gold film: (a) $R_{ps}=1 \times 10^{-10} \text{ m}^2\text{K/W}$; (b) $R_{ps}=1 \times 10^{-7} \text{ m}^2\text{K/W}$.

3.3 Energy Coupling Strength Across Metal-Dielectric Interface

The TTM, together with the Drude model, is used for fitting the measured transient reflectance signals, with R_{es} and R_{ps} adjusted for matching the measured cooling rates. The results are shown in Fig. 3.4. It is impossible to fit the measured results using insulation interface condition, no coupling or extremely large thermal resistance between electrons in the gold film and phonons in the substrate, which will significantly underestimate the cooling rates. For thin samples, we found that the value of R_{es} is of the order of 10^{-10} to $10^{-9} \text{ m}^2\text{K/W}$. This value is below the thermal resistance of representative solid-solid interface measured in thermal equilibrium, which are generally between 10^{-9}

$\text{m}^2\text{K/W}$ and $10^{-7} \text{ m}^2\text{K/W}$ (Cahill, *et al.*, 2003). This indicates that the direct coupling between electrons in the gold film and phonons in the substrate is strong. It is also noted that the resistance increases with the thickness of the gold film, indicating a decrease in the coupling strength between electrons and phonons across the interface. This could be due to the lower T_e obtained in thicker films, and consequently a decrease of the coupling strength. For the sample of thickness 250 nm, R_{es} has little effect on the simulation result since the interface is too far from the surface to influence the surface temperature, and therefore it is not presented here.

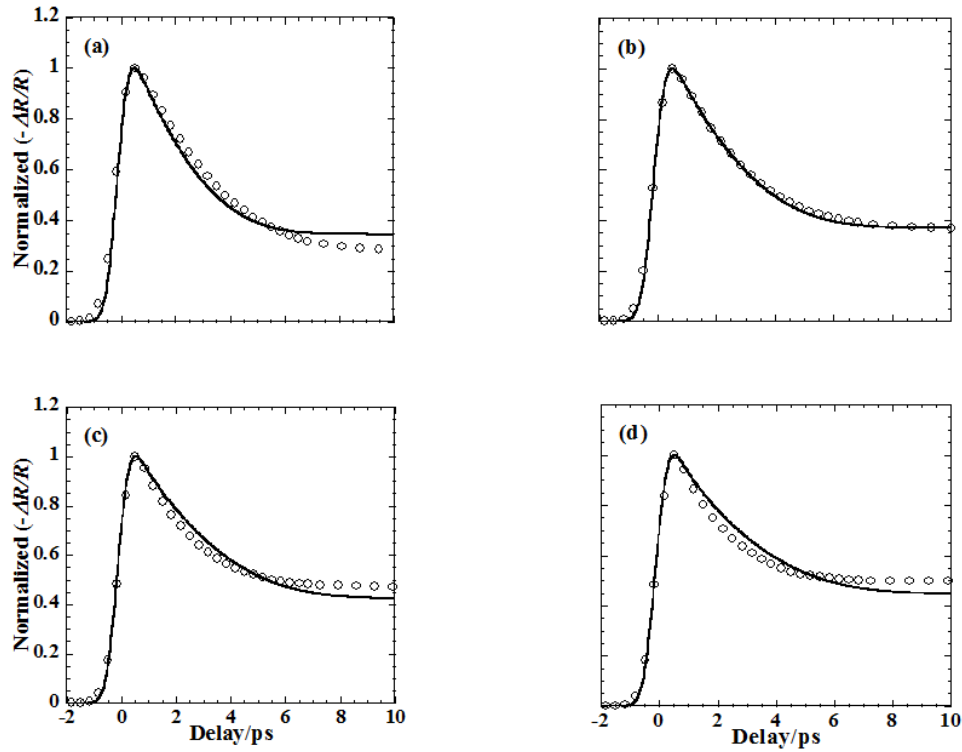


Figure 3.4. Comparison between the measurement and the simulation results for samples of varying gold thicknesses. The open circle represents the measured data and the solid line represents the simulation results. (a) 39 nm fitted by $R_{es}=5\times 10^{-10} \text{ m}^2\text{K/W}$; (b) 46 nm fitted by $R_{es}=6\times 10^{-10} \text{ m}^2\text{K/W}$; (c) 60 nm fitted by $R_{es}=1.2\times 10^{-9} \text{ m}^2\text{K/W}$; (d) 77 nm fitted by $R_{es}=1.8\times 10^{-9} \text{ m}^2\text{K/W}$.

The agreement between the calculated results and the measured data is generally good. The small discrepancy can result from the inaccuracy in computing the absorption or the temperature and the contribution from nonthermalized electrons to the measured signals. As shown in Fig. 3.1, small variation in the shape of the transient reflectance signals can result from different laser fluences and thus the maximum temperatures reached in the film. Absorption in metal, multiple reflections between the metal surface and the interface, and possible deviation of the properties of thin films from those of bulk can all contribute to uncertainties in the calculated temperatures, therefore affecting the calculated reflectance.

With the values of R_{es} shown in Fig. 3.4, the calculation shows that the highest T_e , at the surface of the 39 nm-thick gold film is about 6700 K. This highest T_e is much less than the Fermi temperature, 6.39×10^4 K for gold (Kittel, 2005), and thus it ensures the validity of the linear dependence of C_e on T_e . The highest T_p in the gold film is about 780 K, also in the 39 nm-thick gold film. As shown in Fig. 3.4, the measured R_{es} is of the order of 10^{-10} to 10^{-9} m²K/W. Even if R_{ps} , which is not determined in this study, is also that low (Actually 10^{-10} to 10^{-9} m²K/W is lower than any reported values.), the large difference between T_e and T_p in the gold film makes the interface heat transfer dominated by the coupling between electrons in the gold film and phonons in the substrate.

3.4 Summary

In summary, transient reflectance measurement by femtosecond laser pulses are performed on gold-silicon samples and the results are analyzed with the TTM and the Drude model. Using stretched femtosecond pulses is shown to be able to suppress the effect from nonthermalized electrons, and is thus more suitable for this study. It is shown

that due to the strong nonequilibrium between electrons and phonons during and after ultrafast-laser heating, it is possible to isolate the effect of the direct electron-phonon coupling across the interface, allowing investigation of its strength. The transient reflectance signals can be well-represented by the TTM. Comparison between the transient reflectance signals and the calculated results indicates that the direct coupling between electrons in the metal and phonons in the dielectric substrate dominates the interface heat transfer during and after ultrafast-laser heating of thin films. In the next chapter, the influence of nonthermalized electrons and the probe wavelength is explored in details, which helps to facilitate the modeling of transient heat transfer in metal.

CHAPTER 4. TRANSIENT DYNAMICS OF CARRIERS DETECTED BY ULTRAFAST SPECTROSCOPY WITH TUNABLE LASER WAVELENGTH

Carriers with different kinetic energies may have different transport properties such as effective mass and collisional rate with other carriers or phonons. Therefore, detecting dynamics of carriers on different energy levels can provide comprehensive information about carrier transportation. From the microscopic view, different light wavelengths or photon energies correspond to transition of carriers between different energy levels and therefore ultrafast spectroscopy with tunable laser wavelength can realize analysis of energy-dependent carrier behavior. In this chapter, transient reflectance measurement with varying laser wavelength is conducted for gold and gallium arsenide (GaAs), which are representatives of metals and semiconductors, to explore energy-dependent transport properties of carriers. The wavelength of the laser is adjusted by a commercial optical parametric amplifier (OPA) through nonlinear processes.

4.1 Dynamics of Photoexcited Carriers in Gold

In Chapter 3, the transient carrier dynamics of gold is briefly analyzed, based on which energy coupling across interface is investigated. But some problems remain unresolved such as worse matching between the calculated results and the transient reflectance signals for thick gold films. In this section, the transient carrier dynamics is analyzed in details by referring to the band structure of gold and probing with varying wavelength.

4.1.1 Band Structure of Gold and Experimental Configuration

The density of states (DOS) of gold is qualitatively shown in Fig. 4.1 (Hohlfeld, *et al.*, 2000). The electrons in the s/p band are considered free. The top of the d band, which overlaps with part of the s/p band in energy, lies 2.47 eV (502 nm) below the Fermi energy E_F . This energy difference is the interband transition threshold (ITT) for gold. When the excitation photon energy is lower than the ITT, only part of the free electrons are excited and the d band is not perturbed. On the other hand, when the excitation photon energy is larger than the ITT, the electrons in the d band can also absorb the energy and transit over E_F . In the latter case, it is difficult to model the transient energy process since the excitation energy is absorbed not only by the free electrons but also by the holes in the d band, the relaxation of which also contributes to the transient reflectance. In addition, the volumetric density of the free electrons and thus E_F will change as a function of the excitation fluence and properties of the free electrons such as thermal conductivity are modified accordingly. With this consideration, the 800 nm (1.55 eV) output from the Ti:Sapphire laser, which is below the ITT, is used as the pump in contrast to the previous work using 400 nm (3.1 eV) pump. Since the pump-induced perturbation ($\Delta R/R$) is small for photon energy far off the ITT, as shown in the next section, the absorption and the reflection of the sample to the pump are almost constant. Therefore the self-action of the pump discussed by Hohlfeld, *et al.* (2000) should be negligible. The wavelength of the probe is adjusted by the OPA to sense different energy levels. Gold film thicker than 1 μm is used to eliminate the influence of interface heat transfer in the concerned time domain so that the relaxation process is only determined by the dynamics of energy carriers inside the gold film.

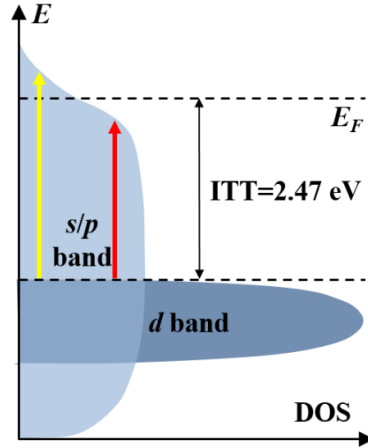


Figure 4.1. Qualitative illustration of the DOS of gold: the light and the dark blue regions indicate the s/p and the d bands, respectively, which overlap partially in energy; the red and the yellow arrows indicate transition from the d band to states below and above E_F .

4.1.2 Transient Reflectance Measurement on Gold Films Using 800 nm Pump with Varying Probe Wavelength

The transient reflectance signals using 800 nm pump with incident fluence of 5.28 mJ/cm² and varying probe wavelength are shown in Fig. 4.2 (a) with curves shifted vertically for clarity. The signals are characterized by a fast change (increase, decrease, or both) and a slower recovery. Probe with photon energy larger than the ITT detects $\Delta R > 0$ while probe with photon energy smaller than the ITT detects $\Delta R < 0$. This is due to change of the electron occupation induced by the excitation, which leads to change of the dielectric constant $\varepsilon = \varepsilon_1 + i\varepsilon_2$. The excitation increases the electron occupation above E_F and depletes the states below E_F . For probe with photon energy below the ITT (502 nm), transition from the d band to states below E_F is enhanced due to the reduced occupation as indicated by the red arrow in Fig. 4.1. In this case, the absorption of the probe photon increases ($\Delta\varepsilon_2 > 0$). On the other hand, for probe with photon energy above the ITT, transition from the d band to states above E_F is weakened as indicated by the yellow arrow

in Fig. 4.1 and therefore such probe detects decreased absorption ($\Delta\epsilon_2 < 0$). Based on the band structure of gold, $\Delta\epsilon_2$ can be computed after laser excitation, $\Delta\epsilon_1$ can then be calculated from the differential form of the Kramer-Kronig relation (2.2). ΔR is then calculated using $\Delta\epsilon_1$ and $\Delta\epsilon_2$ through (2.3) to (2.6). Our experimental data agree with the predicted dependence of ΔR on the probe wavelength as shown in Fig. 4.3 from the work by Sun, *et al.* (1994). The small deviation in the wavelength or the photon energy is due to the difference in the thickness since bulk gold is used in this work while the calculation is for a 20 nm-thick gold film. When the probe photon energy is close to the ITT, due to the finite bandwidth of the laser, the signal shows a hybrid feature.

Another observation from Fig. 4.2 (a) is the different amplitudes of the signals probed by varying wavelength. Note the pump fluence remains the same for all the wavelengths used. In Fig. 4.2 (b), the maximum (in terms of the absolute value) of the transient reflectance signal is plotted versus the probe photon energy. The photon energy above 2.6 eV is achieved by third harmonic generation (THG) from the OPA output. The signal is strong locally around 2.34 eV and 2.53 eV and weakens around the ITT and far off the ITT. This phenomenon can be understood by the temperature-dependent Fermi-Dirac distribution. When the electron temperature T_e rises, smearing of the Fermi-Dirac distribution occurs as shown qualitatively in Fig. 4.4 (a). The variation of the Fermi-Dirac distribution is small at E_F and has two peaks in the vicinity of E_F as illustrated in Fig. 4.4 (b). The states far from E_F are not perturbed after thermalization of electrons. Note: the variation of the Fermi-Dirac distribution is symmetric about E_F but ΔR is not because of the influence of the band structure or the DOS.

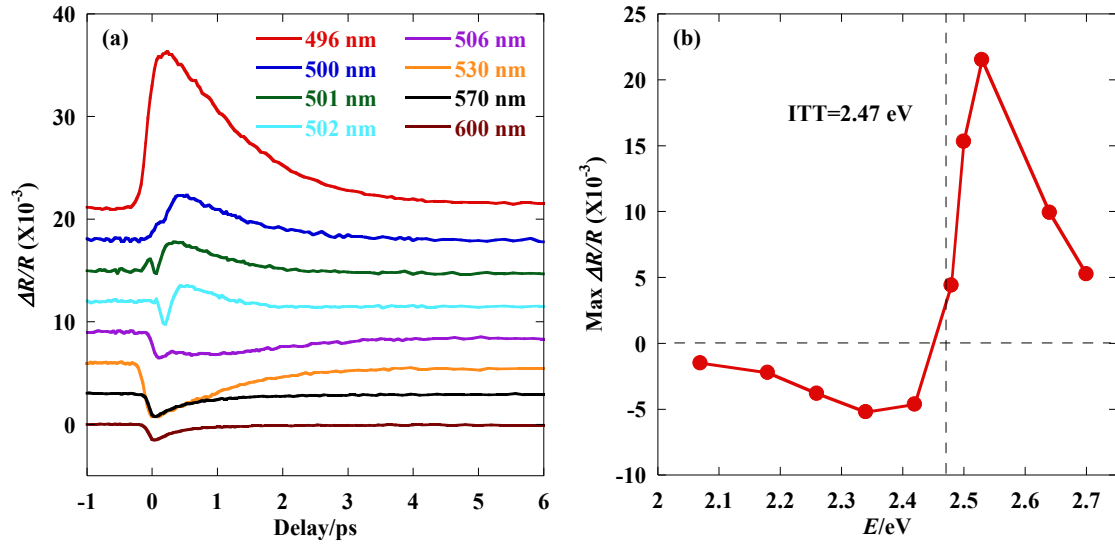


Figure 4.2. (a) Transient reflectance signals of gold by 800 nm pump and varying probe wavelength; (b) Dependence of the amplitude of the transient reflectance signal on the probe photon energy (The horizontal dashed line marks $\Delta R/R = 0$ and the vertical dashed line marks the energy equal to the ITT).

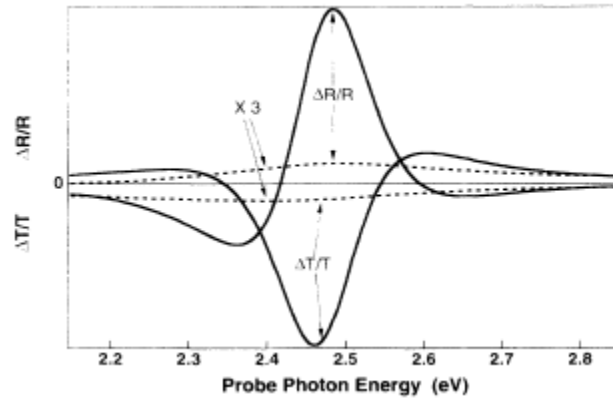


Figure 4.3. Calculated probe photon energy dependence of $\Delta R/R$ and $\Delta T/T$ for a 20 nm-thick gold film for the initial nonthermalized electron distribution (dashed lines) and the thermalized electron distribution (solid lines) from the work by Sun, *et al.* (1994).

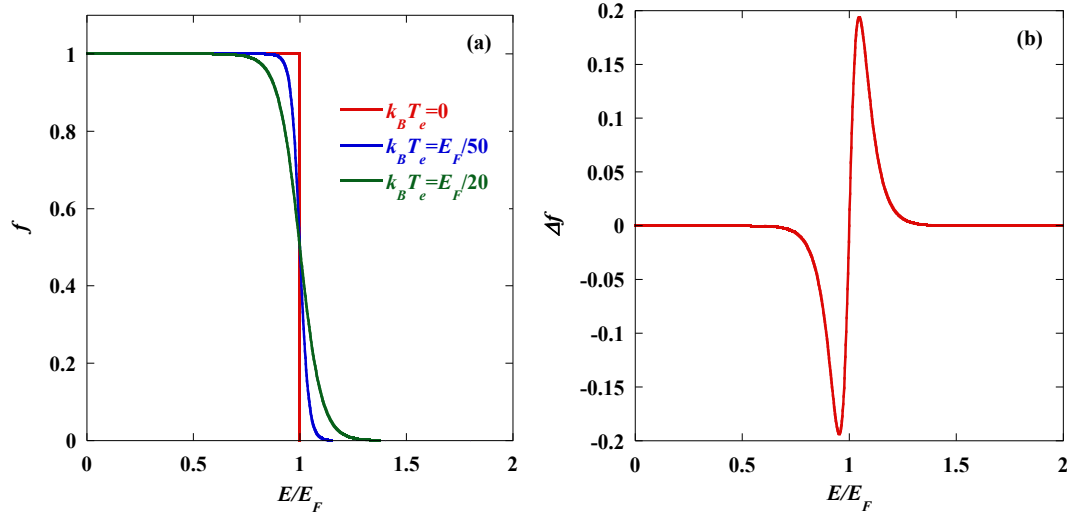


Figure 4.4. (a) The Fermi-Dirac distribution at varying temperature; (b) Difference in the Fermi-Dirac distribution between $T_e = E_F/50k_B$ and $T_e = E_F/20k_B$.

Due to the high sensitivity to ΔT_e , weak excitation can be used to achieve strong signal when probed around 490 nm (2.53 eV). This helps to keep the perturbation low enough to ensure the validity of the commonly used models for physical properties without sacrificing the signal-to-noise ratio. Also, with sufficiently low perturbation, ΔR is nearly proportional to ΔT_e . To justify this, measurements are conducted by varying the pump fluence (1.76 mJ/cm², 3.52 mJ/cm², 5.28 mJ/cm², and 7.04 mJ/cm²). ΔT_e is calculated using the two-temperature model (TTM) with details provided in Section 4.1.4. The maximum of ΔT_e plotted versus the pump fluence in Fig. 4.5 (a) and the maximum of the signal probed by 490 nm is plotted versus the maximum of ΔT_e in Fig. 4.5 (b) together with a linear fitting. It can be seen that good linearity is achieved within this fluence range. This simple relation between ΔR and ΔT_e facilitates the analysis by the TTM as shown in Section 4.1.4.

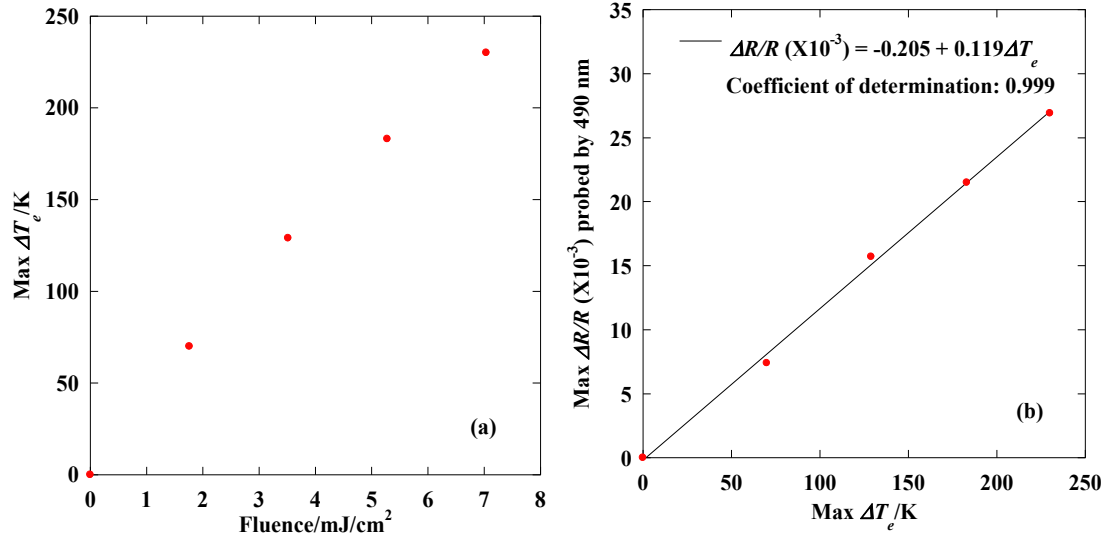


Figure 4.5. (a) Dependence of $\text{max } \Delta T_e$ on the pump fluence probed by 490 nm; (b) Dependence of amplitude of the transient reflectance signal on $\text{max } \Delta T_e$ probed by 490 nm with linear fitting indicated by the black line.

4.1.3 Influence of Nonthermalized Electrons

In previous works (Fann, *et al.*, 1992, Groeneveld, *et al.*, 1992, and Sun, *et al.*, 1994), it is shown that the thermalization process of photoexcited electrons can take hundreds of fs depending on the excitation wavelength and the excitation fluence. Prior to the thermalization process, the electron system does not follow the Fermi-Dirac distribution and thus has no defined temperature, which increases the difficulty of modeling. The instantaneous change of the electron distribution immediately after optical excitation can be calculated as (Sun, *et al.*, 1994):

$$\Delta f \propto f_0(E - E_p)[1 - f_0(E)] - f_0(E)[1 - f_0(E + E_p)], \quad (4.1)$$

where f_0 is the Fermi-Dirac distribution at the initial temperature before the excitation and E_p is the energy of the excitation photon. The coefficient of the proportionality is related to the fluence of the excitation. Physically, this means electrons within an energy span of

E_p are excited from states below E_F to states above E_F . In this work, the initial temperature is 298 K and the pump has photon energy of 1.55 eV. The comparison between the change of the electron distribution due to nonthermalized electrons based on (4.1) and due to fully thermalized electrons is illustrated in Fig. 4.6. T_e equal to 481 K is calculated using the TTM with pump fluence 5.28 mJ/cm^2 (see Section 4.1.4) to quantify the thermalized Fermi-Dirac distribution. The two distribution functions are normalized with respect to the peak of the thermalized Fermi-Dirac distribution and the proportionality coefficient in (4.1) is obtained by assuming the areas enclosed by the two curves are equal. The nonthermalized distribution evolves into the thermalized distribution mainly through interaction among hot electrons. When probed in the two sides of E_F , the contribution from thermalized electrons is much larger than that from nonthermalized electrons while the contribution from thermalized electrons is almost zero and the transient reflectance signal is dominated by nonthermalized electrons when probed far off E_F .

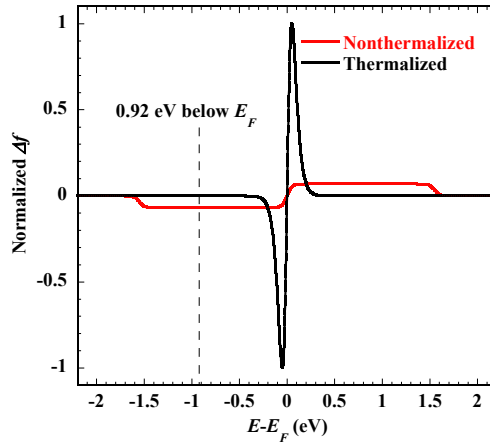


Figure 4.6. Comparison between the change of the electron distribution due to nonthermalized electrons based on (4.1) and due to thermalized electrons (The vertical dashed line indicates the states probed by 800 nm).

To illustrate the influence from nonthermalized electrons, transient reflectance is measured using 1300 nm pump and 800 nm probe on gold films of varying thickness. At 1300 nm, the pump excites only free electrons in the s/p band. Different wavelengths of the pump and the probe can help to reduce the noise from the scattered pump off the sample. The results are shown in Fig. 4.7. For samples thicker than 80 nm, the signals are featured by a fast decay within 1 ps. Such a fast relaxation process cannot be modeled by the TTM with a reasonable value of the electron-phonon coupling factor G , which assumes fully thermalized electrons. This nonthermalization process is accounted for by adding a time constant to the excitation pulse width in the TTM (Hopkins, *et al.*, 2011) but this method only improves the fitting to the rising edge of the transient reflectance. The fast decay is caused by the fast thermalization of electrons. With probe at 800 nm (1.55 eV), the contribution to the signal mainly comes from the perturbation to the states lying 0.92 eV below the ITT, 2.47 eV, as indicated by the vertical dashed in Fig. 4.6. After thermalization of electrons, which typically takes less than 1 ps, these states are hardly perturbed and thus the signal evolves within 1 ps into a period determined only by lattice heating. The relative contribution from nonthermalized electrons to the transient reflectance signal is larger for thicker films since heat diffusion and ballistic transport reduce the contribution from thermalized electrons, consistent with the observation by Sun, *et al.* (1994). This explains why good or at least close fitting can be achieved on gold films thinner than 80 nm in the previous work introduced in Chapter 3, in which the samples are probed at 800 nm. However, for the purpose of thermal modeling, it is more appropriate to use a probe wavelength so that nonthermalized electrons contribute little to

the signal, such as 490 nm for gold. As shown in Section 4.1.4, the transient reflectance signals can be well modeled using the TTM when probed at 490 nm.

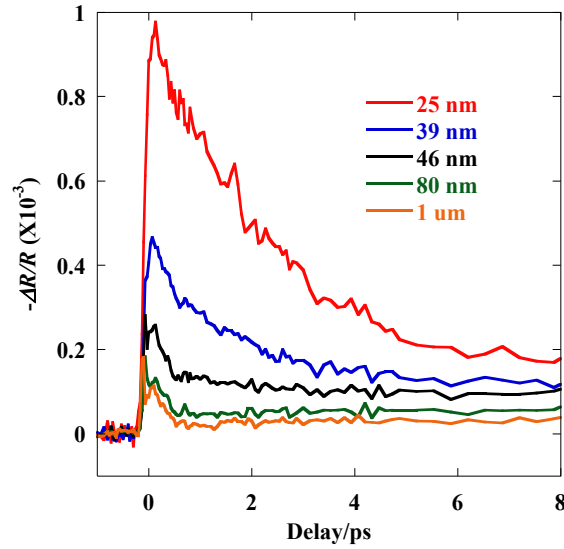


Figure 4.7. Transient reflectance signals of gold films of varying thickness excited by 1300 nm and probed by 800 nm.

4.1.4 Analysis of the Carrier-Phonon Coupling Rate

While Sun, *et al.* (1994) finds carrier relaxation time independent of the probe wavelength in the vicinity of the ITT, varying relaxation times are detected when probed with wavelength farther from the ITT. Figure 4.8 (a) shows the normalized transient reflectance signals using 800 nm pump with fluence 5.28 mJ/cm^2 and probed using photon energy below ITT. Within this range, ΔR is negative due to the increased empty states or holes below E_F created by the excitation. The decay rate of the signal indicates how fast these holes are filled with the cooling electrons or, in other words, how fast the holes relax. Gold has a face centered cubic crystal structure with one atom per primitive cell. Therefore, gold has 3 acoustic phonon branches and the carrier-phonon coupling is only through interaction with acoustic phonons, the characteristic time of which should

scales with $(E/k_B T)^{-1/2}$ (Lundstrom, 2000). Here E refers to the kinetic energy of electrons or holes, k_B is the Boltzmann constant and T is the temperature. Therefore carriers with higher energy should scatter with acoustic phonons at a faster rate, which makes physical sense since such carriers can emit phonons with a broader energy range. Since probe with longer wavelength detects dynamics of holes with higher energy, it detects faster decay. If probe with longer wavelength (>600 nm) is used, the effect from nonthermalized electrons begins to show up. In addition, states farther below E_F are probed with long wavelength. Perturbation to these states after thermalization of electrons is smaller and disappears earlier during cooling of electrons compared with states closer to E_F as shown in Fig. 4.4 (a). Thus probe with long wavelength sees smaller perturbation and shorter relaxation time. Therefore, the relaxation time detected as such underestimates the time required for electrons and phonons to reach thermal equilibrium. Figure 4.8 (b) shows normalized transient reflectance signals using 800 nm pump with fluence 5.28 mJ/cm^2 and probed using photon energy above ITT. Similarly, probe with photon energy farther from ITT detects faster relaxation. As discussed before, probe with 490 nm detects states most affected by thermal excitation and therefore the relaxation time detected by 490 nm can well reflect the time for electrons and phonons to reach thermal equilibrium.

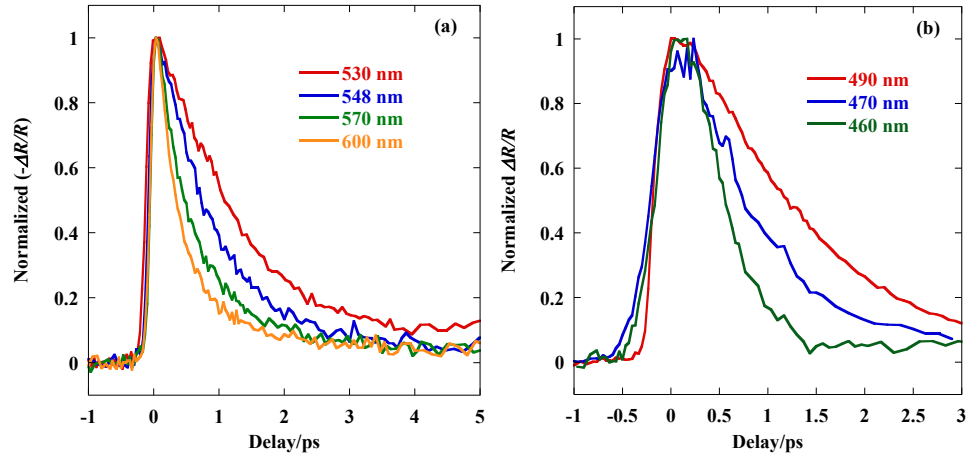


Figure 4.8. Dependence of the electron relaxation time on the probe wavelength: (a) probe photon energy below ITT; (b) probe photon energy above ITT.

To show the merit of using a proper probe wavelength, the TTM is applied to model the transient heat transfer process with G as a free variable. The width of the heating pulse including the thermalization time of electrons is taken as 280 fs to fit the rising edge of the transient reflectance. The ballistic depth of electrons is taken as 200 nm. The surface reflectance and the optical penetration depth for 800 nm are 0.97 and 12.44 nm, respectively. The other parameters are the same as those used in Chapter 3. The evolution of ΔT_e is compared with the normalized transient reflectance signal probed by 490 nm, as shown in Fig. 4.9 for 4 different pump fluences. For these 4 fluences, the maximums of T_e are 368 K, 427 K, 481 K, and 528 K, all of which are much lower than the Fermi temperature of gold (6.42×10^4 K) and within the range for assuming a linear relation between ΔR and ΔT_e . The calculated ΔT_e is almost proportional to ΔR except for the measured signal always has a flatter peak. This discrepancy should not be caused by the limited temporal resolution (on the order of 100 fs) in the measurement since the rising edge is captured well, which is the most steep part on the signal. It is perhaps

caused by contribution from intraband transition of the probe photon, which tends to reduce the reflectance. ΔT_e is normalized to 1.1 to compensate this deviation. In Fig. 4.9, except for the small deviation near the peak, the relaxation process is well matched up to 4 ps, after which the contribution from heating of the lattice is manifested. For all the fluences, the value of G is found to be 1.5×10^{16} W/(m³K). The ballistic depth may incur some uncertainty, whose value varies in literature from 105 nm (Hohlfeld, *et al.*, 2000) to 200 nm (Chowdhury, *et al.*, 2003). The value of G obtained by fitting should increase with increased value of the ballistic depth because large ballistic depth reduces the temperature gradient, weakens the diffusion effect in the calculation and stronger electron-phonon coupling is needed to maintain the same cooling rate. With this consideration, fitting is also performed using a ballistic depth of 100 nm and 150 nm. For 100 nm, $G = 1.3 \times 10^{16}$ W/(m³K) renders the best fitting while for 150 nm $G = 1.4 \times 10^{16}$ W/(m³K). Therefore, it is seen that the value of G does not vary significantly when the uncertainty of the ballistic depth is considered.

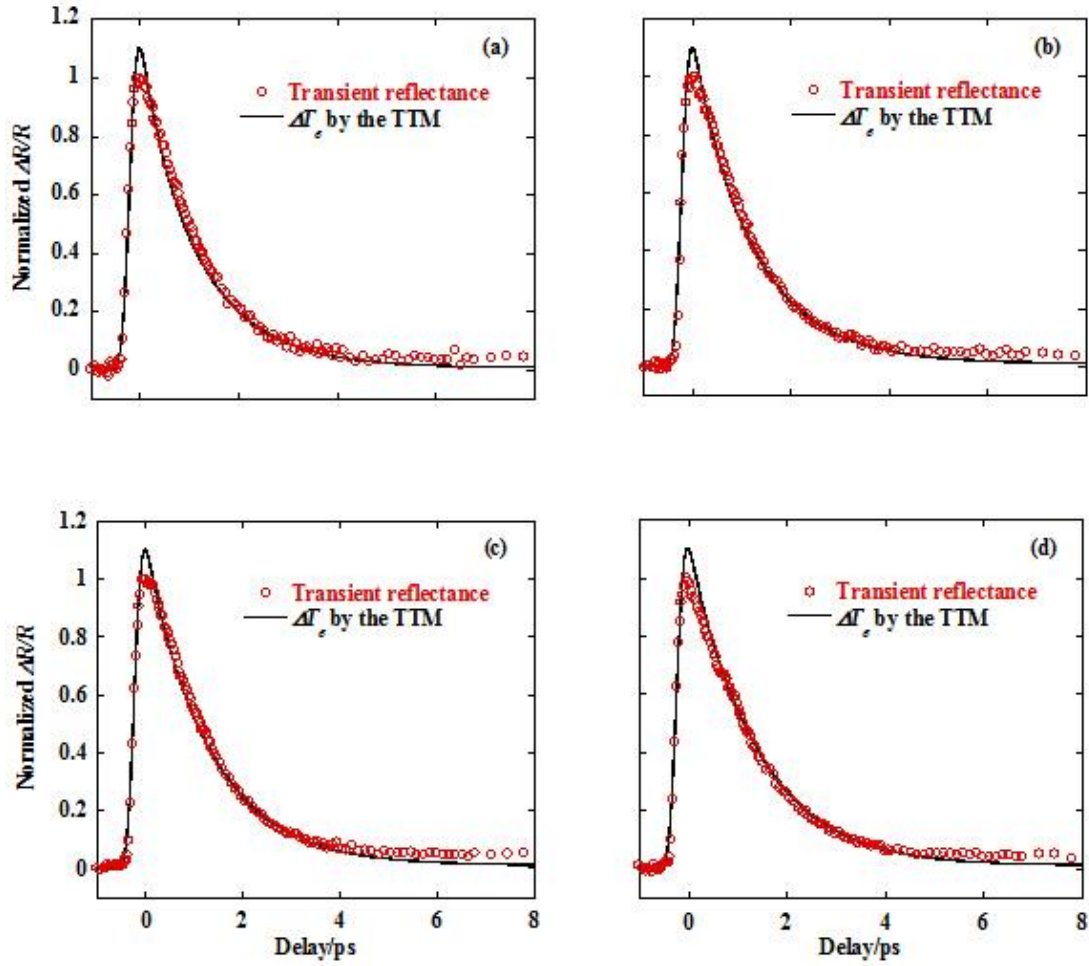


Figure 4.9. Comparison between the transient reflectance signals of bulk gold with the ΔT_e calculated by the TTM for pump fluence (a) 1.76 mJ/cm²; (b) 3.52 mJ/cm²; (c) 5.28 mJ/cm²; (d) 7.04 mJ/cm².

The analysis for gold can be extended to other materials for investigating carrier dynamics and simplifying the modeling effort, provided that the band structure is known. For instance, 577 nm (2.15 eV) may render the best sensitivity to electron excitation in transient reflectance measurement for copper since 2.15 eV is the transition threshold from the d band to E_F (Eesley, 1983 and Ehrenreich, *et al.*, 1962).

In summary, transient reflectance of gold is investigated using ultrafast spectroscopy with excitation of free electrons and varied probe wavelength. The

dependence of the signal on the probe wavelength is demonstrated and analyzed by referring to the band structure. It is shown that the signal is most sensitive to electron excitation when probed around 490 nm. Additionally, a simple linear relation between ΔR and ΔT_e with minimized impact from nonthermalized electrons is obtained around this wavelength. The TTM is applied to well fit the transient reflectance signal probed at 490 nm. This work serves as an instance of inspecting the dynamics of free electrons in metals. With detailed information of the band structure, the methodology can be used for analyzing transport properties of free electrons in other metals and n -type semiconductors, or free holes in p -type semiconductors.

4.2 Dynamics of Photoexcited Carriers in GaAs

In Section 4.1, the dynamics of free electrons in gold is explored through excitation with photon energy below the ITT, which does not perturb bound electrons. Such strategy is generally feasible for metals since metals usually have a large amount of free electrons leading to high values of E_F and the ITT, which makes it easy to achieve sub-ITT photon energies from common laser sources. For example, the values of the ITT for chromium, tungsten, and silver are 0.8 eV (Colavita, *et al.*, 1983), 0.85 eV (Colavita, *et al.*, 1983), and 4 eV (Ehrenreich, *et al.*, 1962) respectively besides 2.47 eV for gold and 2.15 eV for copper introduced in Section 4.1. With commercial laser sources, photon energy smaller than 0.8 eV can be accessed through nonlinear process. However, it is often much more difficult to exclusively excite free electrons or free holes for semiconductors. This is because the ITT for semiconductors, which is equal to the band gap, can be as small as 0 eV for graphene (Sarma, *et al.*, 2011), 0.05 eV for cobalt antimony (Singh, *et al.*, 1994), and 0.17 eV for bismuth telluride (Li, *et al.*, 1961). As

will be shown in this section, ultrafast spectroscopy can provide useful information about the carrier dynamics in semiconductors although when the excitation photon energy exceeds the band gap, electrons and holes are simultaneously excited and the relaxation processes of both contribute to the signal. GaAs is used for demonstration due to its well-known and simple band structure.

4.2.1 Transient Reflectance Measurement on GaAs with Excitation Across the Band Gap

In semiconductors with direct band gap, when a photon with energy $h\nu$ (h is the Planck constant and ν the frequency) larger than the band gap E_g is absorbed, an electron in the valence band can obtain this energy and transit to a high-energy state in the conduction band and a hole in the valence band is generated simultaneously, as shown in Fig. 4.10 (a). This excitation process follows the conservation laws of energy and momentum:

$$E_e + E_h + E_g = h\nu, \quad (4.2)$$

$$m_e E_e = m_h E_h, \quad (4.3)$$

where E_e and E_h donate the obtained kinetic energy of the electron and the hole and m_e and m_h donate the effective mass of the electron and the hole. From (4.2) and (4.3), the kinetic energy can be solved:

$$E_e = \frac{m_h}{m_e + m_h} (h\nu - E_g), \quad (4.4)$$

$$E_h = \frac{m_e}{m_e + m_h} (h\nu - E_g). \quad (4.5)$$

Therefore, immediately after the excitation, the average kinetic energy of the excited electrons is close to the value given by (4.4) while the average kinetic energy of the excited holes is close to the value given by (4.5). On the band structure diagram, E_e is the net energy relative to the conduction band edge while E_h is the net energy relative to the valence band edge, as illustrated in Fig. 4.10 (a). Usually, photoexcited carriers have higher temperatures than the cold lattice so electrons and holes will be cooled down by transferring energy to phonons or other carriers. During the cooling process, the average kinetic energy of carriers decreases. Equivalently, electrons shift towards the conduction band edge and holes shift towards the valence band edge as shown in Fig. 4.10 (b).

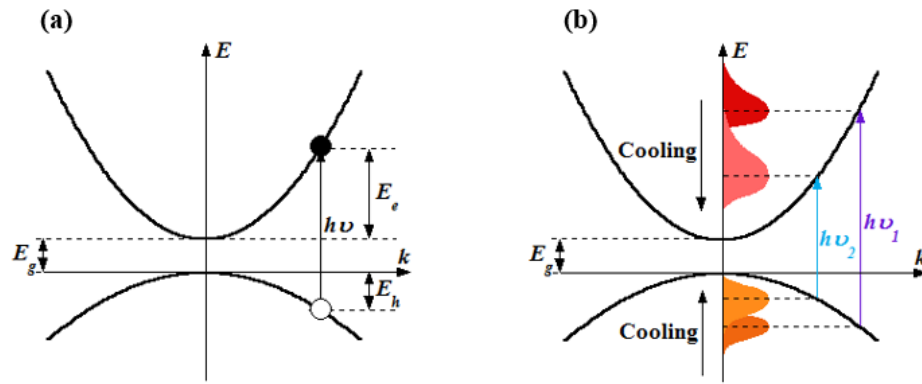


Figure 4.10. (a) Illustration of photoexcitation across the band gap; (b) Illustration of cooling of photoexcited carriers with the solid areas denoting the carrier distribution. The purple and the blue arrows indicate photon energies at which bandfilling occurs.

The relaxation of photoexcited carriers can be manifested in the transient reflectance signal by modifying the dielectric constant $\varepsilon = \varepsilon_1 + i\varepsilon_2$. Immediately after the excitation by the pump, excited carriers occupy high-energy levels, the difference of which is close to the pump photon energy $h\nu$. Thus light with photon energy around $h\nu$ will see absorption saturation due to the bandfilling. As these hot carriers cool down to the band edges, the bandfilling shifts towards photon energy equal to the band gap as

illustrated by the purple and the blue arrows in Fig. 4.10 (b). The bandfilling leads to absorption drop and thus a sink in ε_2 ($\Delta\varepsilon_2 < 0$) at the corresponding photon energy or wavelength. Therefore, as the carriers cool down, the sink in ε_2 shifts from the pump wavelength λ_{pump} towards the wavelength $\lambda_g = hc/E_g$ with c being the speed of light. This evolution is illustrated in Fig. 4.11. $\Delta\varepsilon_I$ is related to $\Delta\varepsilon_2$ through (2.2), from which the spectral dependence of $\Delta\varepsilon_I$ can be proved to follow the typical Lorentzian line shape qualitatively. On the blue side of the sink in ε_2 , $\Delta\varepsilon_I > 0$ while on the red side, $\Delta\varepsilon_I < 0$.

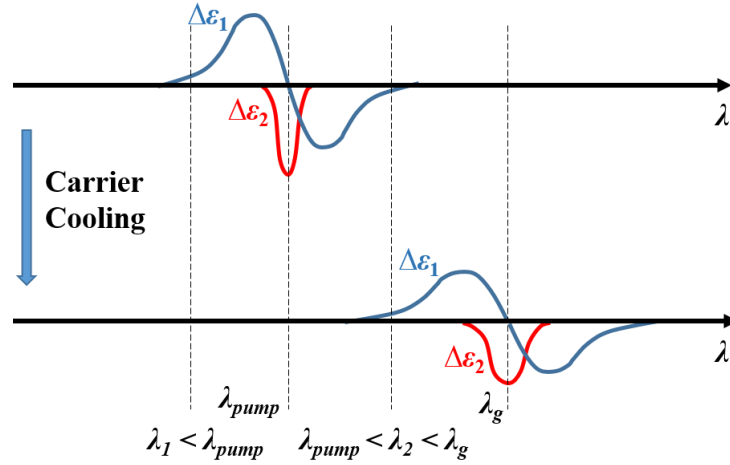


Figure 4.11. Evolution of $\varepsilon = \varepsilon_I + i\varepsilon_2$ after photoexcitation.

If the probe has wavelength shorter than λ_{pump} , exemplified by λ_I in Fig. 4.11, it will see initially $\Delta\varepsilon_I > 0$ followed a decay towards zero. If the probe has wavelength between λ_{pump} and λ_g , exemplified by λ_2 in Fig. 4.11, it will see initially $\Delta\varepsilon_I < 0$ followed by a rise across zero. Approximately $\Delta\varepsilon_2 < 0$ occurs only locally in the spectrum, then the reflectance change ΔR can be predicted by (2.5) with $\Delta\varepsilon_2 = 0$ for wavelength away from the local bandfilling:

$$\Delta R = \Delta\varepsilon_I \partial R / \partial \varepsilon_I. \quad (4.6)$$

To verify this analysis, transient reflectance measurement is conducted on the (100) surface of GaAs and the results are shown in Fig. 4.12. For GaAs, $\epsilon_1 = 13.55$, $\epsilon_2 = 0.63$ at 800 nm and $\epsilon_1 = 15.13$, $\epsilon_2 = 1.70$ at 610 nm. By (2.6a), $\partial R / \partial \epsilon_1 > 0$ at 800 nm and 610 nm and ΔR and $\Delta \epsilon_1$ follow the same sign. GaAs has a direct band gap equal to 1.43 eV (867 nm) at room temperature (Streetman, *et al.*, 2006). When 610 nm pump and 800 nm probe are used, the probe wavelength lies between λ_{pump} and λ_g so $\Delta R < 0$ is initially detected followed by a rise across zero as illustrated in Fig. 4.12 (a). When 800 nm pump and 610 nm probe are used, the probe wavelength is shorter than λ_{pump} so $\Delta R > 0$ is initially detected followed by a decay toward zero as illustrated in Fig. 4.12 (b). The transient reflectance signals agree with the prediction by the Kramers-Kronig relations. This analysis is qualitatively correct since the bandfilling usually dominates the change of refractive index (Bennett, *et al.*, 1990) for photon energy above the band gap but other physical processes such as lattice heating and carrier screening may also affect the optical observables, which requires sophisticated calculation for accurate quantification.

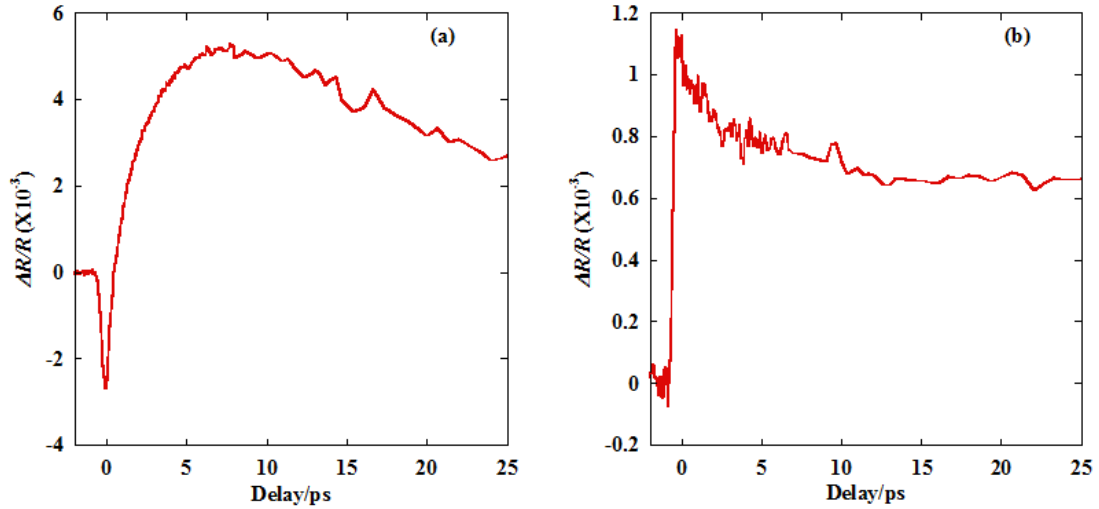


Figure 4.12. Transient reflectance measurement results on GaAs by (a) 610 nm pump and 800 nm probe and (b) 800 nm pump and 610 nm probe.

With sufficient information about the band structure, the analysis based on the Kramers-Kronig relations can provide an estimation of the energy relaxation rate of carriers. The work by Shank, *et al.* (1978) demonstrates such estimation by measuring transient reflectance of GaAs with 307.5 nm (4.03 eV) pump and 615 nm (2.02 eV) probe. ΔR at 615 nm is calculated from the band structure and the Kramers-Kronig relations as a function of the carrier temperature, which is illustrated in Fig. 4.13. The sum of the mean electron energy $\langle E_c \rangle$ and the mean hole energy $\langle E_v \rangle$ is also calculated versus the carrier temperature, which is equal to 2.6 eV (4.03 eV-1.43 eV) immediately after the excitation. From the calculated results, $\Delta R = 0$ when $\langle E_c \rangle + \langle E_v \rangle = 1$ eV as marked by the red dashed lines. Therefore, when the transient reflectance signal crosses zero, the electron and the hole lose 1.6 eV on average to other carriers and phonons. Since the zero-crossing time can be read from experiment, the energy relaxation rate can then be

estimated. The limitation of this methodology is its failure to distinguish the electron dynamics and the hole dynamics.

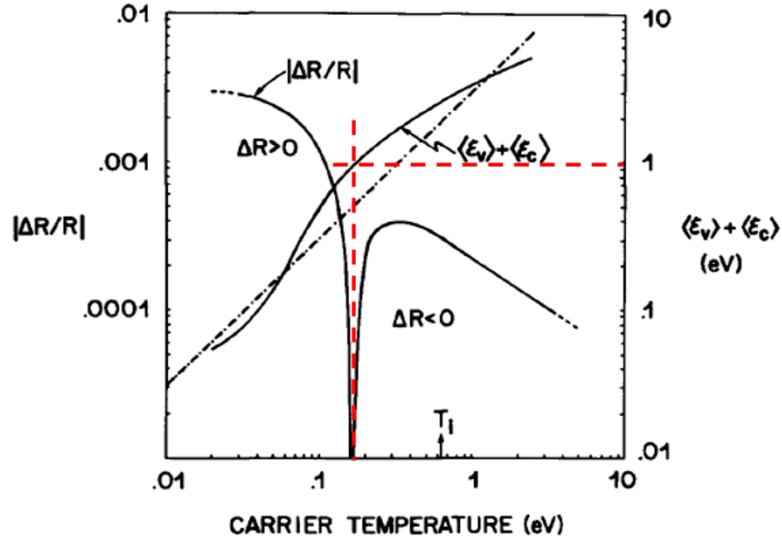


Figure 4.13. Calculated $\Delta R/R$ versus the carrier temperature T for 307.5 nm pump and 615 nm probe. The volumetric densities of photoexcited electrons and holes are both 10^{19} cm^{-3} . The sum of the mean electron energy $\langle E_c \rangle$ and the mean hole energy $\langle E_v \rangle$ is also plotted versus T . The black dot-dash line shows the classical value of $\langle E_c \rangle + \langle E_v \rangle$, $3k_B T$. T_i indicates the carrier temperature immediately after the excitation and the red dashed lines mark the values of T and $\langle E_c \rangle + \langle E_v \rangle$, at which $\Delta R = 0$. The plot is from the work by Shank, *et al.* (1978).

4.2.2 Transient Reflectance Measurement on GaAs with Free Carrier Excitation

In Section 4.1 the dynamics of free carriers in gold is inspected by sub-ITT excitation while in Section 4.2.1 the dynamics of electrons and holes in GaAs is inspected by excitation across the ITT, the band gap. Actually, the dynamics of carriers in metals and semiconductors are not exclusively different. Instead, analog exists between metals and semiconductors with respect to the carrier dynamics. For instance, if the pump photon energy exceeds the ITT of gold, bound electrons in the d band can be excited over E_F , leaving holes in the d band and then the transient change of the optical properties will

result from relaxation of both electrons and holes. If the pump photon energy is below the band gap of semiconductors, then transition across the band gap cannot happen if multiphoton absorption is negligible, the possibility of which is usually small for moderate excitation intensity. In this case, no carriers will be excited at 0 K since the valence band is completely filled while the conduction band is totally empty. At elevated temperature, some electrons can be thermally excited into the conduction band and holes are generated simultaneously in the valence band. These thermoexcited carriers can absorb the photon energy but such absorption is usually weak because the amount of thermoexcited carriers is small. However, in doped semiconductors, there is a considerable number of free carriers, which can be photoexcited to modify the optical properties. The analysis for the dynamics of free electrons in metals can be applied for the dynamics of free electrons in *n*-type semiconductors or holes in *p*-type semiconductors.

In order to illustrate the dynamics of free carriers in semiconductors, transient reflectance measurement is conducted on the (100) surface of an *n*-doped GaAs sample with doped carrier concentration $1.82\text{-}3.37 \times 10^{18} \text{ cm}^{-3}$ and thickness 0.35 mm. The pump is at 1400 nm corresponding to 0.89 eV smaller than the band gap of GaAs 1.43 eV and therefore only free electrons in the conduction band are excited. The pump fluence is 4.48 mJ/cm^2 . According to the reflectance data by Philipp, *et al.* (1963) and the absorption coefficient data by Spitzer, *et al.* (1959), the density of the excited free carriers is $3.05 \times 10^{17} \text{ cm}^{-3}$ estimated as by taking the reflectance as 0.3 and the absorption coefficient as 10 cm^{-1} and assuming that the laser energy is uniformly deposited within the sample thickness. The probe wavelength is selected with detailed consideration of the

band structure as shown in Fig. 4.14. The conduction band minimum and the valence band maximum are at the same wave vector $k = 0$ or the Γ point, separated by the band gap 1.43 eV. The heavy hole band and the light hole band are degenerate at the Γ point. The maximum of the split-off band lies 0.34 eV below the Γ point. To simplify the physical picture, the probe wavelength is selected near 800 nm, corresponding to 1.55 eV. For this wavelength, only states near the band extremes are probed. The split-off band, the L -valley and the X -valley are not probed, accesses to which require photon energies of 1.76 eV, 1.71 eV and 1.90 eV, respectively, as shown in Fig. 4.14.

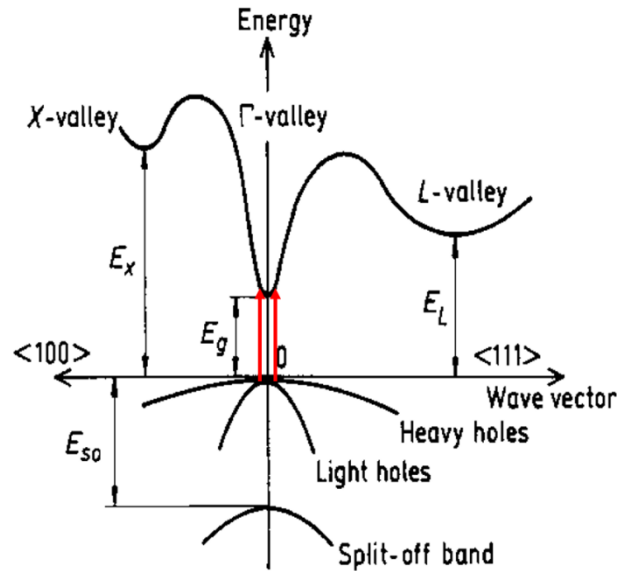


Figure 4.14. Band structure of GaAs (<http://www.ioffe.ru/SVA/NSM/Semicond/GaAs/bandstr.html>). The red and the orange arrows indicate transitions by optical excitation.

The transient reflectance signals are shown in Fig. 4.15 with vertical shift for clarity. The trends of the signals can be explained by referring to the analysis for the transient reflectance signals of gold in Section 4.1.2. The valence band of GaAs is not perturbed in analogy with the d band of gold. The perturbation occurs only in the

conduction band of GaAs in analogy with the s/p band of gold. The excitation increases the mean energy of free electrons in the conduction band leading to less occupied low energy states such as state 1 in Fig 4.16 (a) and more occupied high energy states such as state 3 in Fig. 4.16 (a). Some intermediate energy states such as state 2 in Fig. 4.16 (a) have smaller change in occupation in analogy with the Fermi energy E_F of gold. Transition from the d band to the perturbed states in the s/p band dominates the contribution to the change of the optical properties of gold and similarly, transition from the valence band to the perturbed states in the conduction band determines the transient reflectance signals of GaAs. From Fig. 4.15, probe with long wavelength, which senses the depleted low energy states, detects $\Delta R < 0$. As the probe wavelength decreases, less depleted or more occupied energy states are detected and the negative component drops in magnitude. In our wavelength range, $\Delta R < 0$ with large magnitude is detected by 830 nm probe while a hybrid feature with much smaller magnitude is detected by 760 nm probe. The trends of the signals within short delay are similar to those of gold for sub-ITT probe wavelengths as shown in Fig. 4.2 (a).

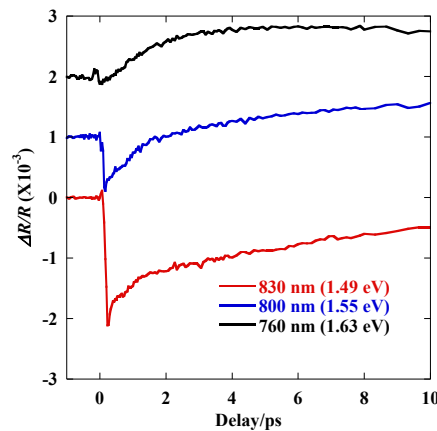


Figure 4.15. Transient reflectance signals of n -type GaAs by 1400 nm pump with fluence 4.48 mJ/cm^2 and varying probe wavelength.

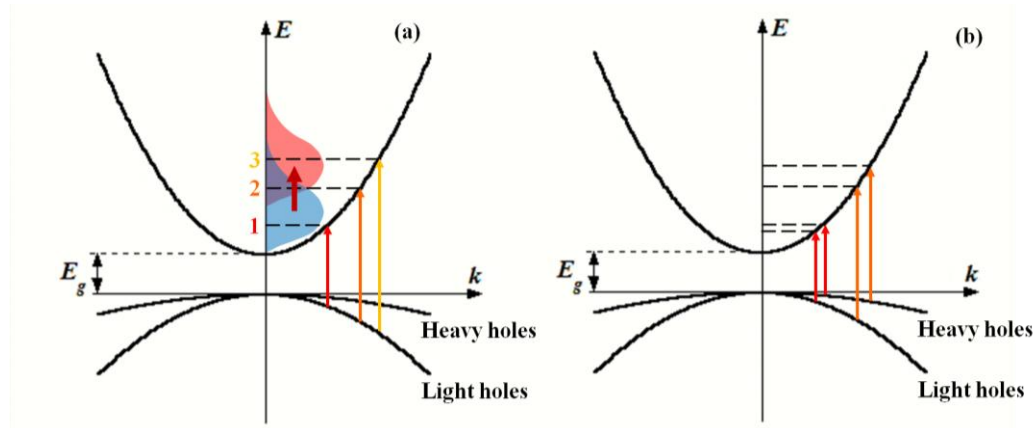


Figure 4.16. Transition analysis for GaAs: (a) energy states probed by varying probe wavelength (The blue area indicates the cold electron distribution while the red area indicates the hot electron distribution; The thick arrow indicates the excitation by the pump while the thin arrows indicate transitions by the probe.); (b) effect of two possible transitions for one probe wavelength (The thin arrows indicate transitions by the probe.).

One difference between the case of gold and the case of GaAs is that the probe can detect two energy states in the conduction band due to the presence of the heavy hole and the light hole bands. As shown in Fig. 4.16 (b), for one probe wavelength, the transition can be from the light hole band to some low energy states in the conduction band or from the heavy hole band to some high energy states in the conduction band. The disparity between the two possible transitions is larger for probe with short wavelength (the orange arrows in Fig. 4.16 (b)) compared to probe with long wavelength, which accesses states closer to the band gap (the red arrows in Fig. 4.16 (b)). Therefore, probe with short wavelength may detect more complex signals since the relaxation of electrons in more diverse energy states to the transient reflectance. From Fig. 4.15, the signal probed by 830 nm shows a simple exponential rise compared with the more complex feature detected by 760 nm. Thus probing closer to the band gap facilitates the analysis.

To sum up, transient reflectance of GaAs is investigated by excitation across the band gap and excitation below the band gap. In both cases, the transient reflectance can reflect the dynamics of carriers with analysis based on the band structure and the Kramers-Kronig relations. This work serves as an instance of inspecting the dynamics of carriers in semiconductors. Analog between metals and conductors can facilitate investigation of complex materials by referring to materials with well-known properties.

4.3 Summary

In summary, the carrier dynamics of metals and semiconductors is analyzed through transient reflectance measurement with gold and GaAs serving as the representative materials due to their well-known properties. Generally speaking, the carrier dynamics of different materials, mainly determined by the band structure and the electron occupation, is rather diverse and so is the effect on optical observables. *Ab initio* calculation and the Kramers-Kronig relations can help to evaluate the transport properties of carriers based on the information from time-resolved ultrafast spectroscopy. Appropriate selection of the laser wavelength in ultrafast spectroscopy can clarify the physical processes and facilitate the analysis.

CHAPTER 5. DYNAMICS OF ENERGY CARRIERS IN SKUTTERUDITES DETECTED BY ULTRAFAST SPECTROSCOPY

Skutterudites doped with proper elements and concentrations have attracted much attention as a high temperature thermoelectric material due to their high figure of merit (ZT) in the temperature range from about 600 to 850 K (Nolas, *et al.*, 1999; Kleinke, 2010; Liu, *et al.*, 2012). Research on skutterudites mainly aims to optimizing its thermoelectric performance such as exploring the microscopic mechanism of property manipulation and test of the influence of different chemical compositions. In this chapter, ultrafast spectroscopy is utilized to inspect the transient dynamics of energy carriers in skutterudites. Information obtained for GaAs shown in Chapter 4 is referred to for analyzing the carrier dynamics of skutterudites, which has a complex band structure. This study provides information about the transport properties of energy carriers, which is closely related to the thermal and the electrical conductivity.

5.1 Interaction Between Guest Atoms and the Host Lattice in Filled Skutterudites

5.1.1 Background

Binary skutterudites have the general chemical formula MX_3 with M being a transition metal atom such as Co, Rh or Ir and X being a pnictide atom, usually P, As or Sb. The skutterudite crystal belongs to the space group $Im\bar{3}$ and has the body-centered cubic (bcc) structure as shown in Fig. 5.1. The unit cell consists of eight cubes with the M

atoms on the corners. Six of the eight cubes are filled with mutually perpendicular X_4 rings while the other two cubes are left empty with large voids. The two voids can be filled by other atoms such as alkaline-earth atoms.

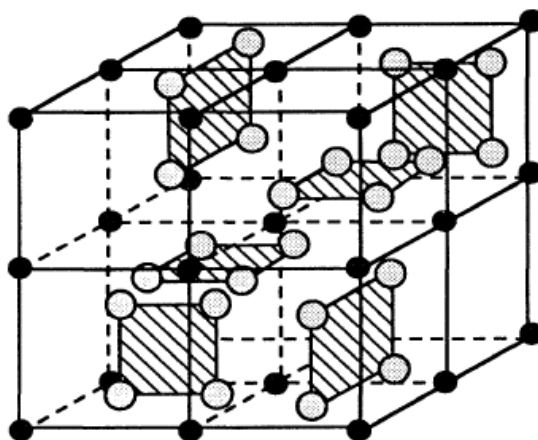


Figure 5.1. Unit cell of the binary skutterudite crystal structure (Morelli, *et al.*, 1995). The gray circle represents the pnictide atom and the black circle represents the transition metal atom.

As proposed by Slack (1995), the filling atoms can “rattle” inside the cage-like voids and such rattling motion can scatter phonons leading to reduced lattice contribution to the thermal conductivity. It has been confirmed that filling the voids with guest atoms can significantly reduce the lattice thermal conductivity k_L and improve the thermoelectric figure of merit (Meisner, *et al.*, 1998, Nolas, *et al.*, 2000, and Shi, *et al.*, 2011). Also, it has been found that filling the voids with multiple species could suppress k_L more effectively (Shi, *et al.*, 2008 and 2011) which is usually explained by a wider spectrum of phonons scattered by atoms with different rattling frequencies. However, there are different viewpoints about the underlying mechanism. The concept of localized rattlers to describe the role of guest atoms is supported by a number of studies including Raman spectroscopy (Li, *et al.*, 2001), inelastic neutron scattering together with heat

capacity measurements (Keppens, *et al.*, 1998 and Hermann, *et al.*, 2003), and infrared reflectance spectroscopy (Dordevic, *et al.*, 1999). On the other hand, molecular dynamics (MD) simulations showed that anharmonic interaction between host and guest atoms was important for decreasing k_L (Bernstein, *et al.*, 2010). Another MD studies explained the lower k_L as a result of lattice distortion and weaker interatomic interaction among host atoms due to filling atoms (Huang, *et al.*, 2010). Using neutron spectroscopy and *ab initio* calculations, it was found that well-defined phase relations between guest and host atom dynamics existed (Koza, *et al.*, 2008), which also contradicted the concept of independent rattlers. Therefore, there is still a controversy on the mechanism of k_L reduction in filled skutterudites.

5.1.2 Transient Reflectance Measurement on Filled Skutterudites Using 400 nm Pump and 800 nm Probe

Ultrafast spectroscopy was previously carried out successfully to study the interaction between the host lattice and the guest atoms in skutterudites filled with misch-metal atoms (Wang, *et al.*, 2009). In this section, we investigate the interaction between filling atoms and phonons in single- and multiple-filled skutterudites. This study allows determination of the effect of filling skutterudites with multiple elements on k_L .

Three single-filled skutterudite samples with individual element and a triple-filled sample with all the three elements are used to test the effect of multiple-element filling. Using electron probe microanalysis, the compositions of these samples are determined as $\text{Ba}_{0.26}\text{Co}_4\text{Sb}_{12.01}$, $\text{Yb}_{0.21}\text{Co}_4\text{Sb}_{11.92}$, $\text{La}_{0.14}\text{Co}_4\text{Sb}_{11.99}$ and $\text{Yb}_{0.05}\text{La}_{0.05}\text{Ba}_{0.08}\text{Co}_4\text{Sb}_{11.92}$. These samples were made and characterized in Chemical and Materials Systems Laboratory, GM Global R&D. Ultrafast spectroscopy for measuring the interaction between the host

lattice and guest atoms is based on the setup described in Section 2.1. The 800 nm probe and the 400 nm pump have pulse durations (FWHM-full width at half maximum) of 70 fs and 140 fs, respectively.

The transient reflectance signals of all the samples have similar features and Fig. 5.2 shows the normalized signals, where the insets illustrate the oscillation in a magnified scale. Compared with the transient reflectance signals of the previously studied misch-metal-filled skutterudites as shown in Fig. 5.3 (Wang, *et al.*, 2009), the oscillation is much weaker. There are two possible reasons for this distinction. The first is the much lower filler concentrations used in these samples ($\sim 10\text{-}20\%$) compared with previously investigated misch-metal filled samples ($55\text{-}82\%$). The second is the different electronic band structures and the different electron occupation caused by the differences in compositions such as doping level and Co-substitution. Modulation of the optical signal by lattice vibration is generally most prominent when the probe is at the spectrum range where the slope of the absorption spectrum is large (Sagar, *et al.*, 2008). The difference in the band structure will change the absorption or reflection spectrum, which changes the sensitivity of the probed state to lattice vibration.

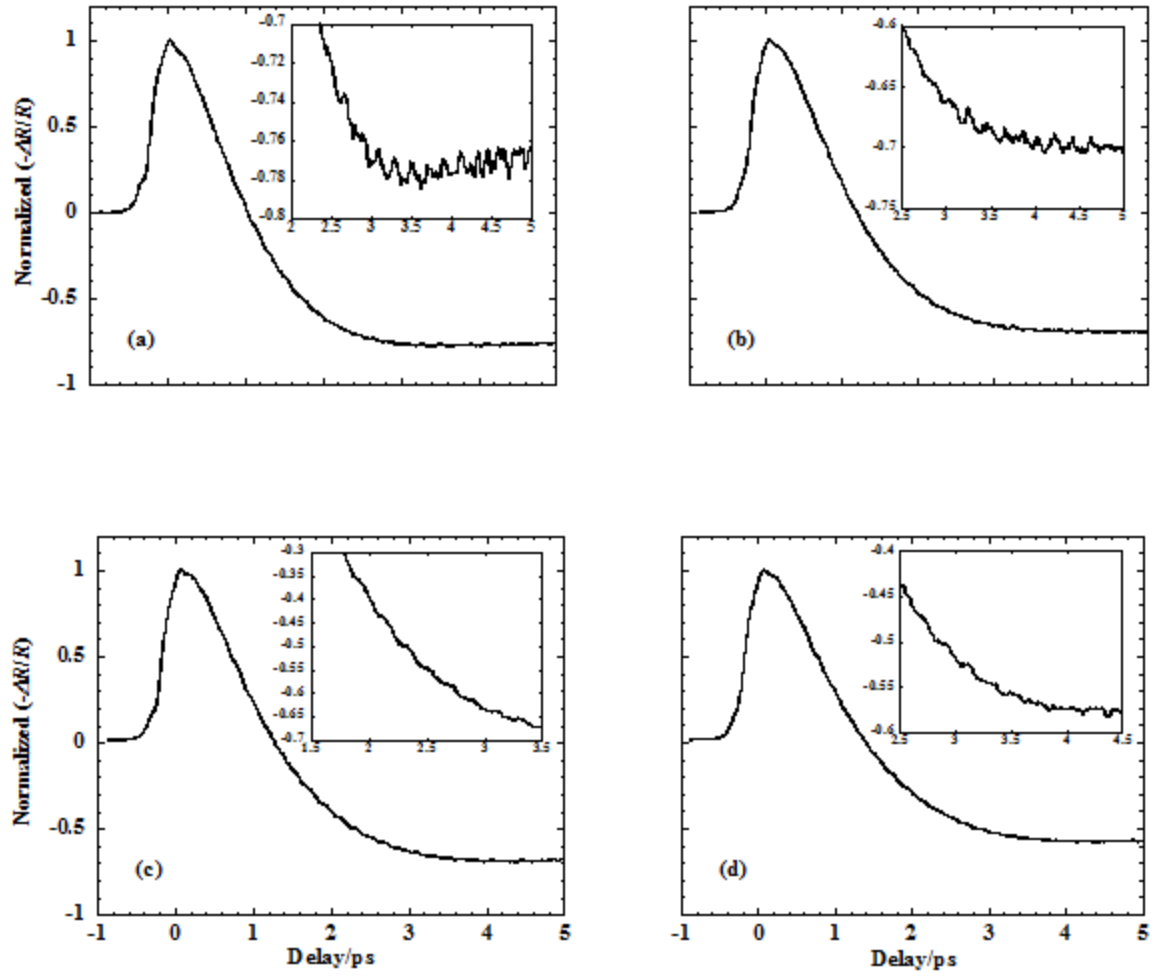


Figure 5.2. Transient reflectance signals of the filled skutterudites: (a) Ba-filled; (b) Yb-filled; (c) La-filled; (d) triple-filled (magnified in the insets).

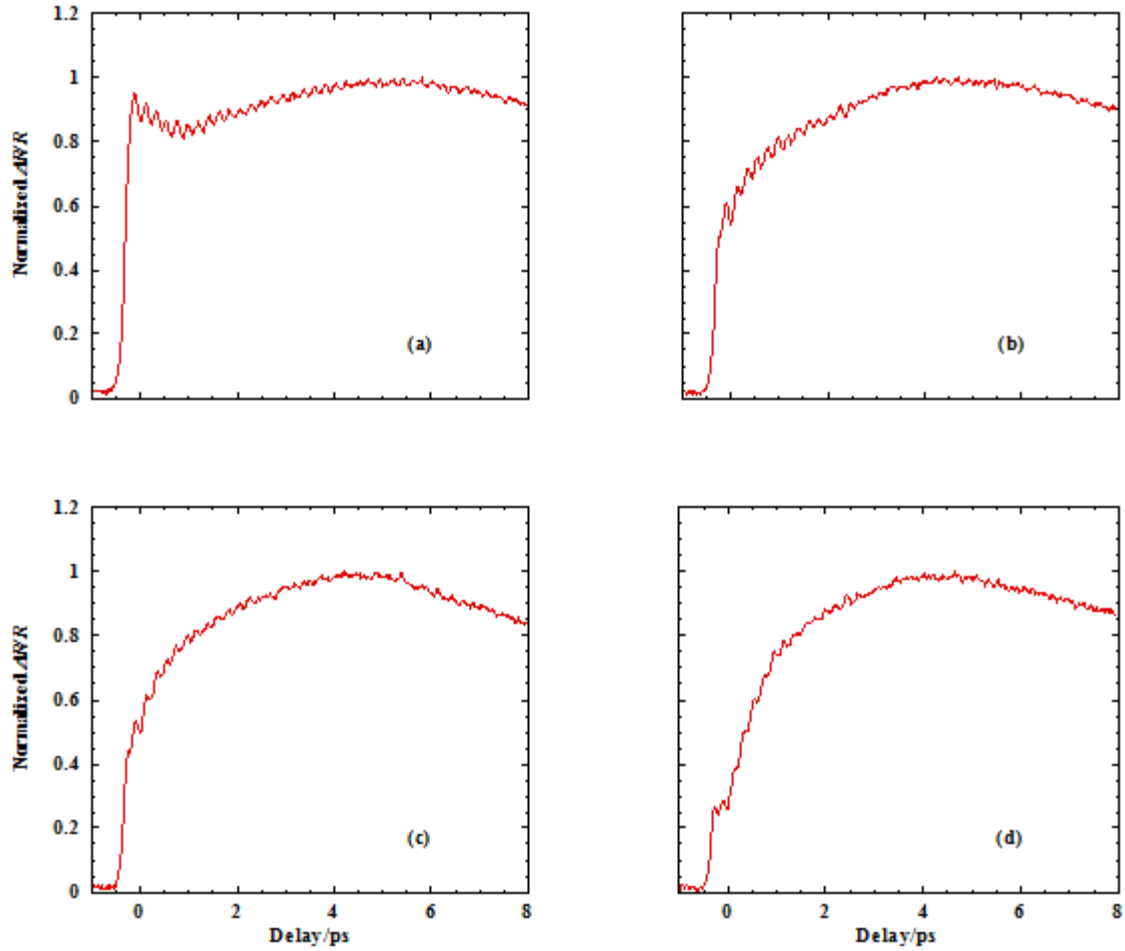


Figure 5.3. Transient reflectance signals of the filled skutterudites: (a) $\text{Mm}_{0.82}\text{Fe}_4\text{Sb}_{11.96}$; (b) $\text{Mm}_{0.72}\text{Fe}_{3.43}\text{Co}_{0.57}\text{Sb}_{11.97}$; (c) $\text{Mm}_{0.65}\text{Fe}_{2.92}\text{Co}_{1.08}\text{Sb}_{11.98}$; (d) $\text{Mm}_{0.55}\text{Fe}_{2.44}\text{Co}_{1.56}\text{Sb}_{11.96}$ (Mm represents misch-metal atoms).

5.1.3 Identification of the Oscillation Modes

In order to identify the detected oscillation modes, a second-order Butterworth bandpass filter is applied to remove the background carrier signal and then Fourier transform is performed to analyze the spectrums of the oscillation, as shown in Fig. 5.4, with dominating peaks marked by the vertical dashed lines. The spectrums are normalized and shifted for clarity. The peak around 174 cm^{-1} exists for all the samples and shifts little with varying filling species. A phonon mode at this frequency was found

in Raman spectroscopy as one of the F_g modes (Nolas, *et al.*, 1999 and Feldman, *et al.*, 2003), which involves motion of the Sb atoms but is not related to the filling atoms. For the three single-filled samples, another mode around 150 cm^{-1} is apparently affected by the nature of the filling atoms. For the triple-filled sample, there are two peaks near 150 cm^{-1} .

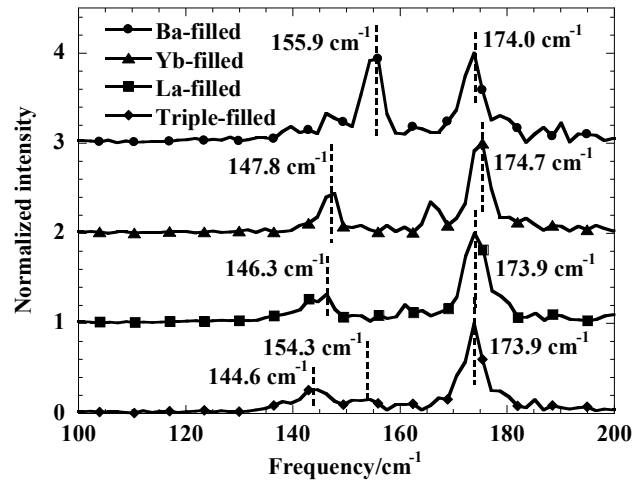


Figure 5.4. Normalized spectra of the transient reflectance signals of the filled skutterudites.

For identification of the detected modes, Raman spectrums of the samples are measured and shown in Fig. 5.5. The spectrums are shifted for clarity. The Raman spectrums of all the samples are similar with regard to the positions of the Raman peaks, and the only detected mode near 150 cm^{-1} is the low-energy A_g mode, which is one of the breathing modes of the Sb_4 ring and marked in the plot. Considering the nonuniformity of the sample surfaces, the frequencies of the concerned modes are measured at seven points and the averages are used for analysis. The frequencies of the low-energy A_g modes from Raman spectroscopy are 145.8 cm^{-1} , 147.7 cm^{-1} , 147.5 cm^{-1} , and 147.7 cm^{-1} for the Ba-filled, Yb-filled, La-filled, and triple-filled samples, respectively. Compared with Fig. 5.4,

it is clear that the modes near 150 cm^{-1} observed in the transient reflectance measurement are different from the low-energy A_g modes. As explained previously by Wang, *et al.* (2009), the oscillation in the transient reflectance signals is caused by the resonant interaction between the filling atoms and the host lattice.

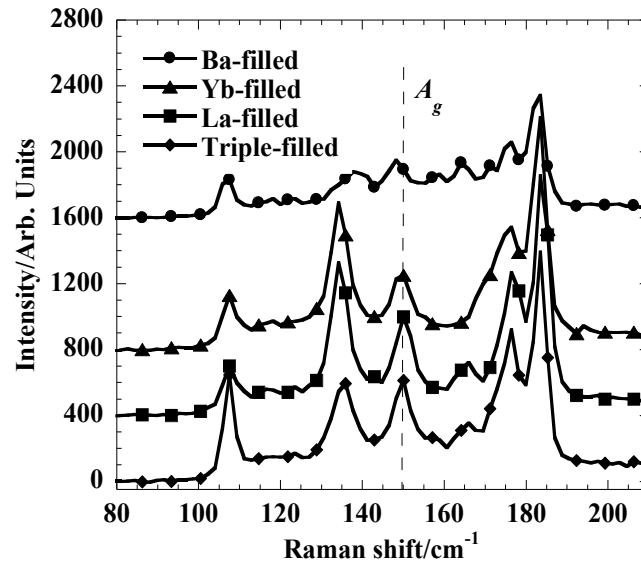


Figure 5.5. Raman spectra of the filled skutterudites.

Figure 5.4 also shows that Yb and La generate resonant interaction modes with close frequencies, but different from the mode frequency produced by Ba. The oscillation spectrum for the triple-filled sample includes two resonance frequencies with one close to the frequency caused by Yb or La and the other close to that caused by Ba. We can thus conclude that filling the skutterudite crystal structure with different elements causes different resonance frequencies for the host-guest system.

5.1.4 Effect of the Resonant Interaction on Lattice Thermal Conductivity

To evaluate the contribution of the resonant interaction mode to the thermal conductivity, k_L is deduced from the total thermal conductivity and the electrical conductivity using Wiedemann-Franz relation (Lorenz number set equal to $2.0 \times 10^{-8} \text{ V}^2/\text{K}^2$). The total thermal conductivity and the electrical conductivity were measured in Chemical and Materials Systems Laboratory, GM Global R&D. The model based on the Debye approximation is taken to fit the deduced k_L from 4 K to 300 K (Yang, *et al.*, 2003 and Nolas, *et al.*, 2006):

$$k_L = \frac{k_B}{2\pi^2 v} \left(\frac{k_B T}{\hbar} \right)^3 \int_0^{\frac{\theta_D}{T}} \frac{x^4 e^x dx}{\tau^{-1} (e^x - 1)^2}, \quad (5.1)$$

where $x = \hbar\omega/k_B T$, \hbar is the reduced Planck constant, ω is the phonon angular frequency, k_B is the Boltzmann constant, and T is the temperature. The sound velocity v and the Debye temperature, θ_D , are 2700 m/s and 287 K respectively (Nolas, *et al.*, 2006). The phonon relaxation time τ is given by:

$$\tau^{-1} = \frac{v}{L} + A\omega^4 + B\omega^2 T \exp\left(-\frac{\theta_D}{3T}\right) + \frac{1}{\tau_0} \exp\left[-\frac{(\omega - \omega_0)^2}{\omega_b^2}\right], \quad (5.2)$$

where L represents the average grain size and ω_0 is the frequency of the resonant interaction mode determined experimentally. The four terms in (5.2) represent scattering by grain boundary, point defects, phonon-phonon umklapp process, and the resonant interaction, respectively. Unlike the rattling mode, which is associated with random and independent motion of the filling atoms, the resonant interaction involves phase-matched relative motion of the host lattice and the filling atoms and disturbs phonon transport by resonant scattering. The relaxation time τ_0 (the inverse of the scattering rate) is

determined experimentally from the decay of the oscillation in the transient reflectance signal by a damping oscillator model (Misochko, *et al.*, 2004 and Wu, *et al.*, 2007). In (5.2), it is assumed that the resonant interaction mode also scatters phonons at frequency other than ω_0 , following a spectral dependence of a Gaussian form with a bandwidth of ω_b . The variables L , A , B and ω_b are adjusted to fit the experimentally determined k_L . The fitting results are shown in Fig. 5.6 with the fitting parameters listed in Table 5.1. For the triple-filled sample, two resonance terms with two resonance frequencies are used. Good fitting can be obtained except for deviations at higher temperature due to the radiation loss that affects the measured thermal conductivity (Yang, *et al.*, 2003).

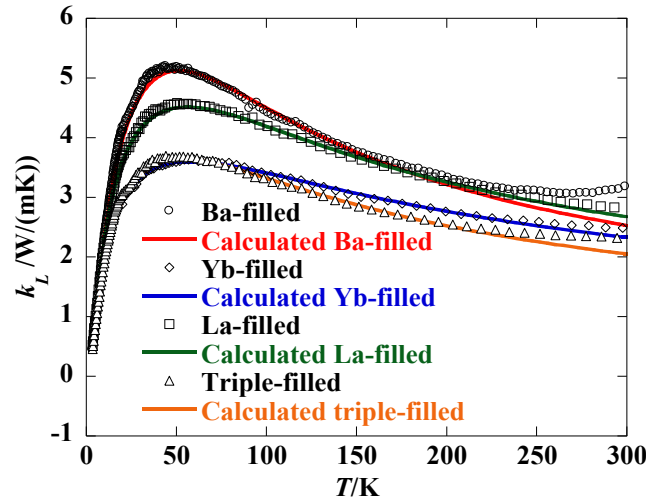


Figure 5.6. Comparison between the measured and the fitted k_L .

Filler	$L/\mu\text{m}$	$A/10^{-43} \text{ s}^3$	$B/10^{-18} \text{ s/K}$	$\omega_0/10^{12} \text{ rad/s}$	$\omega_b/10^{12} \text{ rad/s}$	τ_0/ps
Ba	3.13	121.21	5.05	29.52	10.80	3.94
Yb	4.34	298.99	2.45	27.63	8.85	2.93
La	3.74	185.86	3.01	27.63	9.29	2.93
Triple	4.22	230.30	4.13	27.00/28.89	9.36/8.85	2.53/1.92

We then evaluate and compare the contribution of each scattering term at the frequency ω_0 and 300 K, which is shown in Fig. 5.7. For the triple-filled sample, the low-frequency resonance term is used. It is seen that the boundary scattering contributes the least at this temperature (almost invisible in the plot) and the other three terms have comparable magnitudes, indicating that the resonance interaction has a considerable influence on k_L . For the triple-filled sample, the existence of two resonant terms increases the effect on k_L .

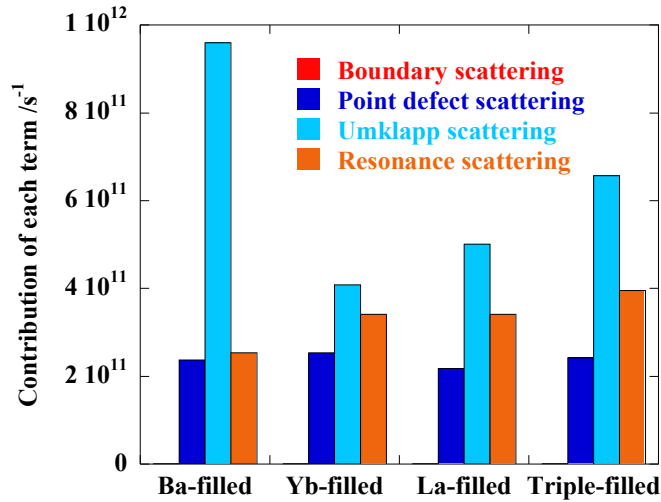


Figure 5.7. Comparison of each scattering term at the resonance frequency and 300 K in (5.2).

In summary, ultrafast spectroscopy is used to detect coherent lattice vibration in single- and triple-filled skutterudites. Comparison of the oscillation spectrums with the Raman spectrums indicates that the detected oscillation represents resonant interaction of the host-guest system and filling with different elements causes different resonance frequencies. By fitting experimentally deduced k_L with measured resonant frequencies and scattering rates, it is justified that the resonant interaction mode has a considerable

contribution to the reduction of k_L , and that multiple-element filling can suppress k_L of skutterudites more effectively.

5.2 Dynamics of Photoexcited Carriers in Skutterudites

For improving the thermoelectric performance of skutterudites, besides thermal conduction of the lattice part, it is also important to learn about the transport properties of carriers, which contribute to part of thermal conduction and the entire electrical conduction. In this section, the carrier dynamics of FeSb₃-based skutterudites is investigated using ultrafast spectroscopy, which reflects the transport properties of carriers.

5.2.1 Band Structure of Skutterudites

The carrier dynamics can be understood in terms of the band structure of skutterudites which was mainly characterized by *ab initio* calculation (Singh, *et al.*, 1994 and 1997, Nordstrom, *et al.*, 1996, Koga, *et al.*, 2005, and Takegahara, *et al.*, 2008). The band structure and the density of states (DOS) of BaFe₄Sb₁₂ calculated by Takegahara, *et al.* (2008) are shown in Fig. 5.8 as an example. There is a region with very low DOS near the Fermi level E_F that separates the conduction band and the valence band as clearly seen in Fig. 5.8. This region is called a pseudogap since actually there is a single band crossing this region that almost touches the conduction band edge at the Γ point. However, this single band contributes little to the DOS and thus little to carrier transition, so the pseudogap is usually observed in optical experiments instead of the real gap. The pseudogap is about 0.68 eV (1 Ry = 13.6 eV) from the DOS calculation. The pseudogap and the single band crossing the pseudogap characterize the band structures of typical skutterudites.

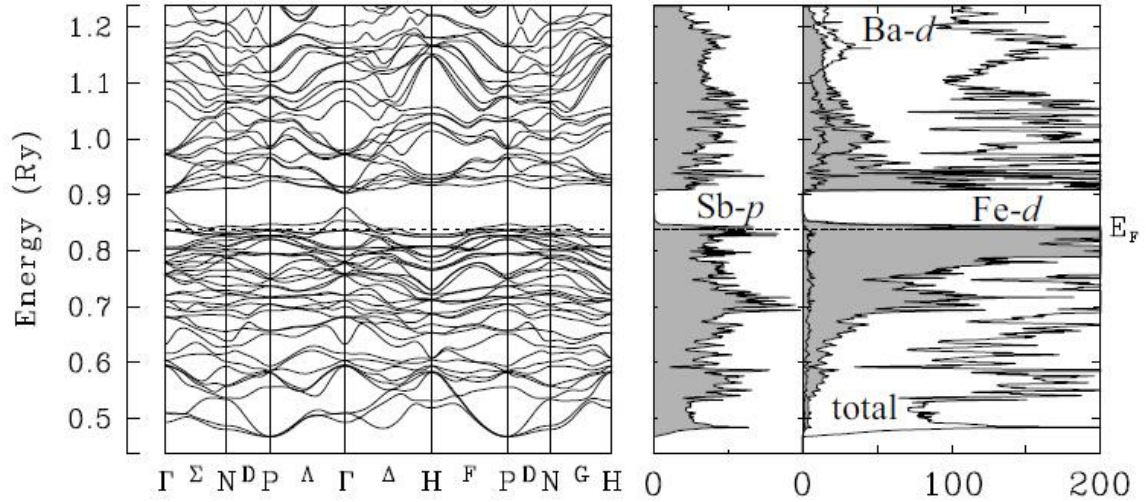


Figure 5.8. Band structure and DOS of $\text{BaFe}_4\text{Sb}_{12}$ (Takegahara, *et al.*, 2008).

As introduced in Section 5.1.1, filling skutterudites with proper elements and concentrations can lead to improved thermoelectric performance. Generally, filling with metal atoms changes the band structure shape only to a small extent and the main effect is to introduce extra valence electrons, which lifts E_F towards or into the conduction band (Løvvik, *et al.*, 2004). Charge compensation is usually required to realize high filling concentration with stable material structure. This is generally achieved through substitution of the transition metal atoms by a lower valent element (e. g. replacement of Co by Fe). This substitution will make the material more deficient in electrons and lower E_F . In this work, the misch-metal-filled skutterudite $\text{Mm}_{0.65}\text{Fe}_{2.92}\text{Co}_{1.08}\text{Sb}_{11.98}$ is investigated in terms of the carriers dynamics, which is of interest in practice because misch metal is much cheaper than individual rare-earth metal. It is assumed that the band structure of this material is close to that of $\text{BaFe}_4\text{Sb}_{12}$.

5.2.2 Transient Reflectance Measurement on Filled Skutterudites Using 800 nm Pump and Probe with Varying Wavelength

The optical setup used is based on the one described in Section 2.1 except that the center wavelength of the pump is 800 nm (1.55 eV), and the OPA is used to tune the wavelength of the probe. The transient reflectance signals of $\text{Mm}_{0.65}\text{Fe}_{2.92}\text{Co}_{1.08}\text{Sb}_{11.98}$ are shown in Fig. 5.9, from which the dependence of the signal trend on probe wavelength is clearly seen. The pump fluence is 0.42 mJ/cm^2 . Some curves are shifted vertically for clarity. Within the wavelength range, both the pump and the probe have photon energies over the pseudogap of the material, 0.68 eV as introduced in Section 5.2.1. Therefore, the transient reflectance signals indicate change of absorption for interband transition across the pseudogap. When the probe wavelength is longer than 1200 nm, the signal shows a fast increase followed by a fast decay and then an ensuing slow bump as indicated in Fig. 5.9 (a). As the probe wavelength decreases, the fast increasing and decaying component weakens and is replaced by a decrease, followed by a fast recovery and a slow bump as shown in Fig. 5.9 (b) and (c).

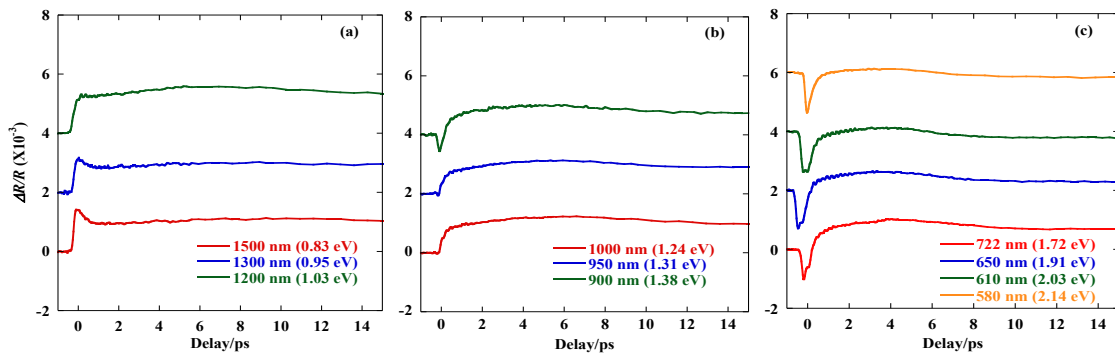


Figure 5.9. Transient reflectance signals of $\text{Mm}_{0.65}\text{Fe}_{2.92}\text{Co}_{1.08}\text{Sb}_{11.98}$ with pump wavelength 800 nm, probe wavelength: (a) 1500 nm, 1300 nm, and 1200 nm; (b) 1000 nm, 950 nm, and 900 nm; (c) 722 nm, 650 nm, 610 nm, and 580 nm.

The trend of the signals immediately after the excitation (within 1 ps delay) can be well explained by the analysis based on the Kramers-Kronig relations as introduced in Section 2.2 and illustrated in Section 4.2.1 for GaAs. The band filling effect reduces the imaginary part of the dielectric constant ε_2 near the pump wavelength λ_{pump} , which induces accompanying change of the real part ε_1 with positive sign on the blue side of the ε_2 sink and negative sign on the red side (Fig. 4.11). The difference from the case of GaAs is the sign of ΔR . The value of the dielectric constant ε can be obtained from the optical conductivity and the reflectance spectrum. For example, from the work by Takabatake, *et al.* (2007), the real part of the optical conductivity at 900 nm is about $\sigma_1 = 6.4 \times 10^5 \Omega^{-1} \text{m}^{-1}$ rendering directly the imaginary part of the dielectric constant $\varepsilon_2 = \sigma_1 / (\varepsilon_0 \omega) = 34.5$ and the reflectance is about 0.6, from which the real part of the dielectric constant $\varepsilon_1 = 5.4$ can be derived. From (2.6a) and the published data of optical conductivity and reflectance spectrum (Takabatake, *et al.*, 2007), it can be found that within the entire probe wavelength range in this work, $\partial R / \partial \varepsilon_1 < 0$. The probe wavelength used in this work is shorter than λ_g . Therefore, within a short period after the excitation, for probe wavelength longer than $\lambda_{pump} = 800 \text{ nm}$, $\Delta R > 0$ since $\Delta \varepsilon_1 < 0$ while for probe wavelength shorter than $\lambda_{pump} = 800 \text{ nm}$, $\Delta R < 0$. The initial change of reflectance shown in Fig. 5.9 agrees with this prediction, except that the change of sign of reflectance occurs around 1000 nm. This is the red shift of spectral hole burning which was also observed in GaAs (Gong, *et al.*, 1991). It can be explained by slight cooling of the carriers within the duration of the pump pulse, which shifts the carriers towards the band edges.

If the transient reflectance is only affected by band filling, $\Delta R < 0$ at long delay should be seen by all the probe wavelengths in this work since when the carriers are

cooled down to the band edges, $\Delta\epsilon_I > 0$ should be detected at any wavelength shorter than λ_g . However, $\Delta R > 0$ at long delay is detected for probe wavelength 650 to 1500 nm as seen in Fig. 5.9. This is because the evolution of ΔR after a 1 ps delay is significantly affected by lattice heating. As the lattice is heated up by the hot carriers, the increased interatomic distance decreases the potential seen by the electrons and causes a shrinkage of the pseudogap. The shrinkage of the pseudogap leads to an increase in the absorption and ϵ_2 for wavelength slightly longer than λ_g , for which absorption is forbidden without the shrinkage of the pseudogap (Bennett, *et al.*, 1990). Similar to the analysis for band filling, $\Delta\epsilon_I$ can be derived using the Kramers-Kronig relations. As illustrated in Fig. 5.10, $\Delta\epsilon_I < 0$ and $\Delta R > 0$ for probe wavelength shorter than λ_g . Consequently, the transient reflectance signal at long delay times reflects the combined effect from band filling and lattice heating. The transient reflectance signals with probe wavelength closer to λ_g , such as 1,300 and 1,500 nm, show $\Delta R > 0$, indicating it is dominated by lattice heating.

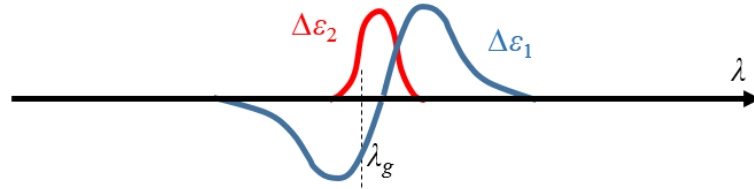


Figure 5.10. Change of the dielectric constant due to the pseudogap shrinkage induced by lattice heating.

The transient reflectance data can be analyzed to obtain information about the carrier relaxation time. To capture the transient physical process, the reflectance signal is approximately represented using a phenomenological model:

$$\Delta R/R = B_c + A_c \exp(-t/t_c) + A_l[1 - \exp(-t/t_l)] + A_s \sin(\omega t - \pi/2). \quad (5.3)$$

The subscript c is for carriers, l for lattice, and s for strain. The sum of the first and the second terms accounts for the effect of band filling by photoexcited carriers. B_c accounts for the change of the reflectance due to band filling after carriers are cooled down to the band edges as predicted by the Kramers-Kronig relations and the exponential term models the relaxation of hot carriers. The third term describes the contribution from lattice heating. The sinusoidal term models the contribution from strain or acoustic phonon, which will be discussed later. The fitting parameters are listed in Table 5.2 for probe wavelength 1500 nm, 1200nm, 1000 nm, and 650 nm. As the probe wavelength decreases, the value of A_c changes from positive to negative as predicted by the Kramers-Kronig relations. t_c is shorter for short probe wavelength, which detects high-energy states, because carriers with high kinetic energy have stronger interaction with other carriers and phonons. It is also found that t_l decreases as the probe wavelength decreases. The possible reason is that the change of the dielectric constant is larger for wavelength near λ_g and decays to zero for wavelength far from λ_g . Therefore, probing with shorter wavelength, which detects states far from the band edges, senses the lattice heating process for a shorter period. For more accurate explanation, sophisticated simulations such as *ab initio* calculations will be needed. The frequency ω of the oscillation due to acoustic phonon increases for shorter probe wavelength, which will be discussed later. It is found that the deviation of the fitting results from the measured signals becomes larger for short probe wavelength. The possible reason is that the probe with high photon energy can access more energy levels. Relaxation of carriers on multiple energy levels contributes to the transient reflectance signal; therefore (5.3) is not comprehensive enough to capture all the physical processes.

Table 5.2. Fitting parameters for the transient reflectance signals of skutterudites.

Probe wavelength/nm	B_c	A_c	t_c/ps	A_l	t_l/ps	A_s	$\omega/\text{rad/ps}$
1500	-0.08	1.58	0.71	1.13	1.06	0.05	0.33
1200	-0.04	1.48	0.65	1.51	0.78	0.12	0.45
1000	-0.01	0.94	0.57	1.15	0.63	0.09	0.52
650	0.00	-1.03	0.33	0.35	0.35	0.10	0.78

In Fig. 5.11 (a), the fitting result for 1500 nm probe is shown together with the individual contribution from band filling, lattice heating, and acoustic phonon. The signal can be fit well up to 15 ps. After 15 ps, the model cannot describe the physical process well since it does not consider carrier recombination and diffusion. In Fig. 5.11 (b), the normalized transient reflectance signals measured using 1500 nm probe with varied pump fluence are plotted. The signals show a similar trend. This indicates that the carrier-phonon interaction, instead of carrier-carrier interaction, dominates the energy transfer process during this period for which the carrier-phonon scattering rate is linear versus the carrier density and the coupling time is nearly constant.

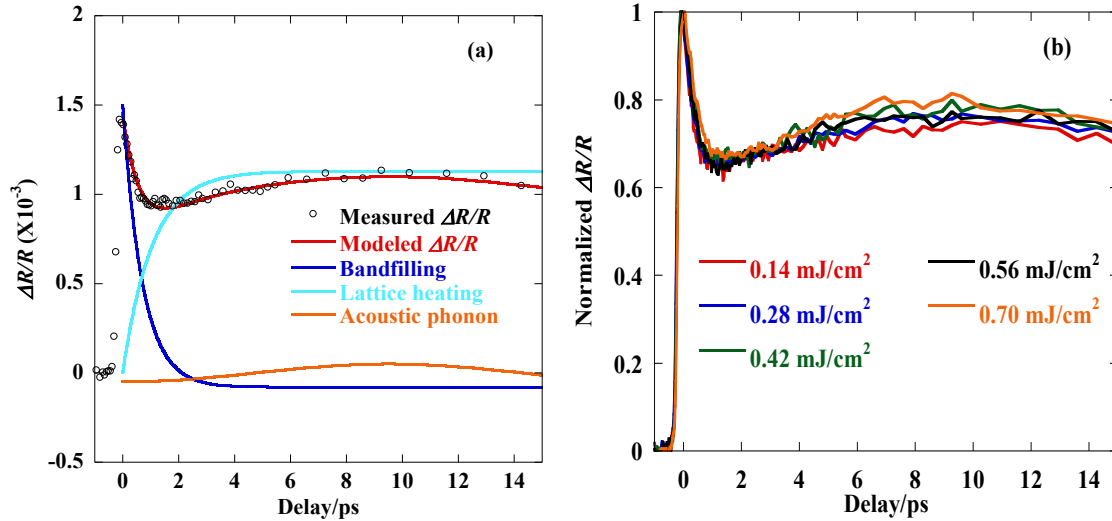


Figure 5.11. Transient reflectance signal of $\text{Mm}_{0.65}\text{Fe}_{2.92}\text{Co}_{1.08}\text{Sb}_{11.98}$ with pump wavelength 800 nm, probe wavelength 1500 nm (a) by fluence 0.42 mJ/cm^2 together with the fitting result by the model described in (5.3); (b) at varying pump fluence after normalization.

In some cases, for example, for gaining an understanding of the carrier-phonon interactions at near equilibrium states, one would be interested in detecting the interactions between carriers near the band edge and phonons. For that, the photon energy of the pump laser should be tuned to below the pseudogap to excite only free carriers, i.e., electrons in n -type samples or holes in p -type samples. The photon energy of the probe laser should be tuned to close to the pseudogap so that only band-edge states are probed. An additional benefit is that the transport properties of electrons and holes can be investigated separately. However, our current capability limits us to the wavelengths range as reported above.

Another observation is the generation of acoustic phonon, shown in Fig. 5.12 in a longer time scale as oscillation. This oscillation in the transient reflectance signal decays fast, which can hardly be detected after two periods. A similar phenomenon was found for bulk As_2Se_3 and was explained as change of reflectance caused by thermo-induced strain or longitudinal acoustic phonon (Thomsen, *et al.*, 1986). The strain pulse propagates from the surface to the deeper part of the sample and induces a local change of the dielectric constant moving together with the strain pulse. This leads to a propagating wave with a local change of optical properties, from which the incident light can be partially reflected. The contribution to reflectance from the wave is characterized by a periodic function with respect to time. Physically, this is because as the wave propagates through the sample, the light reflected from the wave can interfere constructively or destructively with the wave reflected from the surface. The alternative constructive and destructive interference, depending on the depth of the interface, results

in the oscillatory behavior of the reflectance in the time domain, with the oscillation period given by (Thomsen, *et al.*, 1986):

$$T = \lambda/(2nv), \quad (5.4)$$

where λ is the wavelength of the probe, n is the refractive index of the probe and v is the sound velocity. From the published data for optical conductivity and reflectance spectrum (Takabatake, *et al.*, 2007), n is roughly constant at 4.5 from 900 nm to 1300 nm. The longitudinal sound velocity is about 4000 m/s (He, *et al.*, 2014). According to (5.4), the periods of the oscillation are 25.0 ps for 900 nm probe, 27.8 ps for 1000 nm probe, 34.1 ps for 1200 nm probe, and 35.3 ps for 1300 nm probe. There is some uncertainty in the optical properties and the sound velocity due to different sample compositions. Also, the strain pulse spans a certain spatial length and undergoes dispersion during propagation, which also renders uncertainty to the analysis. However, the predicted trend agrees with the experimental observation.

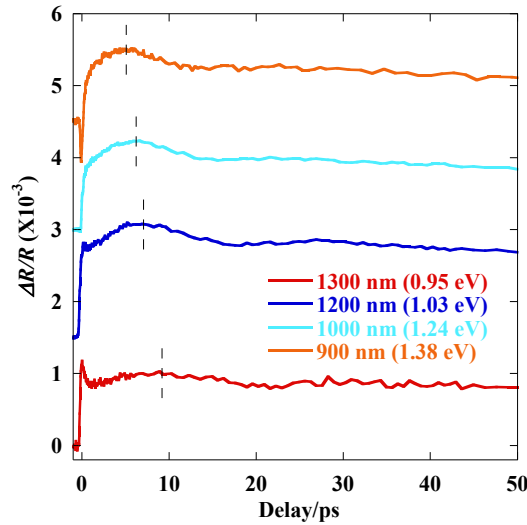


Figure 5.12. Transient reflectance signals of $\text{Mm}_{0.65}\text{Fe}_{2.92}\text{Co}_{1.08}\text{Sb}_{11.98}$ with probe wavelength 1300 nm, 1200 nm, 1000 nm and 900 nm shown in a long-time scale (The first oscillation peak is marked by the dashed line).

In summary, ultrafast spectroscopy is applied to study the dynamics of energy carriers in skutterudites. Probing the transient reflectance by varied wavelength shows that the short-time signal after excitation, which can be predicted well by the Kramers-Kronig relations, reflects band filling due to photoexcited carriers and the long-time signal is dominated by the shrinkage of the pseudogap induced by lattice heating. The relaxation time of hot carriers is obtained by analysis based on a phenomenological model. Fitting the transient reflectance signal shows that hot carriers at high energy levels generally have stronger interaction with other carriers and phonons. Oscillation in the transient reflectance is attributed to thermo-induced longitudinal acoustic phonon. In simulation, the carrier relaxation time detected by ultrafast spectroscopy can be evaluated by convolution of *ab initio* calculation, Fermi's golden rule and MD calculation. This work provides experimental justification of the simulation results, which can help to improve, for example, the potential function used in MD calculation.

5.3 Summary

To sum up, ultrafast spectroscopy is used to measure the transient reflectance of skutterudites. Vibration modes are detected and identified as the interaction modes between guest atoms and the host lattice in filled skutterudites. Such modes can scatter phonons and suppress the lattice-mediated thermal conduction to a considerable extent. Interaction modes with different frequencies are detected in a multiple-filled skutterudite sample, which can scatter phonons in a broader spectral range and more effectively reduce the thermal conductivity of the lattice k_L . Transient dynamics of carriers is analyzed by varying the probe wavelength. Band filling and lattice heating are identified as the two main effects determining the temporal evolution of the reflectance.

CHAPTER 6. CONCLUSIONS AND FUTURE WORK

6.1 Summary and Conclusions

Ultrafast spectroscopy based on transient reflectance measurement is used for investigating the dynamics of energy carriers in solid state materials.

Transient reflectance measurement is conducted for gold films on silicon substrates to study the interface heat transfer. It is shown by the two-temperature model (TTM) that due to the strong thermal nonequilibrium between electrons and phonons during and immediately after ultrafast-laser heating, it is possible to isolate the effect of the direct electron-phonon coupling across the metal-dielectric interface, facilitating evaluation of its strength. Comparison between the transient reflectance signals and the simulation results indicates that the direct coupling between electrons in the metal and phonons in the dielectric substrate is strong enough to dominate the interface heat transfer during the heating of thin films by ultrafast laser.

To explore the carrier dynamics in detail, transient reflectance measurement is conducted by varying laser wavelength, which realizes access to different energy levels. Gold and gallium arsenide (GaAs) are inspected as representatives of metals and semiconductors. The excitation and the relaxation processes of carriers are analyzed by referring to the band structure. The general process of analysis includes identification of the filled states by photoexcited carriers, evaluation of the imaginary part of the dielectric

constant, which is directly related to band filling or absorption saturation, evaluation of the real part of the dielectric constant through the Kramers-Kronig relations and prediction of the reflectance change. Such analysis relates the transient reflectance signal to the carrier dynamics and therefore transport properties of carriers can be deduced from the time-resolved signal. The analog between metals and semiconductors in the detection of the carrier dynamics by ultrafast spectroscopy is demonstrated.

Ultrafast spectroscopy is also used to study the dynamics of energy carriers of skutterudites, an important semiconductor for thermoelectric application. Vibration modes caused by interaction between guest atoms and the host lattice in filled skutterudites are detected, which can scatter phonons and reduce the lattice part of thermal conductivity. It is also found that filling skutterudites by several elements can induce interaction modes with different frequencies, which can scatter phonons in a broader spectrum and suppress the lattice-mediated thermal conduction more effectively. The transient dynamics of carriers in skutterudites is investigated by varying the probe wavelength. Band filling and lattice heating are identified as the two main effects determining the temporal evolution of the reflectance, from which the carrier relaxation time can be obtained.

6.2 Future Work

The interaction between solids and ultrafast laser is generally complex and lots of physical processes are not well-known yet. In the future work, experimental techniques can be improved and more important materials can be inspected.

White light can be involved in ultrafast spectroscopy to realize detection of continuous energy states. Analysis of the band structure and the transient physical

process helps to select a proper wavelength, which can facilitate the study by protruding the interested physical process. Also, transmission and reflection can be measured simultaneously, from which the evolution of the dielectric constant can be deduced. Such analysis is more accurate than the current indirect methodology based on the Kramers-Kronig relations. Another possible improvement is to couple the basic pump-probe setup to a microscope, which enables detection of micro- or nano-scale samples.

In addition, the energy-carrier dynamics of materials with important applications such as graphene, black phosphorene and molybdenum disulfide (MoS_2) can be explored by ultrafast spectroscopy. *Ab initio* calculation, molecular dynamics (MD) calculation and Monte Carlo simulation can bridge the gap between experimental observables and the dynamics of energy carriers while measurement results can be used for justification of assumptions in simulation.

The final goal of this work is to provide a clear picture of typical transient processes in all kinds of solids during the interaction with ultrafast laser pulses. Such investigation can help to understand the effect of energy carriers on thermal transport properties of solids and to raise the utilizing efficiency of thermal energy.

LIST OF REFERENCES

LIST OF REFERENCES

- Anisimov, S. I., Kapeliovich, B. L., and Perel'man, T. L., 1974, "Electron Emission From Metal Surfaces Exposed to Ultrashort Laser Pulses," *Soviet Physics JETP*, Vol. 39, No. 2, pp. 375-377.
- Anisimov, S. I. and Rethfeld, B., 1997, "On the Theory of Ultrashort Laser Pulse Interaction with a Metal," *Proceedings of the SPIE*, Vol. 3093, pp. 192-203.
- Ashcroft, N. W. and Mermin, N. D., 1976, *Solid State Physics*, Brooks/Cole.
- Bosco, C. A. C., Azevedo, A., and Acioli, L. H., 2003, "Substrate Dependent Ultrafast Dynamics in Thin NiFe Films," *Applied Physics Letters*, Vol. 83, No. 9, pp. 1767-1769.
- Bennett, B. R., Soref, R. A., and Del Alamo, J. A., 1990, "Carrier-Induced Change in Refractive Index of InP, GaAs, and InGaAsP," *IEEE Journal of Quantum Electronics*, Vol. 26, No. 1, pp. 113-122.
- Bernstein, N., Feldman, J. L., and Singh, D. J., 2010, "Calculations of Dynamical Properties of Skutterudites: Thermal Conductivity, Thermal Expansivity, and Atomic Mean-Square Displacement," *Physical Review B*, Vol. 81, No. 13, pp. 134301-1-11.
- Cahill, D. G., Ford, W. K., Goodson, K. E., Mahan, G. D., Majumdar, A., Maris, H. J., Merlin, R., and Phillpot, S. R., 2003, "Nanoscale Thermal Transport," *Journal of Applied Physics*, Vol. 93, No. 2, pp. 793-818.
- Chen, J. K., Latham, W. P., and Beraun, J. E., 2005, "The Role of Electron-Phonon Coupling in Ultrafast Laser Heating," *Journal of Laser Applications*, Vol. 17, No. 1, pp. 63-68.
- Chowdhury, I. H. and Xu, X., 2003, "Heat Transfer in Femtosecond Laser Processing of Metal," *Numerical Heat Transfer, Part A: Applications*, Vol. 44, No. 3, pp. 219-232.

Colavita, E., Franciosi, A., Mariani, C., and Rosei, R., 1983, "Thermoreflectance Test of W, Mo and Paramagnetic Cr Band Structures," *Physical Review B*, Vol. 27, No. 8, pp. 4684-4693.

Dordevic, S. V., Dilley, N. R., Bauer, E. D., Basov, D. N., Maple, M. B., and Degiorgi, L., 1999, "Optical Properties of $\text{MFe}_4\text{P}_{12}$ Filled Skutterudites," *Physical Review B*, Vol. 60, No. 16, pp. 11321-11328.

Eesley, G. L., 1983, "Observation of Nonequilibrium Electron Heating in Copper," *Physical Review Letters*, Vol. 51, No. 23, pp. 2140-2143.

Ehrenreich, H. and Phillip, H. R., 1962, "Optical Properties of Ag and Cu," *Physical Review*, Vol. 128, No. 4, pp. 1622-1629.

Fann, W. S., Storz, R., Tom, H. W. K., and Bokor, J., 1992, "Direct Measurement of Nonequilibrium Electron-Energy Distributions in Subpicosecond Laser-Heated Gold Films," *Physical Review Letters*, Vol. 68, No. 18, pp. 2834-2837.

Feldman, J. L., Singh, D. J., and Kendziora, C., 2003, "Lattice Dynamics of Filled Skutterudites: $\text{La}(\text{Fe}, \text{Co})_4\text{Sb}_{12}$," *Physical Review B*, Vol. 68, No. 9, pp. 094301-1-11.

Gong, T., Mertz, P., Nighan Jr., W. L., and Fauchet, P. M., 1991, "Femtosecond Refractive-Index Spectral Hole Burning in Intrinsic and Doped GaAs," *Applied Physics Letters*, Vol. 59, No. 6, pp. 721-723.

Groeneveld, R. H. M., Sprik, R., and Lagendijk, A., 1992, "Effect of a Nonthermal Electron Distribution on the Electron-Phonon Energy Relaxation Process in Noble Metals," *Physical Review B*, Vol. 45, No. 9, pp. 5079-5082.

He, C., Daniel, M., Grossmann, M., Ristow, O., Brick, D., Schubert, M., Albrecht, M., and Dekorsy, T., 2014, "Dynamics of Coherent Acoustic Phonons in Thin Films of CoSb_3 and Partially Filled $\text{Yb}_x\text{Co}_4\text{Sb}_{12}$ Skutterudites," *Physical Review B*, Vol. 89, No. 17, pp. 174303-1-7.

Hermann, R. P., Jin, R. Y., Schweika, W., Grandjean, F., Mandrus, D., Sales, B. C., and Long, G. J., 2003, "Einstein Oscillators in Thallium Filled Antimony Skutterudites," *Physical Review Letters*, Vol. 90, No. 13, pp. 135505-1-4.

Hohlfeld, J., Wellershoff, S.-S., Güdde, J., Conrad, U., Jähnke, V., and Matthias, E., 2000, "Electron and Lattice Dynamics Following Optical Excitation of Metals," *Chemical Physics*, Vol. 251, pp. 237-258.

Hopkins, P. E., 2010, "Influence of Electron-Boundary Scattering on Thermoreflectance Calculations After Intra- and Interband Transitions Induced by Short-Pulsed Laser Absorption," *Physical Review B*, Vol. 81, No. 3, p. 035413-1-7.

Hopkins, P. E., Duda, J. C., Salaway, R. N., Smoyer, J. L., and Norris, P. M., 2008, "Effects of Intra- and Interband Transitions on Electron-Phonon Coupling and Electron Heat Capacity After Short-Pulsed Laser Heating," *Nanoscale and Microscale Thermophysical Engineering*, Vol. 12, pp. 320-333.

Hopkins, P. E. and Norris, P. M., 2007, "Substrate Influence in Electron-Phonon Coupling Measurements in Thin Au Films," *Applied Surface Science*, Vol. 253, No. 15, pp. 6289-6294.

Hopkins, P. E., Kassebaum, J. L., and Norris, P. M., 2009, "Effects of Electron Scattering at Metal-Nonmetal Interfaces on Electron-Phonon Equilibration in Gold Films," *Journal of Applied Physics*, Vol. 105, No. 2, pp. 023710-1-8.

Hopkins, P. E., Phinney, L. M., and Serrano, J. R., 2011, "Re-examining Electron-Fermi Relaxation in Gold Films With a Nonlinear Thermoreflectance Model," *Journal of Heat Transfer*, Vol. 133, pp. 044505-1-4.

Hostetler, J. L., Smith, A. N., Czajkowsky, D. M., and Norris, P. M., 1999, "Measurement of the Electron-Phonon Coupling Factor Dependence on Film Thickness and Grain Size in Au, Cr, and Al," *Applied Optics*, Vol. 38, No. 16, pp. 3614-3620.

Huang, B. L. and Kaviani, M., 2010, "Filler-Reduced Phonon Conductivity of Thermoelectric Skutterudites: *Ab Initio* Calculations and Molecular Dynamics Simulations," *Acta Materialia*, Vol. 58, No. 13, pp. 4516-4526.

Johnson, P. B. and Christy, R. W., 1972, "Optical Constants of the Noble Metals," *Physical Review B*, Vol. 6, No. 12, pp. 4370-4379.

Kaganov, M. I., Lifshitz, I. M., and Tanatarov, L. V., 1957, "Relaxation Between Electrons and the Crystalline Lattice," *Soviet Physics JETP*, Vol. 4, No. 2, pp. 173-178.

Keppens, V., Mandrus, D., Sales, B. C., Chakoumakos, B. C., Dai, P., Coldea, R., Maple, M. B., Gajewski, D. A., Freeman, E. J., and Bennington, S., 1998, "Localized Vibrational Modes in Metallic Solids," *Nature*, Vol. 395, pp. 876-878.

Kimura, S. -I., Im, H., Mizuno, T., Narazu, S., Matsuoka, E., and Takabatake, T., 2007, "Infrared Study on the Electronic Structure of the Alkaline-Earth-Filled Skutterudites AM_4Sb_{12} (A=Sr, Ba; M=Fe, Ru, Os)," *Physical Review B*, Vol. 75, No. 24, pp. 245106-1-6.

Kittel, C., 2005, *Introduction to Solid State Physics*, John Wiley & Sons, Inc., New York, 8th edition.

Kleinke, H., 2010, "New Bulk Materials For Thermoelectric Power Generation: Clathrates and Complex Antimonides," *Chemistry of Materials*, Vol. 22, No. 3, pp. 604-611.

Koga, K., Akai, K., Oshiro, K., and Matsuura, M., 2005, "Electronic Structure and Optical Properties of Binary Skutterudite Antimonides," *Physical Review B*, Vol. 71, No. 15, pp. 155119-1-9.

Koza, M. M., Johnson, M. R., Viennois, R., Mutka, H., Girard, L., and Ravot, D., 2008, "Breakdown of Phonon Glass Paradigm in La- and Ce-Filled Fe_4Sb_{12} Skutterudites," *Nature Materials*, Vol. 7, No. 10, pp. 805-810.

Li, C. -Y., Ruoff, A. L., and Spencer, C. W., 1961, "Effect of Pressure on the Energy Gap of Bi_2Te_3 ," *Journal of Applied Physics*, Vol. 32, No. 9, pp. 1733-1735.

Li, L. X., Liu, H., Wang, J. Y., Hu, X. B., Zhao, S. R., Jiang, H. D., Huang, Q. J., Wang, H. H., and Li, Z. F., 2001, "Raman Spectroscopy Investigation of Partially Filled Skutterudite," *Chemical Physics Letters*, Vol. 347, No. 4, pp. 373-377.

Liu, W., Yan, X., Chen, G., and Ren, Z., 2012, "Recent Advances in Thermoelectric Nanocomposites," *Nano Energy*, Vol. 1, No. 1, pp. 42-56.

Løvvik, O. M. and Prytz, Ø., 2004, "Density-Functional Band-Structure Calculations for La-, Y-, and Sc-Filled CoP₃-Based Skutterudite Structures," *Physical Review B*, Vol. 70, No. 19, pp. 195119-1-6.

Lundstrom, M., 2000, *Fundamentals of Carrier Transport*, Cambridge University Press, Cambridge.

Maier, S. A., 2007, *Plasmonics: Fundamentals and Applications*, Springer Science + Business Media, New York.

Majumdar, A. and Reddy, P., 2004, "Role of Electron-Phonon Coupling in Thermal Conductance of Metal-Nonmetal Interfaces," *Applied Physics Letters*, Vol. 84, No. 23, pp. 4768-4770.

Meisner, G. P., Morelli, D. T., Hu, S., Yang, J., and C. Uher, 1998, "Structure and Lattice Thermal Conductivity of Fractionally Filled Skutterudites: Solid Solutions of Fully Filled and Unfilled End Members," *Physical Review Letters*, Vol. 80, No. 16, pp. 3551-3554.

Misochko, O. V., Hase, M., Ishioka, K., and Kitajima, M., 2004, "Observation of an Amplitude Collapse and Revival of Chirped Coherent Phonons in Bismuth," *Physical Review Letters*, Vol. 92, No. 19, pp. 197401-1-4.

Morelli, D. T., Caillat, T., Fleurial, J. -P., Borshchevsky, A., Vandersande, J., Chen, B. and Uher, C., 1995, "Low-Temperature Transport Properties of p-Type CoSb₃," *Physical Review B*, Vol. 51, No. 15, pp. 9622-9628.

Nolas, G. S., Fowler, G., and Yang, J., 2006, "Assessing the Role of Filler Atoms on the Thermal Conductivity of Filled Skutterudites," *Journal of Applied Physics*, Vol. 100, No. 4, pp. 043705-1-4.

Nolas, G. S. and Kendziora, C. A., 1999, "Raman Spectroscopy Investigation of Lanthanide-Filled and Unfilled Skutterudites," *Physical Review B*, Vol. 59, No. 9, pp. 6189-6192.

Nolas, G. S., Morelli, D. T., and Tritt, T. M., 1999, "Skutterudites: a Phonon-Glass-Electron Crystal Approach to Advanced Thermoelectric Energy Conversion Applications," *Annual Review of Materials Science*, Vol. 29, pp. 89-116.

Nolas, G. S., Takizawa, H., Endo, T., Sellinschegg, H., and Johnson, D. C., 2000, "Thermoelectric Properties of Sn-Filled Skutterudites," *Applied Physics Letters*, Vol. 77, No. 1, pp. 52-54.

Nordstrom, L. and Singh, D. J., 1996, "Electronic Structure of Ce-Filled Skutterudites," *Physical Review B*, Vol. 53, No. 3, pp. 1103-1108.

Othonos, A., 1998, "Probing Ultrafast Carrier and Phonon Dynamics in Semiconductors," *Journal of Applied Physics*, Vol. 83, No. 4, pp. 1789-1830.

Pedrotti, F. L., Pedrotti, L. S., and Pedrotti, L. M., 2007, *Introduction to Optics*, Pearson Prentice Hall, Upper Saddle River, NJ, 3rd edition.

Philipp, H. R. and Ehrenreich, H., 1963, "Optical Properties of Semiconductors," *Physical Review*, Vol. 129, No. 4, pp. 1550-1560.

Qiu, T. Q., Juhasz, T., Suarez, C., Brons, W. E., and Tien, C. L., 1994, "Femtosecond Laser Heating of Multi-Layer Metals-II. Experiments," *International Journal of Heat and Mass Transfer*, Vol. 37, No. 17, pp. 2799-2808.

Qiu, T. Q. and Tien, C. L., 1993, "Femtosecond Laser Heating of Multi-Layer Metals-I. Analysis," *International Journal of Heat and Mass Transfer*, Vol. 37, No. 17, pp. 2789-2797.

Sagar, D. M., Cooney, R. R., Sewall, S. L., Dias, E. A., Barsan, M. M., Butler, I. S., and Kambhampati, P., 2008, "Size Dependent, State-Resolved Studies of Exciton-Phonon Couplings in Strongly Confined Semiconductor Quantum Dots," *Physical Review B*, Vol. 77, No. 23, pp. 235321-1-14.

Sarma, S. D., Adam, S., Hwang, E. H., and Rossi, E., 2011, "Electronic Transport in Two-Dimensional Graphene," *Reviews of Modern Physics*, Vol. 83, No. 2, pp. 407-470.

Shank, C. V., Auston, D. H., Ippen, E. P. and Teschke, O., 1978, "Picosecond Time Resolved Reflectivity of Direct Gap Semiconductors," *Solid State Communications*, Vol. 26, No. 9, pp. 567-570.

Shi, X., Kong, H., Li, C. -P., Uher, C., Yang, J., Salvador, J. R., Wang, H., Chen, L., and Zhang, W., 2008, "Low Thermal Conductivity and High Thermoelectric Figure of Merit in n-Type $\text{Ba}_x\text{Yb}_y\text{Co}_4\text{Sb}_{12}$ Double-Filled Skutterudites," *Applied Physics Letters*, Vol. 92, No. 18, pp. 182101-1-3.

Shi, X., Yang, J., Salvador, J. R., Chi, M. F., Cho, J. Y., Wang, H., Bai, S. Q., Yang, J. H., Zhang, W. Q., and Chen, L. D., 2011, "Multiple-Filled Skutterudites: High Thermoelectric Figure of Merit Through Separately Optimizing Electrical and Thermal Transports," *Journal of the American Chemical Society*, Vol. 133, No. 20, pp. 7837-7846.

Singh, D. J. and Mazin, I. I., 1997, "Calculated Thermoelectric Properties of La-Filled Skutterudites," *Physical Review B*, Vol. 56, No. 4, pp. R1650-R1653.

Singh, D. J. and Pickett, W. E., 1994, "Skutterudite Antimonides: Quasilinear Bands and Unusual Transport," *Physical Review B*, Vol. 50, No. 15, pp. 11235-11238.

Slack, G. A., 1995, *CRC Handbook of Thermoelectrics* (edited by D. M. Rowe), CRC, Boca Raton, Florida.

Spitzer, W. G. and Whelan, J. M., 1959, "Infrared Absorption and Electron Effective Mass in n-Type Gallium Arsenide," *Physical Review*, Vol. 114, No. 1, pp. 59-63.

Streetman, B. G. and S. K. Banerjee, 2006, *Solid State Electronic Devices*, Pearson Prentice Hall, Upper Saddle River, New Jersey, 6th edition.

Sun, C. -K., Vallee, F., Acioli, L., Ippen, E. P., and Fujimoto, J. G., 1993, "Femtosecond Investigation of Electron Thermalization in Gold," *Physical Review B*, Vol. 48, No. 16, pp. 12365-12368.

Sun, C. -K., Vallee, F., Acioli, L. H., Ippen, E. P. and Fujimoto, J. G., 1994, "Femtosecond-Tunable Measurement of Electron Thermalization in Gold," *Physical Review B*, Vol. 50, No. 20, pp. 15337-15348.

Takegahara, K., Kudoh, M., and Harima, H., 2008, "Electronic Structures for Alkaline-Earth Filled Skutterudite Antimonides," *Journal of Physical Society of Japan*, Vol. 77, Supplement A, pp. 294-296.

Thomsen, C., Grahn, H. T., Maris, H. J., and Tauc, J., 1986, "Surface Generation and Detection of Phonons by Picosecond Light Pulses," *Physical Review B*, Vol. 34, No. 6, pp. 4129-4138.

Wang, Y., Xu, X., and Yang, J., 2009, "Resonant Oscillation of Misch-Metal Atoms in Filled Skutterudites," *Physical Review Letters*, Vol. 102, No. 17, pp. 175508-1-4.

Weiner, A. M., 2009, *Ultrafast Optics*, John Wiley & Sons, Inc., Hoboken, New Jersey.

Wellershoff, S. -S., Hohlfeld, J., Gdde, J., and Matthias, E., 1999, "The Role of Electron-Phonon Coupling in Femtosecond Laser Damage of Metals," *Applied Physics A*, Vol. 69, No. 1, pp. S99-S107.

Wooten, F., 1972, *Optical Properties of Solids*, Academic Press, Inc., New York.

Wu, A. Q. and Xu, X., 2007, "Coupling of Ultrafast Laser Energy to Coherent Phonons in Bismuth," *Applied Physics Letters*, Vol. 90, No. 25, pp. 251111-1-3.

Yang, J., Morelli, D. T., Meisner, G. P., Chen, W., Dyck, J. S., and Uher, C., 2003, "Effect of Sn Substituting for Sb on the Low-Temperature Transport Properties of Ytterbium-Filled Skutterudites," *Physical Review B*, Vol. 67, No. 16, pp. 165207-1-6.

Ye, H., Wicks, G. W., and Fauchet, P. M., 1999, "Hot Electron Relaxation Time in GaN," *Applied Physics Letters*, Vol. 74, No. 5, pp. 711-713.

Ye, H., Wicks, G. W., and Fauchet, P. M., 2000, "Hot Hole Relaxation Dynamics in p-GaN," *Applied Physics Letters*, Vol. 77, No. 8, pp. 1185-1187.

VITA

VITA

Liang Guo

Education

Ph. D., Mechanical Engineering, Purdue University, West Lafayette, IN, 2009-2014

B. S., Mechanical Engineering, Tsinghua University, Beijing, China, 2005-2009

Research Interests

Dynamics of photoexcited carriers in solid state materials

Excitation and detection of coherent phonons by ultrafast spectroscopy

Heat transfer across interfaces

Technical Skills

Ultrafast spectroscopy (including operation of pulse shaper and OPA)

Raman spectroscopy

Programming Languages: C, Fortran, Labview, C++, Java

Simulation: lattice dynamics, molecular dynamics and Boltzmann transport equation

Publication

Wang, Y., Guo, L., Xu, X., Pierce, J., and Venkatasubramanian, R., *Phys. Rev. B*, 88(6), 064307-1(2013).

Guo, L., Xu, X., Salvador, J. R., and Meisner, G. P., *J. of Electronic Materials*, 42(7), 1978 (2013).

Guo, L., Xu, X., Salvador, J. R., and Meisner, G. P., *Appl. Phys. Lett.*, 102(11), 111905-1 (2013).

Guo, L., Hodson, S. L., Fisher, T. S., Xu, X., *J. Heat Trans.*, 134(4), 042402-1 (2012).